# Plasmon Hybridization for Tip-Enhanced Raman Analysis of Nanomaterials

**Kazumasa Uetsuki**

**September 2012**

# Contents

# Introduction

The adventure of exploring a new world is always thrilling and exciting. From an early age, I liked to take on difficult problems and challenges in areas such as mathematics, quizzes, and board games; the more complicated the problem, the more exciting I found it. This is because of the sense I had that the approach to and the process of solving the problem was just such an uncharted adventure of exploration. The physics of light is one of the greatest fields of adventure in my environment. If you ever have the opportunity to study light, you will find out about the physics of light and its many different characteristic actions that play a hidden role in our daily life, such as scattering, absorption, and refraction, which are based on the interaction between light and materials. For example, we can see objects through light because of the absorption of light by the photoreceptor cells of our retinae, and we can enjoy a rainbow due to the refraction of sunlight by water droplets in the atmosphere. In particular, the interaction of light with materials induces interesting phenomena in the nano-scale world, where things happen that are difficult even to imagine. I wanted to explore such phenomena for myself and to discover the core of the physics that causes them. That is how I began my study of the unresolved phenomena mediated by light in the nano-scale world.

My first research topic after I joined the Kawata laboratory in 2006 was an investigation of carbon nanotubes using Raman microscopy. At first, I was overwhelmed by the abundance of spectroscopic information provided by photons interacting with the electronic or vibronic structures of molecules. As I grew familiar with research into physical analysis based on the interaction between light and materials, I became interested in the visualization of the consequences of physical interactions in the nano-scale world using Raman microscopy. I was stimulated by the clear fact that I was the first person to watch and elucidate these visualized images in my research, so that I felt like the explorer of a new world. I thus became involved in observing and analyzing materials at the nano-scale level using light.

How small an object can we identify with light? I would like to answer this problem by tracing the history of human exploration of miniature worlds. About three hundred and fifty years ago, a

certain book invited scientists into the micro-world. The book was *Micrographia*, published by Robert Hooke in 1665. As the name of the book suggests, it presented graphics of insects, minerals, plants, and animals in micro-scale. The sketch pictures were so amazing and beautiful that many scientists were attracted and inspired by the miniature world, and the book became the world's first scientific bestseller. Why was the book so alluring for scientists at the time? Because it gave an accurate representation of an unknown world that human beings had never been to in a way that surpassed contemporary human capabilities. The observations on which the book was based were made using optical microscopy. The innovation of sample observation through optical microscopes had been creating new branches of science and technology in research fields such as physics, chemistry, and biology, and had drawn the interest and passion of scientists toward ever smaller world. In the nineteenth century, the performance of optical microscopes was significantly improved by new lens manufacturing techniques, and microscopes became more widely utilized in biological and medical investigation. Against the trend, a limitation of optical microscopes was discovered in 1873 by Ernst Abbe, who found that light traveling through a lens makes a spot due to its wave nature. Abbe concluded that light could not be focused to less than approximately half its wavelength, which was called the diffraction limit of light.

Can we observe the nano-scale world with light? The answer is 'Yes'. Toward the goal of nano-observation using light, a wide variety of optical microscopic technologies were invented through the efforts of pioneers in the late twentieth century. These innovations were achieved by taking the quantized photon as the essential element of light. In this way, a number of optical microscopic techniques were established which achieve super-resolution beyond the diffraction limit of light, for example, near-field scanning optical microscopy (NSOM),[1-3] stimulated emission depletion (STED) microscopy,[4] photoactivated localization microscopy (PALM),[5] stochastic optical reconstruction microscopy (STORM),[6] and saturated excitation (SAX) microscopy.[7] These techniques can capture spectral information from sample materials at nano-scale spatial resolution, which is one of the biggest differences from other high-resolution microscopic techniques such as scanning electron microscopy (SEM), scanning tunneling microscopy (STM), and atomic force microscopy (AFM). In addition, since a photon inherently has a small energy and propagates through air and water, super-resolution optical microscopy simultaneously allows both observation and analysis of objects *in situ* without any invasive processes.

Among the various options in super-resolution optical microscopy, I decided in my doctoral course to explore tip-enhanced near-field optical microscopy, which is a type of NSOM, because this form of microscopy had the potential to make the most effective use of photons as conveyor of

information from materials. Tip-enhanced NSOM was first proposed by Satoshi Kawata and co-workers in 1992 as the subject of a Japanese patent. The mechanism is based upon the excitation of localized surface plasmon polaritons at a nanometric metallic probe apex, which generates a strongly enhanced electric field of light adjacent to the probe apex. The locally enhanced field is utilized as a nanometric spot of light. The nano light source can be used for a variety of spectroscopic interactions such as scattering,[8-12] fluorescence,[13,14] and absorption.[15,16] In particular, tip-enhanced Raman scattering (TERS) microscopy is a promising method for molecular analysis providing a wealth of Raman spectral information. The first demonstration of TERS spectroscopy on Rhodamine 6G molecules, reported by Kawata group in 1999, provided an experimental indication of the utility of TERS spectroscopy.[8] In 2002, three years later to the first demonstration, TERS images of two mixed dyes were produced,[17] which represented the first attainment of Raman images beyond the diffraction limit of light. In the following year, TERS images of single-walled carbon nanotubes (SWNTs) were achieved by Novotny's group, and the spatial resolution of TERS microscopy reached up to 23 nm.[18] Since then, TERS spectroscopy has taken the full advantage of photons in the structural nano-analysis of materials, and resulting investigation at nano-scale resolution has made possible, for instance, tip-enhanced coherent anti-Stokes Raman analysis of DNA bases,[19] visualization of localized strain on a silicon substrate,[20] diameter-selective imaging of single-walled carbon nanotubes,[21] and investigation of crystalline defects in graphene layers. [22,23]

People who read this introduction up to here may think that TERS microscopy is ready for practical realization. With the spread of nanotechnology research, TERS microscopy is indeed expected to become an indispensable technique for analytical evaluation systems. However, the range of materials and molecular vibrations observable with TERS microscopy is still very restricted due to the originally quite small cross-section of Raman scattering, which is the most important issue in its practical application. As part of research to improve sensitivity, it has been suggested that a specific plasmonic coupling between closely spaced metallic nanostructures is largely responsible for the Raman enhancement observed in the molecules most readily adsorbed in the nanoscopic junctions.[24,25] Based on this hypothesis, TERS using the nanoscopic metallic gap between a metallic tip and a metallic substrate, which is called gap-mode TERS, has been proposed as a form of single-molecule TERS spectroscopy. Although the samples used were admittedly dye molecules with a large Raman cross-section owing to the resonance Raman effect,[26-28] it is nevertheless a fact that gap-mode TERS microscopy is a technique with a high level of sensitivity that has been investigated under many different optical configurations. These investigations have examined the dependence of the gap-mode plasmonic interaction on the distance between the tip and the substrate, [29-31] and on the

polarization direction of the incident light.[32] However, there has not been adequate study of the gap-mode plasmonic effect on the geometry of the metallic substrates and metallic tips, which is important because the plasmonic coupling effect may be significantly associated with unique plasmonic interactions dependent on structures such as nanoparticle-film,[33] nanoparticle-nanowire,[34] and core-shell systems.[35-37]

The aim of the present dissertation is to investigate gap-mode TERS microscopy within the aim of improving its sensitivity. The idea is premised on plasmonic hybridization at the nanometric gap between localized surface plasmons at a metallic tip and continuum surface plasmons on the surface of a metallic thin film. A detailed description of the investigations is presented in the dissertation.

## References


1. E. H. Synge, *Philosophical Magazine*, **6**, 356-362 (1928).
2. A. Lewis, M. Isaacson, A. Harootunian, and A. Muray, *Ultramicroscopy*, **13**, 227-231 (1984).
3. U. C. Fischer and D. W. Pohl, *Phys. Rev. Lett.*, **62**, 458-461 (1989).
4. S. W. Hell and J. Wichmann, *Opt. Lett.*, **19**, 780-782 (1994).
5. E. Betzig, G. H. Patterson, R. Sougrat, O. W. Lindwasser, S. Olenych, J. S. Bonifacino, M. W. Davidson, J. Lippincott-Schwartz, and H. F. Hess, *Science*, **313**, 1642-1645 (2006).
6. M. J. Rust, M. Bates, and X. Zhuang, *Nature Method*, **3**, 793-796 (2006).
7. K. Fujita, M. Kobayashi, S. Kawano, M. Yamanaka, and S. Kawata, *Phys. Rev. Lett.*, **99**, 228105 (2007).
8. Y. Inouye, N. Hayazawa, K. Hayashi, Z. Sekkat, and S. Kawata, *Proc. SPIE*, **3791**, 40-48 (1999).
9. R. M. Stöckle, Y. D. Suh, V. Deckert, and R. Zenobi, *Chem. Phys. Lett.*, **318**, 131-136 (2000).
10. M. S. Anderson, *Appl. Phys. Lett.*, **76**, 3130-3132 (2000).
11. F. Zenhausern, M. P. O'Boyle, and H. K. Wickramasinghe, *Appl. Phys. Lett.*, **65**, 1623-1625 (1994).
12. F. Zenhausern, Y. Martin, and H. K. Wickramasinghe, *Science*, **269**, 1083-1085 (1995).
13. E. J. Sánchez, L. Novotny, and X. S. Xie, *Phys. Rev. Lett.*, **82**, 4014-4017 (1999).
14. H. F. Hamann, A. Gallagher, and D. J. Nesbitt, *Appl. Phys. Lett.*, **76**, 1953-1959 (2000).
15. B. Knoll and F. Keilmann, *Nature,* **399**, 134-137 (1999).
16. R. Hillenbrand, T. Taubner, and F. Keilmann, *Nature*, **418**, 159-162 (2002).
17. N. Hayazawa, Y. Inouye, Z. Sekkat, and S. Kawata, *J. Chem. Phys.*, **117**, 1296-1301 (2002).

18. A. Hartschuh, E. J. Sánchez, X. S. Xie, and L. Novotny, *Phys. Rev. Lett*., **90**, 095503 (2003).
19. T. Ichimura, N. Hayazawa, M. Hashimoto, Y. Inouye, and S. Kawata, *Phys. Rev. Lett.*, **92**, 220801 (2004).
20. N. Hayazawa, M. Motohashi, Y. Saito, H. Ishitobi, A. Ono, T. Ichimura, P. Verma, and S. Kawata, *J. Raman Spectrosc*., **38**, 684-696 (2007).
21. T. Yano, P. Verma, S. Kawata, and Y. Inouye, *Appl. Phys. Lett*., **88**, 093125 (2006).
22. Y. Saito, P. Verma, K. Masui, Y. Inouye, and S. Kawata, *J. Raman Spectrosc*., **40**, 1434-1440 (2009).
23. J. Stadler, T. Schmid, and R. Zenobi, *Nano Lett*., **5**, 8442-8448 (2011).
24. K. Kneipp, Y. Wang, H. Kneipp, L. T. Perelman, I. Itzkan, R. R. Dasari, and M. S. Field, *Phys. Rev. Lett.*, **78**, 1667-1670 (1997).
25. S. Nie and S. R. Emory, *Science*, **275**, 1102-1106 (1997).
26. C. C. Neacsu, J. Dreyer, N. Behr, and M. B. Raschke, *Phys. Rev. B*, **73**, 193406 (2006).
27. K. F. Domke, D. Zhang, and B. Pettinger, *J. Am. Chem. Soc.*, **128**, 14721-14727 (2006).
28. W. Zhang, B. S. Yeo, T. Schmid, and R. Zenobi, *J. Phys. Chem. C*, **111**, 1733-1738 (2007).
29. B. Pettinger, K. F. Domke, D. Zhang, G. Picardi, and R. Schuster, *Surf. Sci*., **603**, 1335-1341 (2009).
30. R. M. Roth, N. C. Panoiu, M. M. Adams, R. M. Osgood, Jr., C. C. Neacsu, and M. B. Raschke, *Opt. Express*, **14**, 2921-2931 (2006).
31. T. Yano, T. Ichimura, A. Taguchi, N. Hayazawa, P. Verma, Y. Inouye, and S. Kawata, *Appl. Phys. Lett.*, **91**, 121101 (2007).
32. N. Hayazawa, H. Ishitobi, A. Taguchi, A. Tarun, K. Ikeda, and S. Kawata, *Jpn. J. Appl. Phys.*, **46**, 7995-7999 (2007).
33. F. Le, N. Z. Lwin, J. M. Steele, M. Käll, N. J. Halas, and P. Nordlander, *Nano Lett.*, **5**, 2009-2013 (2005).
34. F. Hao and P. Nordlander, *Appl. Phys. Lett.*, **89**, 103101 (2006).
35. S. J. Oldenburg, R. D. Averitt, S. L. Westcott, and N. J. Halas, *Chem. Phys. Lett*., **288**, 243-247 (1998).
36. E. Prodan, C. Radloff, N. J. Halas, and P. Nordlander, *Science*, **302**, 419-422 (2003).
37. J. A. Fan, C. Wu, K. Bao, J. Bao, R. Bardhan, N. J. Halas, V. N. Manoharan, P. Nordlander, G. Shvets, and F. Capasso, *Science*, **328**, 1135-1138 (2010).

## Organization of this dissertation

In this dissertation, I discuss plasmon hybridization between a metallic tip and a metallic film, and tip-enhanced Raman scattering spectroscopy utilizing the plasmon hybridization effects at the gap of a tip-film system. For the discussion, this dissertation is organized as follows.

In Chapter 1, I give fundamental concepts of Raman spectroscopy and microscopy. Chapter 2 explains that the enhancement of Raman scattering by metallic nanostructures, in which necessary ideas in the discussion on surface plasmon polaritons and tip-enhanced Raman scattering (TERS) are provided. Then, I discuss TERS spectroscopy and microscopy through nanoscale Raman analysis of graphene and single-walled carbon nanotubes in Chapter 3 and 4, where the current situation and challenges in TERS spectroscopy are argued. For solving the challenges, I show the idea of plasmon hybridization between a metallic tip and a metallic film in Chapter 5. I aim to make readers comprehend physics in the plasmon hybridization by presenting the theory, numerical calculation and experimental results. Finally, I show results of TERS measurements utilizing the phenomenon of the plasmon hybridization in Chapter 6. I discuss what is improved and what is expected with the usage of plasmon hybridization effects.

# Chapter 1.
# Raman spectroscopy and microscopy

This chapter presents the reason why Raman spectroscopy has been utilized for studying the molecular structure determination in condensed matter physics, materials physics, bioscience, and other related science fields. The answer is that a Raman spectrum of materials has rich information of molecular vibrations of the materials. In Chapter 3 and 4, I will actually demonstrate the Raman analysis of carbon-based nanomaterials. To gain a clear understanding of Raman scattering process, I focus on the optical processes under the broad heading of light-matter interaction phenomena. In the first of this chapter, the principle of Raman scattering is briefly explained from the classical and quantum point of view, and the root of Raman spectrum known as "molecular fingerprint" is expounded. After the basic introduction, I represent optical system for Raman spectroscopy and microscopy to analyze Raman scattering from a sample.

## 1.1
## Fundamentals of Raman scattering

Light scattering provides quite useful information to study fundamental interactions between light and materials, because light can be scattered inelastically so that the incident photons and scattered photons have different energy. The difference of the energy corresponds to energy of molecular vibrations associated with atomic arrangement of the materials, therefore the inelastic scattering light reflects on structural information of the materials. The inelastic scattering of light is called Raman scattering, discovered by C. V. Raman in 1928.[1] In the primary method of Raman scattering measurement, he irradiated samples with sunlight focused by means of a telescope through a filter, and directly observed the secondary scattered light from the samples. After the first discovery of Raman scattering, the number of research groups who have studied Raman scattering runs into hundreds of

thousands. In the current era, Raman scattering has found huge applications not only in physics, but also in bioscience, electrical engineering, mechanical engineering, and other fields.

Raman scattering can be interpreted by the classical theory and quantum theory. The former helps us to understand basic concepts of Raman scattering intuitively, and the latter is necessary to discuss about two-photon process of Raman scattering. First, I explain the classical theory to catch fundamental phenomena in Raman scattering, and then move to the quantum theory in which transition probability of molecular vibrational states is contextualized. Finally, Raman selection rules that are a condition for generating Raman scattering are briefly discussed.

**Classical theory**

In Raman process, incident light reaches a molecule and is inelastically scattered. The inelastic scattering is attributed to an interaction in which electromagnetic field of the incident light shakes electrons in the molecule. The oscillation of the electrons is perturbed by molecular vibrations within displacements of atoms at the different positions in the molecule. The ability to oscillate the electrons is defined as polarizability, and the polarizability of molecules depends on chemical and structural properties of the molecules. Since every material has a unique set of the molecular structure, the inelastic scattering light also represents a distinct spectral pattern depending on the each material. Hence, Raman scattering light can be utilized to characterize materials properties in the molecular level.

In the description of Raman scattering, polarizability of materials is needed to describe. Given a polarizability tensor $\boldsymbol{\alpha}$ of an atom in a material, a polarization $\boldsymbol{P}$ of the atom in an electric field $\boldsymbol{E}$ is written as

$$\boldsymbol{P} = \boldsymbol{\alpha} \cdot \boldsymbol{E} \tag{1.1}$$

where the electric field is oscillating at an optical frequency $\omega_i$, then the electric field is given as

$$\boldsymbol{E} = \boldsymbol{E}_0 \sin \omega_i t \tag{1.2}$$

Since the polarizability of the atom is oscillating according to the lattice vibration in the material, the polarizability is modulated by

$$\boldsymbol{\alpha} = \boldsymbol{\alpha}_0 + \boldsymbol{\alpha}_1 \sin \omega_q t \tag{1.3}$$

where $\omega_q$ is an optical phonon mode frequency of the material that couples to optical field of the incident light. As a result, the polarization induced by the applied electric field is described as

$$\begin{aligned} \boldsymbol{P} &= \boldsymbol{E}_0(\boldsymbol{\alpha}_0 + \boldsymbol{\alpha}_1 \sin\omega_q t)\sin\omega_0 t \\ &= \boldsymbol{E}_0\left[\boldsymbol{\alpha}_0 \sin(\omega_i t) + \frac{1}{2}\boldsymbol{\alpha}_1 \cos(\omega_i - \omega_q)t - \frac{1}{2}\boldsymbol{\alpha}_1 \cos(\omega_i + \omega_q)t\right] \end{aligned} \quad (1.4)$$

Thus, the incident photon is scattered with a couple of frequencies according to the polarizability of the atom. The first term in Eq. (1.4) is defined as Rayleigh scattering, and the second and third terms are Raman scattering classified as Stokes and anti-Stokes scattering, respectively. Figure 1.1 is a schematic image of a typical Raman spectrum from a material. Raman spectra are described by energy shift of the Raman scattered photon from the incident photon. The strong peak in the center is associated with the Rayleigh scattering, and the other peaks are due to the Raman scattering. Since a material has the several molecular vibration modes such as longitudinal optical (LO) and transverse optical (TO) phonons, multiple Raman peaks are usually observed. Since every material has a unique set of the molecular vibration modes, Raman scattering is often called "molecular fingerprint". With the practical analysis of Raman peaks, we can identify the nature of the materials. The lineshape of Raman peaks usually shows a Lorentzian curve because the molecular vibrations can be represented as a damped harmonic oscillator with the phonon frequency. Considering the damping

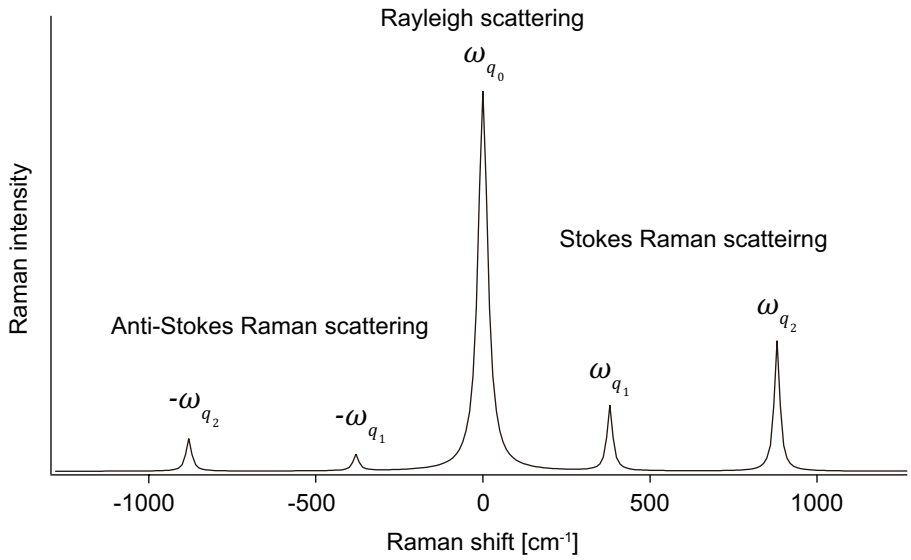


**Figure 1.1** Schematic image of a typical Raman spectrum.

energy given by $\tau_q$, a Lorentzian curve is described as

$$I(\omega) = \frac{I_0}{\pi\tau_q}\frac{1}{(\omega-\omega_q)^2+\tau_q^2} \tag{1.5}$$

The full width at half maximum (FWHM) intensity is given by $2\tau_q$. The damping energy $\tau_q$ indicates the inverse of the lifetime for a phonon,[2] therefore Raman spectra also provide information on the phonon lifetimes. When several peaks are overlapped each other, those peaks can be separated and analyzed using the multi peak fitting of Lorentzian curves.

**Quantum theory**

In a quantum description of Raman scattering, state transition of molecular vibrations from an initial state to a final state has to be discussed considering an intermediate state. Raman scattering process takes place by an intermediary of incident photon and scattering photon, and the transition of the vibrational states can occur through both creation and annihilation of the photons. Figure 1.2 is an excitation process diagram of Raman scattering, where an initial state, an intermediate state, and a final state of a molecule are described by $|m\rangle$, $|e\rangle$, $|n\rangle$, respectively. Furthermore, I define vibrational states of a molecule as $|m)$ for the ground state and $|n)$ for the excited state, and also the electric ground states as $|g]$ having the energy $\hbar\omega_g$. According to Born-Oppenheimer approximation, I can describe electron motion and atomic motion in the system independently, thus I indicate an initial state $|m\rangle$ and a final state $|n\rangle$ of molecular state as

$$|m\rangle = |g]|m)$$

$$|n\rangle = |g]|n)$$

In a same way, an intermediate state $|e\rangle$ of the molecular vibrations is depicted as

$$|e\rangle = |e]|v)$$

where $|e]$ indicates any excited electric states having the energy $\hbar\omega_e$ except the ground state, and $|v)$ is the intermediate vibrational state. In Raman process, a vibrational ground state is excited to a vibrational excited state in the same electronic level through an intermediate state, in which an incident photon is annihilated and a scattering photon is created, as illustrated in Fig. 1.2. The intermediate state does not need to be a real state and can exist just at a given instant as a transient response,

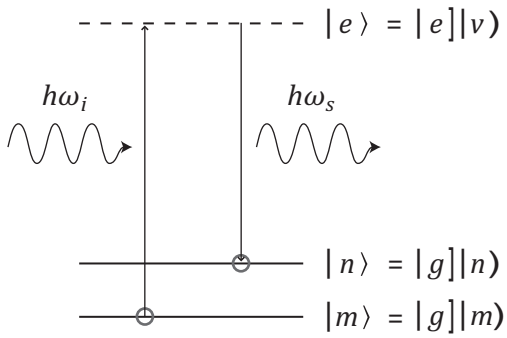


**Figure 1.2** Excitation process diagram of Raman scattering. $\hbar\omega_i$ and $\hbar\omega_s$ are energies of the incident photon and scattering photon, respectively.

and therefore it is usually called virtual state and drawn with a dashed line. Since the creation and annihilation of photons must be simultaneously done, Raman scattering process is considered as two-photon scattering process. That's why cross section of Raman scattering is extremely small (~$10^{-30}$ $cm^2$) comparing with other one-photon optical processes such as fluorescence (~$10^{-16}$ $cm^2$).

I express the Raman scattering intensity using above premise. In quantum theory, intensity of light is defined by photon flux which is the number of photons passing through a unit area for a unit time. Given scattering photon flux $F_{k_s e_s}$ having the wavenumber $k_s$ and the coordinate $e_s$ is generated by incident photon flux $F_{k_i e_i}$ interacted with a material, then the scattering photon flux from the material at a distance $R$ is described as

$$F_{k_s e_s} R^2 = \left(\frac{\mathrm{d}\sigma}{\mathrm{d}\Omega}\right)_{m\to n} F_{k_i e_i} \tag{1.6}$$

where $(d\sigma/d\Omega)_{m\to n}$ is differential cross section of the Raman scattering from $|m\rangle$ state transited to $|n\rangle$ state at a molecular position $\sigma$. Here, the cross section is described as

$$\left(\frac{\mathrm{d}\sigma}{\mathrm{d}\Omega}\right)_{m\to n} = \frac{16\pi^4 \omega_s^3 \omega_i}{c^4} \left| \sum_{\rho,\sigma} (\boldsymbol{\rho}\cdot\boldsymbol{e}_s)(\boldsymbol{\sigma}\cdot\boldsymbol{e}_i)\, \alpha_{\rho\sigma} \right|^2 \tag{1.7}$$

where $\omega_s$ and $\omega_i$ are frequency of the scattering light and the incident light, respectively. And, $\boldsymbol{\sigma}$ and $\boldsymbol{\rho}$ are unit vectors with the direction of $x$, $y$, or $z$. $\alpha_{\rho\sigma}$ is Raman tensor indicating the $\rho\sigma$ components. As you can simply understand, the cross section raises up with the use of photon having higher energy. To solve the Raman tensor $\alpha_{\rho\sigma}$, the second order time-dependent perturbation theory is introduced under a condition that the population at the final state $|n\rangle$ is supposed to zero at the initial

condition. Moreover, I assume that Raman excitation energy $\hbar\omega_i$ is much smaller than any electron transitions of a molecule and the electronic ground state is not degenerated (Placzek approximation[1]). Finally, the Raman tensor $\alpha_{\rho\sigma}$ is described as

$$\alpha_{\rho\sigma} = \sum_{e \neq g} \left\{ \frac{[g|D_\sigma|e][e|D_\rho|g]}{\hbar(\omega_e - \omega_g - \omega_i)} + \frac{[g|D_\rho|e][e|D_\sigma|g]}{\hbar(\omega_e - \omega_g + \omega_i)} \right\} \tag{1.8}$$

where $D_\sigma$ and $D_\rho$ are $\sigma$ and $\rho$ components of dipole moments $\boldsymbol{D}$ of materials, respectively. In Placzek approximation, the Raman tensor is expressed by the sum of a symmetric operation of an eigenstate of the electronic state from the initial state $|m\rangle$ and the final state $|n\rangle$, where contribution of vibrational states is negligible. Namely, Raman tensor of the molecule is approximated to be the polarizability tensor. In summary of the quantum theory, Raman scattering is described as a sum of the transition probability between eigenstates of electronic states of a molecule due to an interaction between photon and the molecule.

**Selection rules of Raman scattering**

In Raman scattering, any molecular vibration modes in a molecule are not always excited by photon irradiation. This is because the molecular vibrations need to be associated with change of the polarizability. For discussion of the relationship between molecular vibrations and the polarizability, group theory is useful for the description. Here, I leave the detail discussion of group theory on textbooks,[3] but I give some of the fundamentals. According to group theory, a molecular vibration mode can be expressed as basis of an irreducible representation of symmetric operation corresponding to a point group of the molecules. It decides if vibrational modes of molecules are active or inactive on the Raman scattering, thus giving Raman selection rules. In fact, molecular vibrations with symmetry perturbing polarizability of the molecule at an equilibrium position of nucleus, which is often described as totally symmetric modes, indicate Raman active. For assignments of Raman scattering peaks observed from molecules to particular molecular vibration modes, Raman selection rules and group theory play an important role. In the practical way to describe symmetry of a molecule, a character table based on the molecular structure is utilized.[3] Furthermore, frequency of each molecular vibration is also able to be estimated by using the character table and some of the molecular information such as the lattice constant and the molecular mass.

## 1.2
## Optical system for Raman spectroscopy/microscopy

I provide an overview of Raman spectroscopy/microscopy following the basic concepts of Raman scattering discussed above. As I have discussed, materials can be identified by analysis of the vibrational modes observed in Raman spectra from the materials. Since the vibrational modes are obtained from the Raman peaks, dispersion of photon energy of Raman scattering light should be narrow enough to resolve the each Raman peak. In this sense, laser light having narrow energy dispersion is usually utilized for Raman spectroscopy/microscopy.

Figure 1.3 shows an optical setup for Raman spectroscopy/microscopy which I use in this thesis. First, laser beam is collimated with a beam expander, and polarization of the laser light is adjusted by a half wave plate and a polarizer. Then, the laser light is introduced into an inverted objective lens as Raman excitation light. A sample is illuminated by the light focused by the objective lens with the numerical aperture (NA) equal to 1.4 and the magnification factor of 60 (Nikon, Plan Apo). The sample is set on a piezoelectric transducer (PZT) stage, and position of the sample is precisely controlled by the PZT stage. Raman scattering light from the sample is collected by the same objective lens, and passes through an edge filter suitable for the excitation laser, in which light having shorter wavelength than excitation light is selectively cut. The extracted Raman scattering light is lead to a spectrometer by an achromatic lens through a slit. Note that size of the slit decides the spectral resolution. The Raman scattering is dispersed by a grating equipped in the spectrometer, and focused on a liquid nitrogen cooled CCD camera (Roper, 1340 × 400 channel, -100 Cº). The grating has blaze

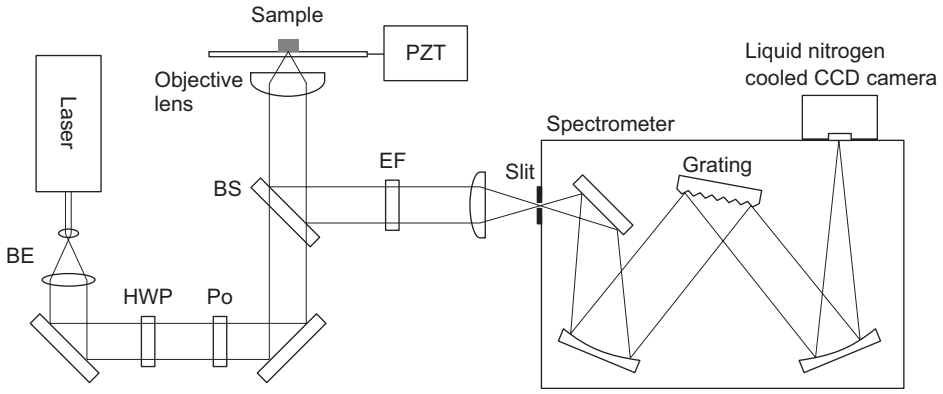


**Figure 1.3** Optical system for Raman spectroscopy/microscopy. BE is a beam expander, HWP is a half wave plate, Po is a polarizer, BS is a beam splitter, and EF is an edge filter.

wavelength of 600 and 1200 lines/mm that is chosen according to the necessary spectral resolution. For the Raman microscopy, Raman scattering from the sample is detected point by point with Raster scanning over the sample, and the Raman image is analytically constructed.

Since Raman microscopy is based upon optical microscopy, the spatial resolution is limited due to wave nature of light. Light traveling through a lens makes a spot whose size is decided in association with wavelength $\lambda$ of the light and numerical aperture ($NA$) of the lens. The spatial resolution is provided as

$$x = 0.61\frac{\lambda}{NA} \tag{1.9}$$

As one can understand, the resolution directly depends on the wavelength and the numerical aperture. Considering the range of visible light is from 400 nm to 800 nm and capability of numerical aperture is up to about 1.5, the highest resolution is restricted to ~ 160 nm. This limitation of spatial resolution of optical microscopy is so-called diffraction limit.

## Summary

I have given a broad perspective on how Raman spectroscopy provided an especially sensitive characterization tool for the analysis of materials. I have explained fundamental physics of Raman scattering through a perspective of the classical and quantum theory, where the relationship between Raman scattering and molecular vibrations was expounded. I also briefly introduced Raman selection rules for understanding a fundamental concept to assign Raman peaks to particular molecular vibrational modes of the materials. After the basic introduction, I represented optical system for Raman spectroscopy and microscopy to analyze Raman scattering from a sample.

## References

1. 濱口宏夫, 平川暁子, ラマン分光法, 学会出版センター (1988).
2. R. R. Alfano, and S. I. Shapiro, *Phys. Rev. Lett.*, **26**, 1247-1251 (1971).
3. F. Albert Cotton, *Chemical Applications of Group Theory Second Edition*, 丸善 (1985).

# Chapter 2.
# Enhancement of Raman scattering by a metallic nanostructure

Since cross section of spontaneous Raman scattering is extremely low, the lowest detectable number of molecules is limited even though the detector performance has been well developed. The scattering efficiency from a material can be dramatically enhanced in the close vicinity of metal nanostructures up to single-molecule detection level, which is called surface enhanced Raman scattering (SERS) effect. In this chapter, I start by explaining an electromagnetic field generated on surfaces of metal nanostructures under light illumination and what happens in Raman scattering when a molecule is placed in the field. Then, I present fundamental concepts of tip-enhanced Raman scattering (TERS) induced at a nanometric metallic tip apex as localized SERS. Furthermore, chemical effect in SERS between a metal and a molecule is described according to the experimental results. Finally, field enhancement in a nano gap between metallic nanostructures is shown, and the advantages of the gap for SERS measurement are discussed.

## 2.1
## Surface enhanced Raman scattering

Surface enhanced Raman scattering from a material can be caused when the material is irradiated by light near a metal surface. The enhancement of Raman scattering is attributed to an enhanced electromagnetic field of light generated on a metal surface through a resonant electron oscillation on the metal surface. At the beginning of the interpretation of the field enhancement, I discuss an interaction between photons and electrons near a metal surface. As long free electron model in metals, that is Drude model, the electrons collectively oscillate like a plasma of an electron gas. The elementary

excitation associated with such a collective oscillation of a plasma wave is quantized as 'plasmon'. Plasmon in bulk materials does not interact with photon because plasmon is based on longitudinal wave that never couple to transversal wave of photon. However, plasmon on an interface between a metal and a dielectric medium can couple with photon under a satisfied boundary condition depending on dielectric functions of the metal and medium. Such plasmons coupling with photon on metal surfaces are called surface plasmon polaritons (SPPs), and resonant excitation of SPPs induces field enhancement of light on the metal surface. The physical properties of SPPs are discussed in the case of a metallic substrate and a metallic nanoparticle, respectively. In calculation, SI units are utilized.

**Surface plasmon polaritons on a metal substrate**

Fundamental behavior of SPPs is understood by a dispersion relationship at an interface between a dielectric and a metal. Figure 2.1 shows a schematic illustration of surface electromagnetic wave existing at an interface of a dielectric and a metal with the dielectric function of $\varepsilon_1(\omega)$ and $\varepsilon_2(\omega)$, respectively. Electric fields of the surface wave along *x* and *z* directions in the two media are described by $E_{1x}$, $E_{1z}$ and $E_{2x}$, $E_{2z}$, respectively. $k_{1z}$ and $k_{2z}$ stand for the wavenumber of the surface wave along *z* direction, and the wavenumber along *x* direction is described by $k_x$ under phase matching condition between the two media. The solution of the surface wave that fulfills the boundary conditions for the tangential components of the electric field and the normal component of the electronic displacement exhibits the following forms as

$$E_{1x} = E_{2x} \tag{2.1}$$

$$\varepsilon_1(\omega)E_{1z} = -\varepsilon_2(\omega)E_{2z} \tag{2.2}$$

With Maxwell equations, Eq. (2.1) and Eq. (2.2) can be converted into

$$\frac{k_{1z}}{\varepsilon_1(\omega)} + \frac{k_{2z}}{\varepsilon_2(\omega)} = 0 \tag{2.3}$$

I generalize a dispersion relationship of the surface wave by wavenumber of light. Assuming wavenumbers of light in vacuum is *k*, wavenumbers of the surface wave are conserved at the interface as

$$k_x^2 + k_{1z}^2 = \varepsilon_1(\omega)k^2 \tag{2.4}$$

$$k_x^2 + k_{2z}^2 = \varepsilon_2(\omega)k^2 \tag{2.5}$$

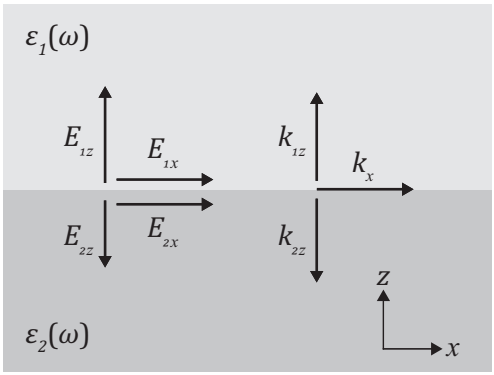


**Figure 2.1** Schematic illustration of surface electromagnetic wave at an interface of two media $\varepsilon_1(\omega)$ and $\varepsilon_2(\omega)$.

Thus, the following dispersion relation reads

$$k_x^2 = \frac{\varepsilon_1(\omega)\varepsilon_2(\omega)}{\varepsilon_1(\omega) + \varepsilon_2(\omega)} k^2 \tag{2.6}$$

Here, I suppose that medium 1 has the dielectric constant which hardly change in visible range of light as $\varepsilon_1(\omega) = \varepsilon_m$, and medium 2 is a metal substrate with the dielectric function following Drude model neglecting the damping loss of electrons as $\varepsilon_2(\omega) = 1 - \omega_p^2/\omega^2$, where $\omega_p$ is plasma frequency of the metal. The dispersion relation of the surface plasmons is solved and expressed as shown in Fig. 2.2. The dispersion curve of the surface plasmons has two asymptotic lines. The one asymptotic line given at $\omega \to 0$ is obtained as $k_x = (\omega/c)\sqrt{\varepsilon_m}$, and this dispersion curve corresponds to dispersion relation of light. The other asymptotic line is given when $\omega \to \omega_p/\sqrt{1+\varepsilon_m}$. The latter line means that wavenumber of the surface plasmons diverges to infinity as the frequency approaches the asymptotic energy while keeping the energy. In other words, the wavelength of the surface plasmons goes to infinitely small value at the asymptotic line.

Next, I discuss the way to excite surface plasmons by light irradiation. Propagation light cannot directly excite surface plasmons with any excitation wavelength due to phase mismatch between them. It is clear that dispersion relation of surface plasmons does not have any common points with that of light as shown in Fig. 2.2. To excite surface plasmons with the use of light, we can utilize evanescent waves that have higher wavenumber components than propagating light wave. Evanescent waves can be generated on a medium boundary under total reflection condition, and intensity of the evanescent waves exhibits exponential decay with a distance from the boundary. I explain the method to excite surface plasmons by evanescent waves.

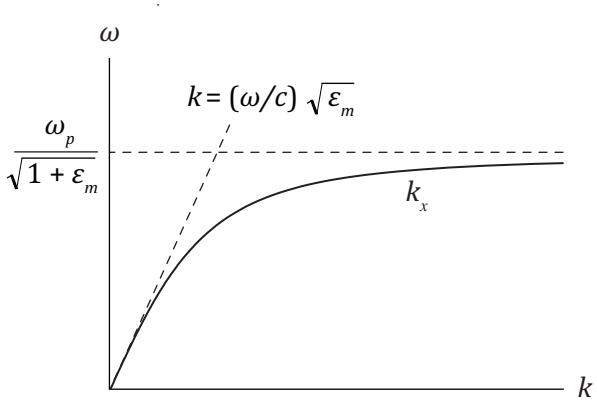


**Figure 2.2** Dispersion relation of surface plasmons and light. The black dotted lines indicate asymptotic lines for the dispersion relation. The equation $k_x = (\omega/c)\sqrt{\varepsilon_m}$ corresponds to dispersion relation of light.

I consider a configuration that consists of three layers of air $\varepsilon_0$, metal $\varepsilon(\omega)$ and glass $\varepsilon_m$ as shown in Fig. 2.3(a). TM-polarized light is irradiated to the metal substrate from the glass side with the incident angle of $\theta$. In this configuration, evanescent waves can be generated on the medium boundary under total internal reflection condition, and intensity of the evanescent waves exhibits exponential decay with a distance from the boundary. Referring to Eq. (2.6), dispersion relation of surface plasmons at the interface of metal-air and metal-glass can be expressed as shown in Fig. 2.3(b). Light lines of the incident light propagating in air and glass are also shown. Now, I focus on an area between the two light lines in air and glass as shown in the gray-filled area in Fig. 2.3(b). In that area, propagation light in the glass is totally reflected at the metal-glass interface, and evanescent waves are generated at the interface. The evanescent waves penetrate into the metal substrate, and can interact with surface plasmons at the metal-air interface. When phase of the evanescent waves matches with that of surface plasmons under $k_{sp} = \left(\frac{\omega}{c}\right)\sqrt{\varepsilon_m}\sin\theta$, the surface plasmons couple with the evanescent waves and SPPs are created on the air-metal surface. The SPPs propagate along the interface with decaying the intensity, and electromagnetic fields generated by the SPPs are located near the surface. The propagation length is usually a few micrometer, and it depends on damping constant of the electron scattering in the metal and disorganized roughness on the metal surface. The configuration based on this total internal reflection for exciting SPPs as shown in Fig. 2.3(a) is suggested in 1968, and called as *Kretschmann* configuration.[1]

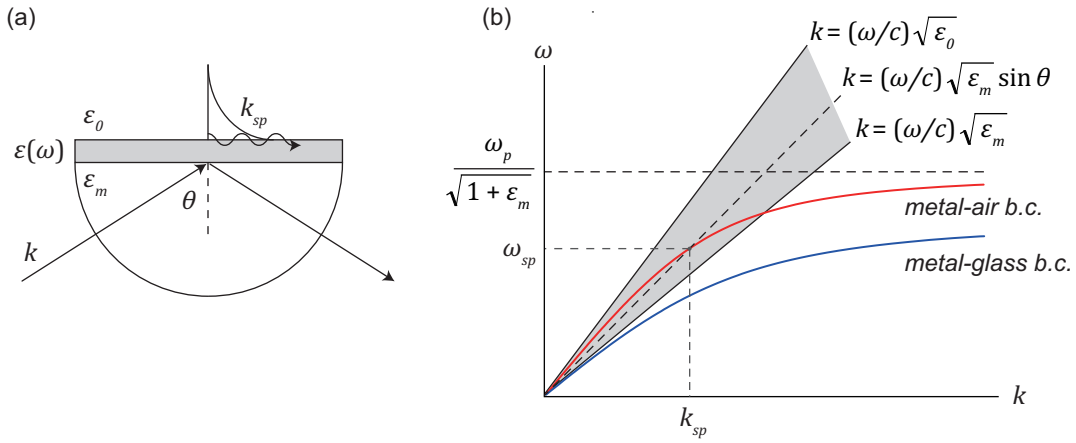


**Figure 2.3** (a) Schematic illustration of ATR based on *Kretschmann* configuration. (b) Dispersion relations of surface plasmons at the boundaries of (red) metal-air and (blue) metal-glass.

Here, I contemplate electromagnetic fields generated by SPPs with the basis of the velocity. Given that velocity of energy propagation of light is described as the group velocity, velocity $v_e$ of SPPs is written by

$$v_e = \frac{\mathrm{d}\omega}{\mathrm{d}k} \tag{2.7}$$

Comparing the group velocity of SPPs with that of propagation light in Fig. 2.3(b), the velocity of SPPs is slower than that of the light. In this sense, SPPs are often called 'slow light'.[2] What does the slow velocity of SPPs actually indicate? This phenomenon means that the electromagnetic energy of SPPs is condensed in the propagating direction according to the wavelength getting short. Or from a quantum point of view, slow light can be understood as an increase of the number of photon in a unit volume. As a result, field intensity of light is enhanced on a metal surface when the light properly excites SPPs. The enhancement factor is defined by the intensity ratio of the enhanced field to the incident light field. For instance, supposing a metal substrate in Fig. 2.3(a) is gold with the thickness of 50 nm and the excitation wavelength is 633 nm, the enhancement factor is estimated to be ~ 26. If Raman scattering is excited adjacent to the metal substrate under the condition, field of the scattering light is dramatically increased by the field enhancement. The field enhancement effect associated with SPPs is the root of electromagnetic effect in SERS spectroscopy.

**Localized surface plasmon of a metallic nanostructure**

I now turn to plasmonic excitations in a metal nanostructure. When a metallic nanoparticle is irradiated with light, electromagnetic field of the light easily penetrates over the metallic nanoparticle and induces an oscillation of electrons in the nanoparticle. The result is that the electrons are displaced with respect to the positively charged ions that form the metallic nanoparticle (See Fig. 2.4). The resulting electric dipole on the nanoparticle represents a restoring force and hence the nanoparticle can be considered as a harmonic oscillator, driven by a light wave and damped by some losses such as ohmic losses and radiative losses. The surface plasmons can be localized adjacent to surface of the metallic nanoparticle, and such surface plasmons are called as localized surface plasmons. Unlike surface plasmons on a metal surface, localized surface plasmons on a metallic nanoparticle can couple with an electromagnetic field of propagating light.

The behavior of localized surface plasmons is dealt with as an electrostatic problem, assuming diameter of a metallic nanoparticle is much smaller than wavelength of the excitation light. In an electromagnetic field of light, a metallic nanoparticle takes a charge distribution associated with the external field and forms depolarization field $E_1$ in itself that behaves to negate the electric field in the nanoparticle as shown in Fig. 2.4. Here, an electrostatic problem is appropriable to discussion of the depolarization field on the nanoparticle when the external electric field is presumed to be constant without time retardation of the electron motion over the nanoparticle having the diameter much smaller than wavelength of the light. The polarization $P$ inside the nanoparticle is described as

$$P = xE \tag{2.8}$$

where $x$ and $E$ denote electric susceptibility and internal electric field in the nanoparticle, respectively. The internal electric field of the nanoparticle is obtained from the sum of the depolarization field and the external field, and given by

$$E = E_0 + E_1 = E_0 - NP \tag{2.9}$$

where $N$ is a depolarization coefficient that depends on geometry of the nanostructure. After substitution of Eq. (2.8), the depolarization field is written as

$$P = \frac{x}{1 + Nx} E_0 \tag{2.10}$$

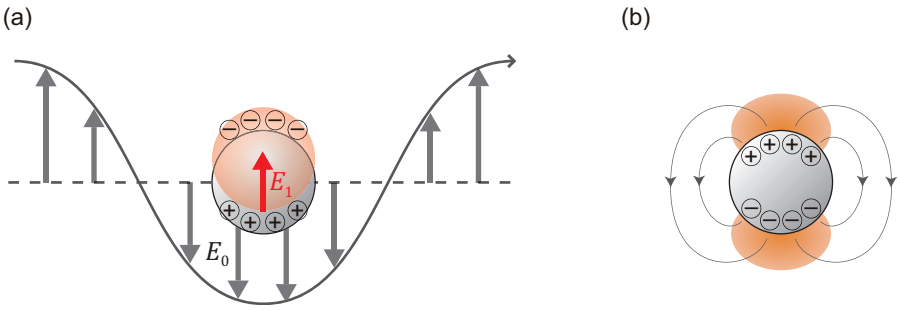


**Figure 2.4** Schematic images of (a) depolarization field induced inside a metallic nanoparticle, and (b) field enhancement formed in the vicinity of a metallic nanoparticle.

If the metallic nanoparticle is set in a medium that has a dielectric function $\varepsilon_m$, dielectric function $\varepsilon(\omega)$ of the nanoparticle is affected by the electric susceptibility and is satisfied with the following equation $\varepsilon(\omega) = \varepsilon_m(1 + 4\pi x)$. Moreover, the depolarization coefficient $N$ for a nanoparticle is given by $\frac{1}{a^2}\int_0^{\pi} 2\pi \cos^2\theta \sin\theta \, d\theta = 4\pi/3$. As a result, dipole moment $p$ of the metallic nanoparticle with the diameter of $a$ is derived as

$$p = PV = \frac{\varepsilon(\omega) - \varepsilon_m}{\varepsilon(\omega) + 2\varepsilon_m} a^3 E_0 \tag{2.11}$$

From Eq. (2.11), it is clear that amplitude of dipole moment of the nanoparticle depends on a frequency of the external electric field. In particular, the dipole moment goes to infinity when the denominator is close to zero. That is, an extremely strong electric field can be resonantly induced around the surroundings of the nanoparticle under the condition of $\varepsilon(\omega) = -2\varepsilon_m$. The electric field induced around the metallic nanoparticle forms a confined electromagnetic field in the close vicinity of the metallic nanoparticle as shown in Fig. 2.4(b). The resonant condition relies on a dielectric function of the metal, therefore silver,[3] gold,[4] and aluminum[5] nanoparticles have been utilized according to the desirable resonance wavelength. For the detail discussion of resonance energy of the localized SPPs, Drude model can be not suitable for the description of the dielectric function of metal, because Drude model cannot perfectly represent behavior of the electrons associated with electron transition in metal. To estimate the resonance energy, it is preferred to use a dielectric function obtained from the experimental observation such as Johnson and Christy parameters.[6] Note that Eq. (2.11) is applicable only to the lowest order dipole mode in a nanoparticle, not applicable to quadrupole, or octupole. Those multipole modes are caused by the retardation of the electron oscillation

to the external field.[7] The lowest mode is called Fröhlich mode,[8] and Fröhlich mode is more dominant when a nanoparticle is getting small.

Field enhancement around a metallic nanoparticle is estimated from Eq. (2.11) and an electric field resulting from a dipole radiation. The electric field intensity from a dipole radiation of a metallic nanoparticle in an electrostatic field is written as

$$E = pE_0 \left[ 2\cos\theta \left( \frac{1}{r^3} \right) \right] \tag{2.12}$$

where $r$ is a distance from the dipole. The maximum field intensity from the dipole on surface of the nanoparticle is given at $\theta = 0$ and $r = a$ therefore, the maximum field intensity is described as

$$E = 2\frac{\varepsilon(\omega) - \varepsilon_m}{\varepsilon(\omega) + 2\varepsilon_m} E_0 \tag{2.13}$$

Here, assuming dielectric function of the metal is written as $\varepsilon(\omega) = \varepsilon' + i\varepsilon''$, an intensity ratio of the enhanced field to the incident field under the resonance condition $\varepsilon' + 2\varepsilon_m = 0$ is simply expressed by

$$\eta_{\max} = \left| \frac{E}{E_0} \right| = 3 \left| \frac{\varepsilon'}{\varepsilon''} \right| \tag{2.14}$$

The thing is that the field enhancement takes the larger value as the absolute value of the real part is larger and the absolute value of the imaginary part is smaller. If I qualitatively explain the physical meaning, it indicates that the slower light on a surface of the nanoparticle and a smaller damping constant of the electron oscillation in the nanoparticle give the stronger field enhancement. The $\eta_{\max}$ is commonly utilized as an enhancement factor for describing the degree of the enhancement.

In Raman scattering excited near a metallic nanoparticle, the field enhancement effect acts on the both incident light and scattering light. First, an electromagnetic field of the incident light is enhanced by a metallic nanoparticle, and the enhanced field excites SERS from a molecule adjacent to the nanoparticle. The SERS interacts with the metallic nanoparticle, and the SERS is enhanced as well. Therefore, enhancement factor of the Raman scattering occurred near a metallic nanoparticle is described by

$$\eta_{\text{Raman}} = \left| \frac{\eta(\omega_i) E_i}{E_i} \right|^2 \left| \frac{\eta(\omega_s) E_s}{E_s} \right|^2 = \eta^2(\omega_i)\, \eta^2(\omega_s) \tag{2.15}$$

where $E_i$, $\omega_i$ and $E_s$, $\omega_s$ stand for electric field and frequency of the incident and Raman scattering light, respectively. $\eta(\omega)$ represents the field enhancement factor of light at a certain frequency $\omega$. Given the difference between frequency of the incident light and that of Raman scattering light is as small as a tithe part of their frequency, Eq. (2.15) can be simplified as

$$\eta_{\text{Raman}} = \eta^4(\omega_i) \tag{2.16}$$

Thus, Raman enhancement factor of SERS by a metallic nanoparticle is depicted by the fourth power of the field enhancement. Raman enhancement factor is estimated by comparing intensity of spontaneous Raman scattering with that of SERS in a unit volume. The field enhancement factor can be estimated from the forth root of the Raman enhancement factor according to Eq. (2.16).

The resonance wavelength of localized SPPs in metallic nanostructures is essentially dependent on the geometry and the material because allowed electron distribution inside them is decided by their physical properties. Therefore, when the metallic nanostructure has complicated geometries, analytical calculation for the localized SPPs is not applicable. Instead, numerical analysis is a powerful tool to approximate resonance wavelength of localized SPPs of intricate nanostructures. Some of the numerical approaches have been proposed as finite-difference time-domain (FDTD) method,[9] discrete dipole approximation (DDA),[10,11] and finite element method (FEM).[12] Among them, FDTD method is commonly utilized because it is facile to build the simulation algorithm and applicable to complicated geometries. In FDTD method, electromagnetic fields in an arbitrary 3D (or 2D) space divided into a unit grid (so-called Yee grid) are consecutively calculated in time domain according to the discretized Maxwell equations. The electric field vector components in a unit volume are solved at a given point in time, and then the magnetic field components in the same unit volume are solved at the next point in time. The calculation is continuously repeated until the electromagnetic field takes the stable equilibrium condition. By introducing materials with the arbitrary geometry in the arbitrary space and incident electromagnetic waves given as an initial condition, a response of the electromagnetic field to the materials is obtained. These sequences of the calculation have been currently performed by a computing machinery. Since resolution of the space is dependent on the grid size, calculation errors caused by an artificial boundary condition on the grid are reduced by using the small grid. On the other hand, the number of the grid simply affects the computation time. Therefore, the size and the number of the grid have to be optimized according to performance of the computing machinery. A required relation between the time step and the grid size for the stable calculation is provided by Courant condition.[13]

I show an example of FDTD calculation for solving resonant wavelength and electromagnetic field of localized SPPs for a metallic nanostructure. Figure 2.5(a) shows 3D FDTD analysis of a scattering spectrum from an Au nanoparticle with the diameter of 50 nm set in vacuum. The grid size was set to $1 \times 1 \times 1$ nm$^3$, the time step was 10 fs, and polarized white light was irradiated as the incident light. As shown in Fig. 2.5(a), a scattering peak was observed around 526 nm and the intensity was rising up toward the range of ultraviolet. The peak is associated with localized SPP resonance of the Au nanoparticle, and the increase of the scattering intensity in the ultraviolet region is caused by plasma reflection due to a plasma oscillation inside the Au nanoparticle. Figure 2.5(b) indicates distribution of the electric field around the Au nanoparticle excited by 526 nm wavelength. The intensity of the electric field distribution is normalized by electric field intensity of the incident light, so that the electric field intensity is equivalent to the field enhancement factor. As you can see, strong fields were localized at the top and bottom of the nanoparticle, in which the vertical axis was parallel to the polarization direction of the incident light. The field distribution is based on the Fröhlich mode, and it is clear that size of the localized field along the horizontal axis roughly corresponds to a diameter of the nanoparticle. Note that distribution of the field enhancement on the boundary of the nanoparticle is not smooth but it shows several shots. This is due to artificial sharp corners around the nanoparticle produced by square grids adjacent to the spherical boundary, where electromagnetic fields are extremely concentrated at the corners. Although the area of the error can be reduced using a small grid, the error is not completely removed. Therefore, evaluation of the field enhancement should be considered by an average of a few points around the maximum value. Given the maximum field enhancement is about 10, the Raman enhancement factor adjacent to the nanoparticle is estimated to ~ $10^4$ according to Eq. (2.16).

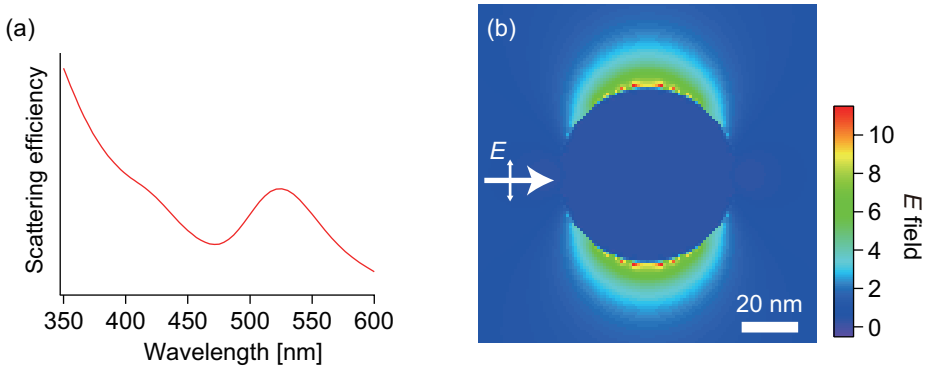


**Figure 2.5** FDTD analysis of (a) scattering spectrum of an Au nanoparticle with the diameter of 50 nm, and (b) electric field distribution around the Au nanoparticle excited at 526 nm wavelength.

For the experimental measurement of resonance condition of localized SPPs of a metallic nanostructure, absorption and scattering spectroscopy have been utilized. When white light is illuminated to a metallic nanostructure, an electromagnetic field of the white light excites localized SPPs on it. The energy of the excited localized SPPs is released through ohmic losses and radiative losses. Hence, the absorption spectrum reflects on an energy decay caused by the thermal relaxation, and the scattering spectrum indicates a radiative light coupling to the localized SPPs. Since wavelength components of the scattering light is overlapped with that of the excitation light, the scattering light is usually measured by dark-field optical microscopy.[3] The spectroscopic observation is quite useful for not only a nanosphere, but also the various shapes of metallic nanostructures.[3-5] Recently, nano-scale mapping of energy distribution of localized SPPs on metallic nanostructures has been carried out by the usage of electron energy-loss spectroscopy (EELS),[14] and near-field optical microscopy.[15,16] As for experimental measurement of the enhancement factor, SERS spectroscopy from molecules adjacent to metallic nanostructures is useful. Raman enhancement factor is estimated by comparing intensity of spontaneous Raman scattering and that of SERS from molecules, then the electric field enhancement factor can be obtained from the forth root of the Raman enhancement factor according to Eq. (2.16).

## 2.2
## Tip-enhanced Raman scattering

The enhanced field associated with localized SPPs of a metallic nanoparticle is confined to surface of the metallic nanoparticle as I explained in previous section. Herein, scanning a metallic nanoparticle on a sample surface with observing SERS from the sample, we can observe the SERS at an interval of the nanoparticle size beyond the diffraction limit of light. How can we manipulate a metallic nanoparticle on a material at the nano-scale accuracy? The good candidate for the purpose is a metallic sharp tip installed in scanning probe microscopy, because the tip apex can be employed as a metallic nanoparticle and precisely controlled in 3-dimention at the nano-scale resolution. Raman spectroscopy based upon localized SPPs excited at a metallic tip apex is “tip-enhanced Raman scattering (TERS) spectroscopy”.[17]

A fundamental concept of TERS spectroscopy is explained. When a metallic tip apex with a nanometric diameter is irradiated with an optical field, localized SPPs are excited at the tip apex as well as the case of a metallic nanoparticle. The localized SPPs generate a localized electric field,

resulting in photon energy confined in the local vicinity of the tip apex. The field distribution confined at a metallic tip apex can be easily understood using the FDTD calculation. Figure 2.6(a) indicates the calculated field distribution for a silicon tip coated with Au having the apex diameter of 30 nm. The tip was put in air above a glass substrate with a distance of 2 nm. The excitation laser wavelength was 777 nm that was chosen according to the plasmon resonance wavelength at the tip apex, and the laser was irradiated from the left side with the vertical polarization. This calculation was done in 3D, and the mesh size was set to 1 × 1 × 1 $nm^3$. As you can see, the electric field is strongly enhanced and localized into a tiny volume around the tip apex. Figure 2.6(b) represents a line profile of the enhanced electric field along the horizontal axis between the tip and the glass substrate. Although the center of the line profile has four small spikes caused by the calculation error, the field distribution is well confined under the tip apex. Executing Gaussian fitting on the line profile, the FWHM is estimated to be ~ 30 nm, corresponding to the tip apex size. The localized light is interacted with a sample under the tip apex, which gives SERS from the sample. The SERS is again interacted with the tip apex, and propagated to the far-field. The propagated signals are finally detected by spectroscope. Since localized SPPs excited at a metallic tip apex work as a nano light source, we can obtain high-resolution Raman images by scanning the tip on a sample.

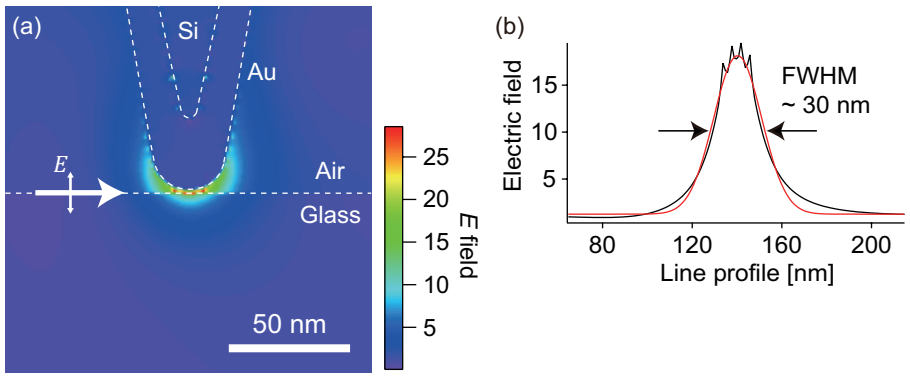


**Figure 2.6** (a) Calculated local field distribution for an Au-coated Si tip with the apex diameter of 30 nm, put in air above a glass substrate with the distance of 2 nm. The intensity represents the electric field enhancement. The excitation laser wavelength is 777 nm, and the laser is irradiated from the left side with the vertical polarization (white arrow). The white dotted lines are interfaces between different materials. (b) Line profile of the enhanced electric field along the horizontal axis between the tip and the grass substrate in Fig. 2.6(a). The black line shows the low data, and the red line shows the Gaussian-fitted data.

Optical system of TERS spectroscopy/microscopy is based on Raman microscopy and AFM. Figure 2.7 represents the optical configuration of TERS spectroscopy/microscopy that I use. First of all, the laser beam is collimated with a beam expander, and polarization of the laser is properly adjusted by a half wave plate, a polarizer, and a z-polarizer, where the polarization is formed into radial polarization. Then, it is introduced into an inverted objective lens through a mask that rejects the low NA components (NA < 1). A surface of the substrate is focused by the evanescent light with the objective lens with the high NA equal to 1.4 (Nikon, Plan Apo). A metallic tip is approached and moved at the focused position, where a distance between the tip and the substrate is precisely controlled by feedback system using a quadrant detector. After the tip adjustment, a sample is displaced to the focused area. The tip and sample are independently controlled by the PZT. Raman scattering light from the sample is collected by the same objective lens, and lead to a spectrometer through an edge filter suitable for the excitation laser and a slit with the width of 100 μm. The Raman scattering is dispersed by a grating, and focused on a liquid nitrogen cooled CCD camera (Roper, 1340 × 400 channel, -100 Cº). The grating has blaze wavelength of 600 and 1200 lines/mm that is chosen according to the necessary spectral resolution. Raman scattering from the sample is detected point by point with raster scanning of the sample stage, fixing the position of the tip at the focus spot under a contact-mode AFM.

This system is designed to ensure the reproducibility and stability. A mirror (M*) inserted before the edge filter is installed for adjusting the tip position at the center of the focus spot, in which total reflection light from the substrate surface is detected during raster scanning of the tip around the focus spot. The intensity of the total reflection light is slightly decreased when the tip is at the focus spot because a part of the evanescent light formed on the substrate surface is scattered by the tip apex. By analyzing the intensity change of the reflection light, a scattering image from the tip is constructed. The tip apex is adjusted to the center of the focus spot by the PZT at the nanometric accuracy. Figure 2.8 shows a SEM image of an Ag-coated silicon tip with the thickness of 65 nm, prepared by a vacuum vapor deposition method. The vacuum vapor deposition method usually makes a rough surface on a silicon tip as shown in Fig. 2.8. One can see a nanoparticle at the tip apex whose diameter is ~ 50 nm, where the nanoparticle is arguably Ag. Whether a metallic nanoparticle is attached on the tip apex or not is one of the most important points to get strong TERS signals from samples. Therefore, it's deemed desirable to check SEM images of metal-coated tips although an ultratrace amount of chemicals could attach to the tips during the SEM observation. Also, to avoid a friction damage at a metallic tip apex during the scanning process, silicon tips having a small elastic coefficient like ~ 0.01– 0.1 N/m are usually utilized.

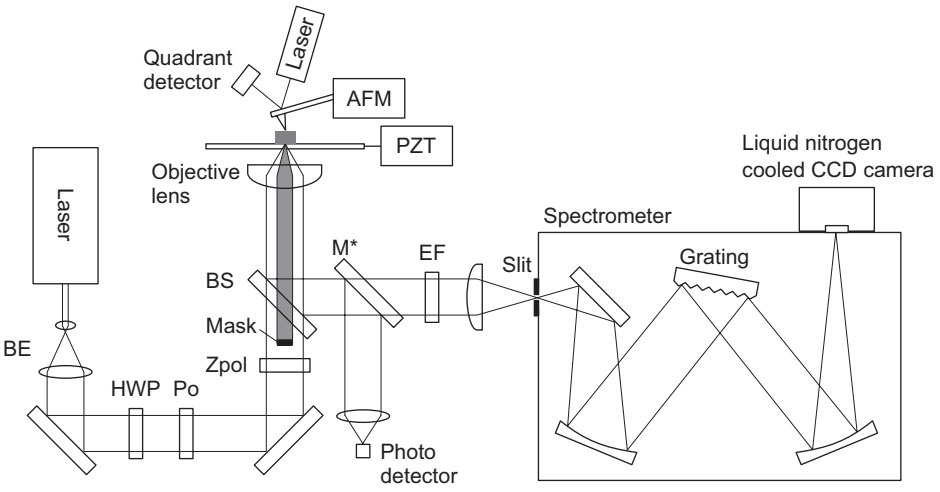


**Figure 2.7** Optical configuration of TERS microscopy. BE is a beam expander, HWP is a half wave plate, Po is a polarizer, Zpol is a z-polarizer, BS is a beam splitter, and EF is an edge filter. M* is a flick mirror which is installed for the photo detector and removed for the spectroscope.

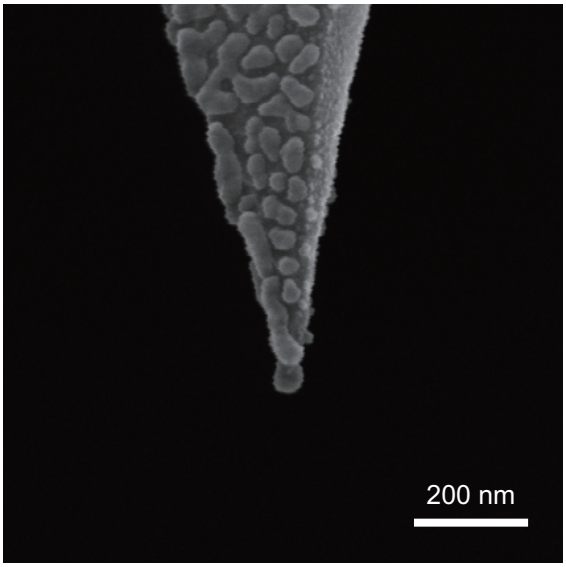


**Figure 2.8** SEM image of an Ag-coated silicon tip with the thickness of 65 nm.

Since TERS counts on the intensity and size of localized SPPs excited at a metallic tip apex, the key point is the efficient excitation of the localized surface plasmons. For this purpose, many efforts have been focused on the optimization. Here, I introduce several kinds of researches for it.

**Optimization of polarization components in the incident light field**

Confinement of a light field at a metallic tip apex is strongly induced when electrons in the tip are oscillated parallel to the tip axis due to lightning rod effect.[18] Therefore, polarization of the incident light should be adjusted to have as much vertical components as possible onto a surface of the substrate. Using an objective lens for focusing incident light, radially polarized light can dominantly create the vertical polarization components at the focus spot. [19-21] The radially polarized light is generated with a z-polarizer that is composed of several half-wave plates. In addition, annular illumination cutting the low NA components (NA < 1) with a mask is commonly utilized for TERS spectroscopy combined with an inverted optical microscope.[22] The low NA components (NA < 1) are transparent light and can be scattered by elsewhere than a tip apex, thus they can give a background noise. On the other hand, the high NA components (NA > 1) are totally reflected on a surface of the substrate. As a result, the annular illumination can reduce the background noise. Figure 2.9 represents spatial distribution of scattering light from a metallic tip apex on a glass substrate, illuminated by focused laser light using an objective lens (NA = 1.4) with a mask under (a) radial polarization and (b) linear polarization. Since a metallic tip strongly scatters vertically polarized light onto the substrate due to the lightning rod effect, Fig. 2.9 shows field distribution of the vertical polarization components produced onto the surface of the substrate observed from the underneath. The yellow spot indicates a position causing a strong interaction between incident light and the metallic tip, which is efficient excitation of the localized SPPs. As you can see, radial polarization light gives a single spot while linear polarization light gives two spots at the center of their images. The reason why linear polarization light gives the two spots is that the linear polarization light is interfered with the components having a phase shift of $\pi$ at the focus spot, resulting in a creation of the two spots having the vertically polarized components along the linear polarization direction. These scattering images indicate that radial polarization light effectively produces *z* polarization components than linear polarization light does.

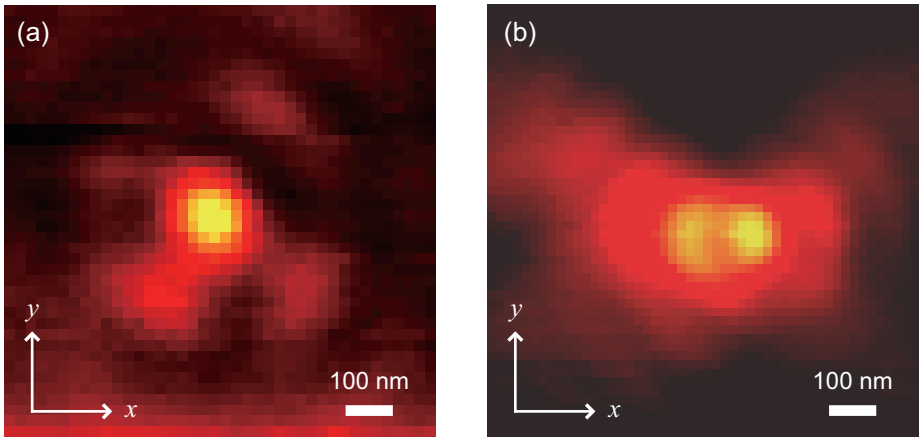


**Figure 2.9** Field distribution of scattering light interacted with a metallic tip apex, illuminated by focused laser light using objective lens (NA = 1.4) with a mask under (a) radial polarization and (b) linear polarization along the horizontal *x* axis.

### Optimization of geometry and material for metallic tips

Geometry and material of metallic tips are quite important to obtain enormous field enhancement at the tip apex because plasmonic behavior of metallic nanostructures sensitively depends on them. In general, Au or Ag tips are utilized for TERS experiment because the localized surface plasmon resonance wavelength of their tips is located in a visible range. Several methods for preparing metallic tips have been proposed, for instance, a metallic tip could be coated with a thin metal film on a silicon cantilever,[23] a metallic nanoparticle could be attached to the end of the tip,[24] or a metal wire could be electrochemically etched after milling with a focus ion beam.[25] Also, as a method for tuning the localized surface plasmon resonance at a metallic tip apex, several materials such as $SiO_2$, $AlF_3$, $SiO_x$, W for a base cantilever have been proposed.[26-30] The plasmon resonance wavelength is greatly altered according to a refractive index of the materials, which can be interpreted from Eq. (2.12). For example, since a refractive index of Si and $SiO_2$ is ~ 1.5 and ~ 4.3 at the wavelength of 488 nm, the plasmon resonance wavelength of a Ag-coated silicon tip is dramatically blue shifted with a replacement from Si to $SiO_2$.[28] Numerical analysis is accessible to roughly estimate the plasmon resonance wavelengths for various kinds of tips.[31-33] In addition, material coating on metallic tips has been suggested for improving the stability of plasmonic structures of the tip.[34] The tip geometry giving the strong field enhancement constantly has not been well-established, hence there still remains room for the optimization of the tip geometry.[35-37]

## 2.3
## Chemical enhancement in SERS

SERS from a molecule adsorbed on a metal surface is enhanced through not only the field enhancement effect but also the chemical effect.[38,39] The chemical effect can enhance Raman scattering efficiency of molecules in addition to the field enhancement effect. In this section, I explain the basic mechanism of chemical effect in SERS. After the explanation, I propose some methods for distinguishing electromagnetic effect and chemical effect in SERS. I suggest some ideas for selectively inducing SERS through the electromagnetic effect or through the chemical effect. Then, I show you wavelength dependence of SERS spectra from a sample. Moreover, I also mention to chemically-enhanced Raman modes from a sample sandwiched between metal nanostructures. I will explain the fundamental physics behind the ideas and elucidate the results in detail.

### 2.3.1
### Mechanism of chemical enhancement in SERS

Chemical enhancement in SERS involves changes to the adsorbate electronic states due to an interaction of the analyte with a metal. When molecules are adjacent to metal atoms in the order of Å scale, electronic orbital of the molecules can interact with that of the metal atoms. The interaction creates complex vibronic states in the molecule-metal system involving electronic states of the molecules and Fermi level of the metal atoms. Here, I consider such a molecule-metal system as follows. Fermi level of the metal lies between the highest occupied molecular orbital (HOMO) level and the lowest unoccupied molecular orbital (LUMO) level of the molecule. Figure 2.10 depicts an energy level scheme for the molecule-metal system. The continuous metal levels of the conduction band of the metal are shown in the left, and the discrete molecular electronic levels are in the right. According to Born-Oppenheimer approximation, I describe electron motion and atomic motion in the system independently, and indicate the discrete molecular electronic levels by $|K]$ for the LUMO state and $|I]$ for the HOMO state, and group of the molecular vibration modes by $\sum|v\rangle$. $\hbar\omega_{MK}$ is an energy bandgap representing the charge-transfer from the metal to the molecule, and $H_{IM}$ is a coupling matrix element that means the degree to which a particular vibration can mix the Fermi level state $|M]$ with the HOMO state $|I]$. When Raman scattering of the molecule is excited by a photon that has the energy $\hbar\omega$ corresponding to $\hbar\omega_{KM}$, charge-transfer transition from the metal to the

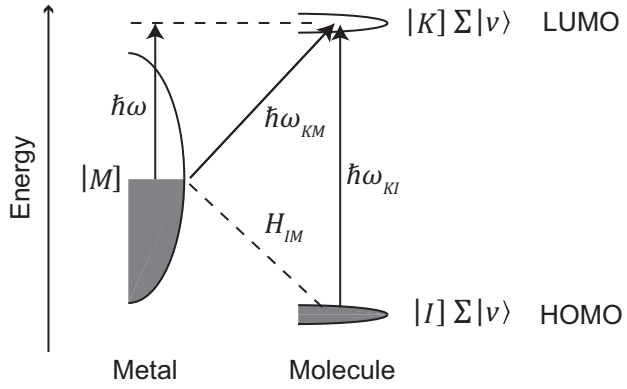


**Figure 2.10** Energy level scheme for a molecule-metal system for metal-to-molecule charge-transfer transitions.

molecule is stimulated by the incident photon. The Raman scattering process can be described by the quantum theory. When I utilize an initial state $|I]|m\rangle$, a final state $|I]|n\rangle$, and a virtual vibronic state $|K]|e\rangle$ of molecular vibrational state, the Raman tensor element *C* is depicted as [5]

$$C = -(2/\hbar^2)\sum_{K\neq I}\sum_{M>I}\left[[M|D_\sigma|K][K|D_\rho|I] + [M|D_\rho|K][K|D_\sigma|I]\right] \times \frac{(\omega_{KI}\omega_{KM} + \omega^2)\, h_{IM}\, \langle m|Q|n\rangle}{(\omega_{KI}^2 - \omega^2)(\omega_{KM}^2 - \omega^2)} \tag{2.17}$$

where $\hbar\omega_{XY}$ represents an energy gap between electronic state *X* and state *Y*. Although the equation looks very complicated, the thing is that the Raman tensor element can resonantly diverge under a resonant condition $\omega_{KM} \simeq \omega$. Since this resonance condition is exactly associated with the charge-transfer in this metal-molecule system, chemical effect in SERS needs chemical bonds between the molecule and the metal. Due to the necessity of the chemical bonds, chemical effect in SERS picks up a dominant Raman spectrum of only molecules bonding with metal surface. This is the reason why the chemical effect is often called 'first-layer' enhancement effect.[40] Raman enhancement factor accompanied with the chemical effect has been estimated ~ 10 to $10^7$. [41-43] The wide distribution of the enhancement factor implies that the chemical effect is quite sensitive to the adsorption site of the molecules on metal surfaces. The chemically enhanced modes can be enhanced by the electromagnetic effect, and therefore those Raman modes are expected to be more enhanced than the electromagnetically enhanced Raman modes.

The chemical effect can induce nontotally symmetric vibration modes of molecules because a polarizability of the molecules is altered by the vibronic interaction between the molecules and the metal atoms. Since nontotally symmetric vibration modes are observed by SERS only through the chemical effect, contribution of the chemical effect can be analyzed by monitoring such nontotally symmetric vibration modes. For example, resonance condition of the chemical effect was well comprehended by Osawa et al.[44] He monitored an intensity change of SERS at a nontotally symmetric vibration mode of 4-aminothiophenol (4-ATP) molecules attached on an Ag electrode with tuning Fermi level of the Ag electrode under an electrochemical environment. In the electrochemical environment, the energy gap between Fermi level of the Ag and LUMO state of the 4-ATP molecules is adjustable by changing the applied potential to the Ag electrode with a reference electrode. Figure 2.11 is potential dependence of 1440 $cm^{-1}$ band Raman intensity of the 4-ATP molecules for (a) 632.8 nm, (b) 514.5 nm, and (c) 488.0 nm excitations. The Raman band at the 1440 $cm^{-1}$ is associated with the nontotally symmetric vibration mode. As shown in Fig. 2.11, the Raman intensity is resonantly increased at a certain potential. It is confirmed that the resonance condition is dependent on the excitation wavelength, which proves the charge-transfer mechanism of the chemical effect in SERS. Hence, charge-transfer mechanism in SERS can be understood by monitoring behavior of nontotally symmetric vibration modes in molecules.

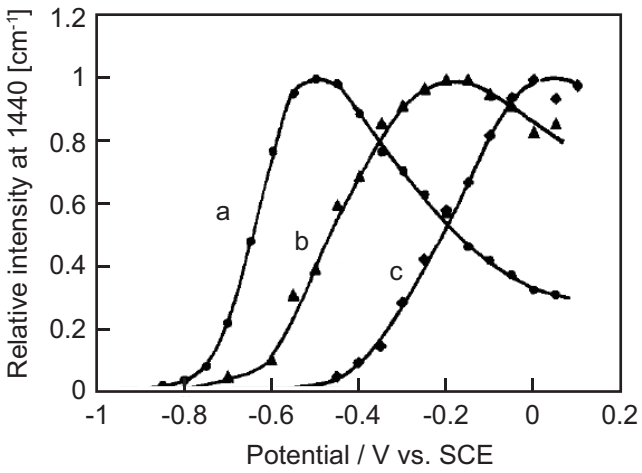


**Figure 2.11** Potential dependence of the 1440 $cm^{-1}$ band Raman intensity of 4-aminothiophenol molecules for (a) 632.8 nm, (b) 514.5 nm, and (c) 488.0 nm excitations. The intensities are normalized with the maximum values for each excitation (referred from ref. 44, Fig. 4).

### 2.3.2
### Selective enhancement through electromagnetic effect

For evaluating electric fields generated on a metallic nanostructure from the SERS measurement, electromagnetic effect and chemical effect in the SERS have to be distinguished. In this section, I suggest a method to selectively induce electromagnetic effect in SERS. As explained in section 2.1, field enhancement due to localized SPPs on a metallic surface extends to several tens of nanometer over a metal surface, while chemical effect in SERS occurs in a few angstrom regions adjacent to the metal surface. Therefore, molecules kept above a metal surface by a few nanometer can be sensitive only to the electromagnetic effect. For the purpose of selectively inducing the electromagnetic effect, I introduced a nanometric-thin spacer layer between a metal surface and sample molecules to prevent the molecules from the direct attachment to the metal surface.

I first prepared an Au film with the thickness of 8 nm which was produced on a glass substrate by a vacuum vapor deposition method under $2.0 \times 10^{-7}$ Torr. In order to form a spacer layer on the Au film, I immersed the Au film into a 1 % ethanol solution of polyvinylpyridine (PVP) for 8 hours. The average thickness of the spacer layer could be controlled by the solution concentration and immersion time, and could be measured by ellipsometry. In the present case, the average spacer thickness was around 4 nm. Also, I found through the AFM imaging that the PVP layer contained some holes, however, with reasonably low density. The average distance between such holes was several micrometers; hence, it was always possible to select a surface area avoiding the holes. After the deposition, I removed the excess PVP molecules deposited on the Au film from the surface by washing the Au film with pure ethanol. As a probe of the electromagnetic effect on the Au film, I utilized 4-aminothiophenol (4-ATP) molecules. I prepared a 1 mM ethanol solution of 4-ATP molecules, and immersed the PVP-coated Au film into the 4-ATP solution for 12 hours. Finally, I took it out from the solution, and dried it. To verify the effect of the spacer layer, I also prepared an Au film on which 4-ATP molecules were adsorbed without a PVP spacer layer. It is well known that 4-ATP molecules form a densely packed, well-ordered self-assembled monolayer (SAM) on Au surfaces, therefore 4-ATP molecules could be easily adsorbed onto Au surface without a spacer layer.

Figure 2.12(a) is schematic illustrations of a PVP-coated Au film covered with 4-ATP molecules and a non-coated one. Raman measurement of the samples were performed using optical system shown in Fig. 1.3, where the excitation light was illuminated from the glass side of the samples. Figure 2.12(b) shows SERS spectra of 4-ATP molecules on the Au films with and without the PVP spacer layer, and a normal Raman spectrum of 4-ATP bulk molecules. The three spectra were

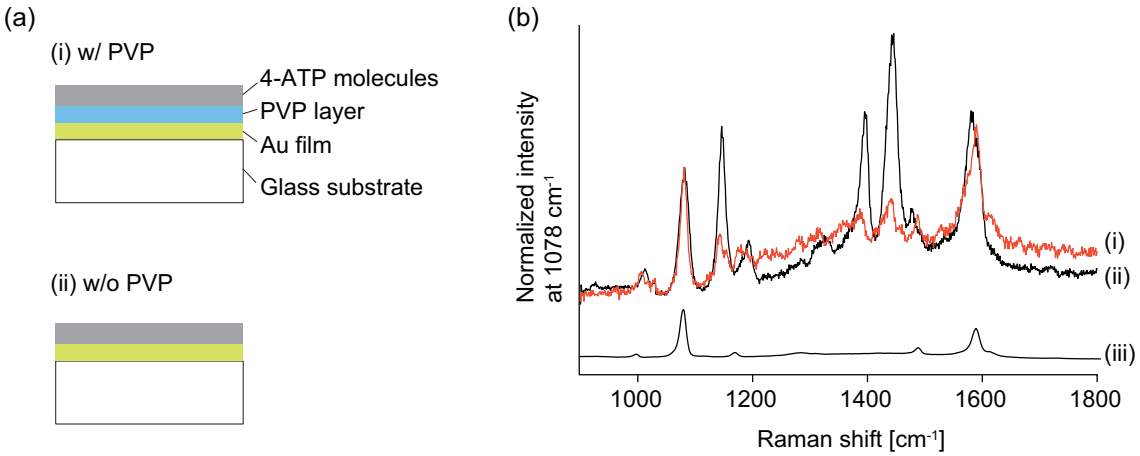


**Figure 2.12** (a) Schematic illustrations of (i) PVP-coated Au film covered with 4-ATP molecules, and (ii) non-coated one. (b) SERS spectra of 4-ATP molecules (i) with and (ii) without a PVP spacer, respectively. The spectra are normalized at 1078 $cm^{-1}$ for the facile comparison. (iii) Normal Raman spectrum of 4-ATP molecules. The excitation laser is 632.8 nm.

**Table 2.1** Peak frequencies and assignments for 4-ATP solid and 4-ATP SAMs on Au films.

| 4-ATP solid | 4-ATP on Au | Assignments [a] |
|---|---|---|
| 1585 | 1581 | $\nu$ CC, 8*a* ($a_1$) |
| | 1571 | $\nu$ CC, 8*a* ($b_2$) |
| 1484 | 1483 | $\nu$ CC + $\delta$ CH, 19*a* ($a_1$) |
| | 1438 | $\nu$ CC + $\delta$ CH, 19*b* ($b_2$) |
| | 1390 | $\delta$ CH + $\nu$ CC, 3 ($b_2$) |
| | 1327 | $\nu$ CC + $\delta$ CH, 14 ($b_2$) |
| 1168 | 1177 | $\delta$ CH, 9*a* ($a_1$) |
| | 1141 | $\delta$ CH, 9*b* ($b_2$) |
| 1080 | 1078 | $\nu$ CS, 7*a* ($a_1$) |

[a] Approximate description of the Raman modes ($\nu$: stretch, and $\delta$: bend) from ref. 44, 45, and 46. Frequencies ($cm^{-1}$) are followed by the Raman spectra in Fig. 2.11.

measured with 632.8 nm excitation wavelength. In order to compensate the slight difference in the enhancement, the two SERS spectra are normalized at 1078 $cm^{-1}$. The bottom spectrum is a normal Raman spectrum of 4-ATP bulk molecules. Comparing the two Raman spectra with and without introduction of the PVP spacer layer, the peaks at 1078 and 1581 $cm^{-1}$ remain unchanged, while the peaks at 1141, 1390, 1438 and 1571 $cm^{-1}$ are drastically decreased with the PVP layer. This result indicates that the peaks strongly observed with the PVP layer can be attributed to the electromagnetic effect in SERS, while the decreased peaks can be due to the chemical effect. Note that PVP molecules don't have any observable Raman modes in the spectral region of 1000 – 1600 $cm^{-1}$.

To understand the reason why the enhancement depends on the vibrational modes, I refer to the peak assignments for 4-ATP molecules as shown in Table 2.1. The band assignment of 4-ATP molecules is based on vibrations characteristic of *p*-disubstituted benzenes given by notations of the corresponding vibrations of benzenes, and the symmetric group is characterized as $C_{2v}$ symmetry.[47] The benzene ring vibrations are classified as $a_1$, $a_2$, $b_1$, and $b_2$ species. With respect to the molecular plane, the $a_1$ and $b_2$ species are in-plane vibration modes, and $a_2$ and $b_1$ modes are out-of-plane vibration modes. Note that $a_1$ vibrations are polarized along the molecular $C_2$ axis and totally symmetry modes, whereas $b_1$ and $b_2$ vibrations are polarized perpendicular to the $C_2$ axis and non-totally symmetry modes. Although all of the vibrations are Raman active, the normal Raman spectrum is dominated by the $a_1$ vibrations due to the totally symmetric vibrations as shown in Table 2.1.[48] Here, you can notice that the active peaks at 1078 and 1581 $cm^{-1}$ with the PVP layer are based on the $a_1$ vibrations. Since the electromagnetic effect in SERS simply enhances light fields over the samples, vibration modes observed in the normal Raman spectrum are purely enhanced. In contrast, the deactivated peaks at 1141, 1390, 1438 and 1571 $cm^{-1}$ with the PVP layer are associated with the $b_2$ vibrations. Since 4-ATP molecules form the SAM on the Au film without the PVP layer, it is clear that their activation of the $b_2$ vibrations needs chemical bonds between the metal and the molecule. That is, it is confirmed that the enhancement of the $b_2$ vibrations is associated with chemical effect in SERS. This nature of the $b_2$ vibrations has been already pointed out in previous researches devoted to understand the mechanism of the SERS by the Raman intensity dependence on excitation wavelength,[44] pH,[44,49] potential on electrodes,[49] metal geometry,[50-52] and direction of charge transfer,[53,54] although there are some reports that claim the $b_2$ vibrations of 4-ATP molecules can be caused by molecular transformation from 4-ATP to 4,4'-dimercaptoazobenzene.[54,55] One can notice that the $b_2$ vibrations are still observed in the black spectrum, albeit with weak intensities. This is because, even though the prominent mechanism for the enhancement for these modes is the chemical effect, they also have slight contribution through the electromagnetic effect.

### 2.3.3
### Selective enhancement through chemical effect

The introduction of a nanometric spacer layer between a metal and a sample provided a practical way to distinguish the SERS vibrational modes that are dominantly enhanced by either electromagnetic or chemical mechanism. Another evidence of the chemical effect can be found by an introduction of halide ions into sample molecules. It is believed that halide ions clean metal surfaces by removing residual compounds and make "active sites" on the metal surfaces, which increases the number of chemical bondings between the metal atoms and the sample molecules.[56-58] I argue that the additional enhancement with the introduction of halide ions is due to the enhancement through the chemical effect.

I prepared a mixed ethanol solution of 1 mM 4-aminothiophenol molecules and 1 mM sodium bromide (NaBr). In the solution, NaBr is ionized into $Na^+$ and $Br^-$, and $Br^-$ works as halide ions. I immersed an Au-coated substrate into the mixed solution for 12 hours, and rinsed it with pure ethanol, where a 4-ATP SAM was formed on the surface of the Au-coated substrate. Figure 2.13(a) shows SERS spectra of the 4-ATP molecules on Au-coated substrates prepared with and without $Br^-$ ion, respectively. The excitation wavelength was 632.8 nm. It is observed that intensities of the all $b_2$ vibrations at 1141, 1390, 1438 and 1571 $cm^{-1}$ increase with the introduction of NaBr solution, while intensities of the $a_1$ vibrations remain immutable. Since only the $b_2$ vibrations are selectively enhanced, the enhancement induced by the halide ions is associated with the chemical effect. Here, I contemplate the reason why halide ions selectively cause the chemical effect in SERS. From the aspect that electron affinity of 4-ATP molecules is 2.58 eV and that of $Br^-$ ion is 2.96 eV, $Br^-$ ions are more strongly adsorbed on Au atoms than 4-ATP molecules. $Br^-$ ions skin Au atoms from the Au substrate surface, and then AuBr is formed into a dimer combination in ethanol solution. The reaction process creates active sites on which 4-ATP molecules can attach to the flesh Au surface, inducing the increase of the number of 4-ATP molecules adsorbed on the Au surface. Indeed, selective Raman enhancement through the chemical effect by halide ions has been often explained in terms of the increase of the number of the adsorbed molecules,[57-59] but the selective enhancement is not simply explained by the reason. This is because if the enhancement is due to the increase of the adsorbed molecules, the electromagnetic effect must be enhanced as well as the chemical effect. In my opinion, the selective enhancement is due to an increase of the packing density of the 4-ATP molecules on the Au surface. There are several articles claiming that the $b_2$ vibrations stem from a chemical transformation from 4-ATP to 4,4'-dimercaptoazobenzene, in which the two 4-ATP molecules

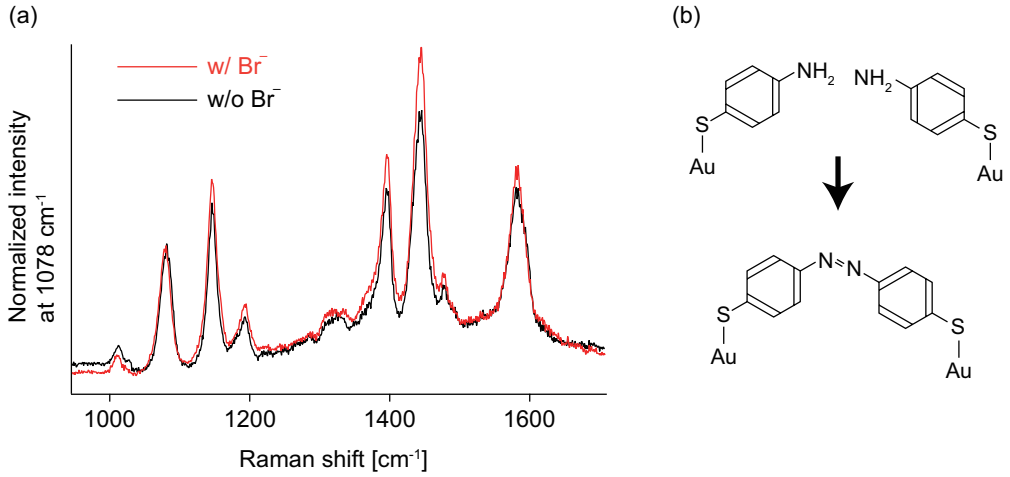


**Figure 2.13** (a) SERS spectra of 4-ATP molecules prepared (red) with and (black) without $Br^-$ ion, respectively. The excitation wavelength is 632.8 nm. (b) Schematic image of chemical transformation from 4-ATP to 4,4'-dimercaptoazobenzene.

are oxidized by photo irradiation and form a double-bond between the two nitrogen atoms as shown in Fig. 2.13(b).[38,39] In order to undergo this reaction, 4-ATP molecules have to exist each other in subnano-scale proximity (the length of a 4-ATP molecule is ~ 7 Å). Hence, the increase of the packing density of the 4-ATP molecules can facilitate the chemical transformation, resulting in increasing Raman intensities of the $b_2$ vibrations. Actually, the mechanism of chemical effect in SERS is still controversial because the interaction between metal atoms and molecules is occurred at the atomic level, which is not observable in conventional optical microscopy. Toward the detail understanding, we need to utilize nano-resolved spectroscopic techniques such as TERS spectroscopy.

### 2.3.4
### Excitation wavelength dependence on SERS

In this section, I elucidate a resonance condition on the chemical effect in SERS of 4-ATP molecules. As I explained in section 2.3.1, the chemical enhancement is due to charge-transfer between a metal atom and a molecule The resonance condition can be found by monitoring the Raman intensity of $b_2$ vibrations of the 4-ATP molecules under several excitation wavelengths. To elucidate the resonance condition, I measured SERS of a 4-ATP SAM on Au and Ag substrates coated on a cover slip using several excitation wavelengths, where the both metal films had a thickness of 8 nm.

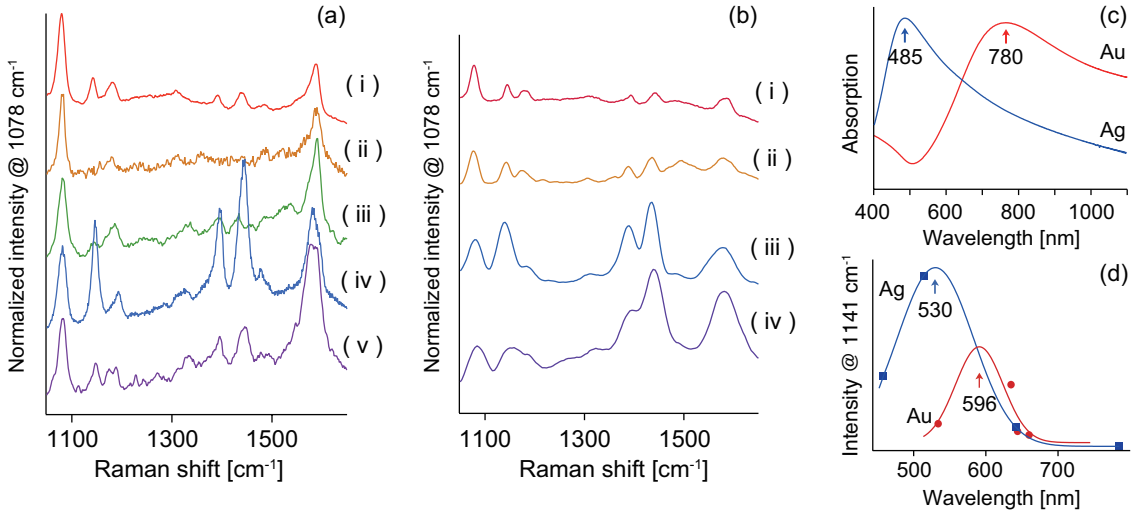


**Figure 2.14** (a) SERS spectra of 4-ATP molecules adsorbed on Au substrate, normalized at 1078 $cm^{-1}$. The excitation wavelengths for the spectra (i) through (v) are 785, 658, 642, 633 and 532 nm, respectively. (b) SERS spectra of 4-ATP adsorbed on Ag substrate, normalized at 1078 $cm^{-1}$. The excitation wavelengths for the spectra (i) through (iv) are 785, 642, 514.5 and 458 nm, respectively. (c) Absorption curves for Au and Ag substrates used in the present study, in which the peak wavelengths represent the surface plasmon resonance. (d) Resonances curves plotted from the intensity of the mode at 1141 $cm^{-1}$ in Fig. 2.14(a) and (b). The blue line is for the Ag substrates, and the red line is for the Au substrates.

Figure 2.14(a) shows a series of SERS spectra measured from 4-ATP molecules on an Au substrate, excited with the indicated wavelengths. These spectra are normalized for the mode at 1078 $cm^{-1}$, so that one can focus attention on the modes that are enhanced through the chemical effect. The increased intensities of the $b_2$ modes in spectrum (iv) indicate the chemical resonance in SERS. Similar results are also obtained for an Ag substrate as shown in Fig. 2.14(b), where the $b_2$ modes drastically increase in spectra (iii) and (iv). In fact, in the case of the Ag substrate, the $b_2$ modes become even stronger than the $a_1$ modes at the resonance. A careful observation of Fig. 2.14(a) reveals that the $b_2$ modes are once again slightly enhanced in spectrum (i). This is because the excitation wavelength in this spectrum is 785 nm, which is close to the surface plasmon resonance of the Au substrate with the thickness of 8 nm, as illustrated in Fig. 2.14(c). Therefore, the electromagnetic effect is greatly enhanced at this wavelength. As mentioned earlier, the enhancement of the $b_2$ modes also has slight contribution from the electromagnetic effect. Thus, after passing through the resonance in chemical effect, the $b_2$ modes are once again slightly enhanced near the surface plasmon resonance. It should be noted that the absorption spectra were measured for bare metal substrates

without 4-ATP molecules. However, it was confirmed that the presence of 4-ATP SAM did not change the absorption curves significantly.

In order to have a comparison between the electromagnetic and chemical resonances in SERS, the resonance curves obtained from the intensity of the mode at 1141 $cm^{-1}$ in Fig. 2.14(a) and (b) are plotted in Fig. 2.14(d). The experimental data shows a reasonably good fitting with Gaussian curves. The fitting indicates that the resonance for the chemical effect in SERS is obtained at around 596 and 530 nm, respectively, for Au and Ag films. As one can notice, the resonance in SERS related to the electromagnetic and chemical effects are distinctly different. Also, as an evident from different resonance peak positions for Au and Ag substrates in Fig. 2.14(c), the potential for charge-transfer for the two metals is not the same. This is caused by the difference of the Fermi levels of the two metals. In fact, the LUMO level $\pi^*$ of 4-ATP is at ~ 3.03 eV and the Fermi level for Au is ~ 5.1 eV below the vacuum level,[60] so that the resonance condition is estimated to ~ 600 nm, which is well corresponding to the experimental result in Fig. 2.14(c). Note that the Fermi level slightly depends on crystal faces of the metal surfaces due to differences in the surface dipole.[61]

### 2.3.5
### Multiple Raman modes of chemical enhancement in sandwiched molecules

In this section, I show some interesting observations of chemically enhanced Raman modes of 4-ATP molecules sandwiched between two metallic nanostructures. Chemical enhancement in SERS involves a chemical interaction between molecules and metal atoms, and if molecules are sandwiched between two metal structures, the chemical interaction becomes more significantly. It might change vibronic states in the molecules and generate extraordinary enhancements of several Raman peaks. For understanding the contribution of the chemical enhancement for molecules sandwiched between two metal structures, I measured SERS spectra of 4-ATP molecules sandwiched between a metallic tip and a metal substrate.

For this experiment, an Au-coated tip was prepared by evaporating Au on a commercially available AFM cantilever tip. The diameter of the tip apex was about 30 nm after the Au evaporation. This Au-coated tip was brought in contact with the 4-ATP samples adsorbed on an Au substrate, and Raman scattering was then excited with 642 nm laser line. A schematic of the sample arrangement is shown in the Fig. 2.15(a). In Fig. 2.15(b), (i) and (ii) represent Raman spectra of the sandwiched 4-ATP molecules and not-sandwiched 4-ATP molecules (that is, a SAM of 4-ATP). The spectrum

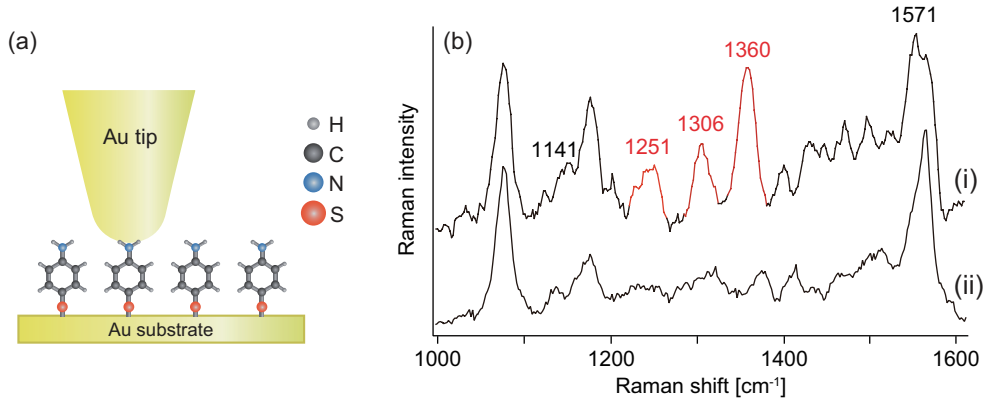


**Figure 2.15** (a) Schematic illustration of 4-ATP molecules sandwiched between Au substrate and Au tip. (b) Raman spectra of (i) the sandwiched 4-ATP molecules and (ii) not-sandwiched 4-ATP molecules. In order to remove the background signal from those 4-ATP molecules which are not under the tip apex, the spectrum here is presented after subtracting SERS signal obtained in the absence of the tip.

(i) was obtained by subtracting the SERS spectrum (ii) from the spectrum obtained under the combination of the Au substrate and the Au-coated tip. The subtraction essentially removes the background signal coming from those 4-ATP molecules that are not under the tip apex, resulting in the subtracted spectrum for only those modes that are enhanced from the molecules under the Au-coated tip.

Comparing the SERS spectrum (i) with (ii), Raman modes at 1141, 1251, 1306, 1360, and 1571 $cm^{-1}$ were selectively enhanced with the contact of an Au-coated tip. The selective enhancement could be interpreted in terms of a metal-molecule-metal charge-transfer theory due to the chemical bonding between Au atoms on the tip and 4-ATP molecules. When an Au-coated tip was brought close to a SAM of 4-ATP prepared on an Au substrate, the Au atoms on the tip made chemical bondings with positively charged nitrogen atoms of the 4-ATP molecules. The chemical bonding between the Au-coated tip and the 4-ATP molecules gave rise to the additional chemical enhancement, due to the increase of the vibronic interaction between the electronic and vibrational motions. According to assignment of vibrational modes in 4-ATP molecules in Table 2.1, 1141 and 1571 $cm^{-1}$ are associated with the $b_2$ modes, whereas the other three modes at 1251, 1306, and 1360 $cm^{-1}$ modes are missing in the assignment list. The latter three extraordinary Raman modes can be caused by a slightly different chemical structure in 4-ATP molecules, compared with 4-ATP molecules on the Au substrate. It is reported that chemical bondings between Au atoms and 4-ATP molecules through the nitrogen atom induce extraordinary Raman modes of 4-ATP molecules.[60,62,63] The ad-

sorption interaction of the molecular bindings changes the electronic properties of the molecules, leading to the increase of the polarizability derivatives of some specific vibrations.[64] The other possible reason could be a local structural deformation of the sample molecules under the tip,[50] because such a tip often applies a small amount of local pressure on the sample. The deformation allows a single or a few 4-ATP molecules to lie flat on the Au film and undergo charge-transfer. Herein, benzene ring π-orbitals better couple to the Au substrate, dramatically increasing vibronic mixing for selected benzene modes. These results imply that nano-scale molecular deformation could be captured with the usage of a nanometric metallic tip.

## 2.4
## Gap-mode enhancement

I have explained enhancement of Raman scattering near a metallic nanostructure in terms of the electromagnetic effect and chemical effect. Since the enhancement is directly linked to the sensitivity in Raman spectroscopy, the way to improve the enhancement has been extensively investigated. The most successful results for dramatically increasing the Raman enhancement effect are attained with a nanometric gap in two metallic nanostructures. When SPPs are induced in two adjacent metallic nanostructures, the electromagnetic fields of the two SPPs are strongly interacted each other. If the distance between the two metallic nanostructures is reduced to a nanometric size, the electromagnetic field is confined to a nanometric volume in the gap. The field confinement provides huge field enhancement in the nano gap. There are some reports that SERS detected from a nanometric junction between metallic nanoparticles shows the Raman enhancement factor from $10^{14}$ to $10^{15}$ order,[65,66] indicating the cross section of the SERS reaches to $10^{-14}$ comparable with that of fluorescence. Owing to the gigantic enhancement factor, the literatures have also mentioned the potential for single molecule detection with SERS spectroscopy, where the single molecule detection was confirmed by SERS intensity following Poisson distribution and sudden spectral change and fluctuation of the Raman modes.[65,66] Based on the idea of field enhancement effect in nano gaps, Raman enhancement in TERS can be greatly improved with an introduction of metallic nano-gap structures. Here, I explain concepts of field enhancement effect at nano gaps between a metallic tip and a metallic substrate using a schematic illustration and numerical analysis.

When a positively charged metal nanostructure approaches to a negatively charged metallic nanostructure, Coulomb interaction between them takes place and it is inversely proportional to

square of the gap distance in the absence of tunneling current. If the two nanostructures are adjacent each other with keeping their electric potential, one can simply guess the electric field at the gap is enormously increased. Now, I consider a system that a metallic tip is adjacent to a metallic substrate as illustrated in Fig. 2.16(a). When light is irradiated to the system with the polarization direction parallel to the tip axis, an electric field of the light couples to localized surface plasmons of the metallic tip and a dipole moment is excited at the tip apex. The dipole moment then generates a local electric field, which induces charge distribution on a surface of the metallic substrate. The charges induced on the surface are opposite to those of the tip apex, resulting in electric field confinement at the nano gap due to the strong Coulomb interaction. It should be noted that the localized SPPs excited in a tip-substrate system must be considered as a single system, because a dipole moment in a metallic tip apex is always interacted with an electric field induced on a surface of the substrate.

To understand an electric field distribution in a tip-substrate system, I calculated electric fields for the system using FDTD method. Figure 2.16(b) is the FDTD result of field enhancement of an Au tip-substrate system, where a diameter of the tip apex is 30 nm, a corner angle of the tip apex is set to 30º, and the gap distance is kept to be 2 nm. The field distribution is plotted under the resonance condition of 609 nm obtained from a scattering spectrum from the tip-substrate gap. As one can see, the field enhancement is dominantly occurred at the gap, and the maximum value displays ~ 36. Comparing the field enhancement at the metallic tip apex with and without the metallic substrate (See in Fig. 2.6(b)), the field enhancement factor with the substrate is ~ 2 times higher than the other. If Raman enhancement factor in the gap is counted, the Raman enhancement factor can be calculated to be $36^4 \approx 1.7 \times 10^7$. Thus Raman scattering detected in a tip-substrate gap is definitely quite sensitive to molecules existing at the gap.

How much is the electric field confined at the nano gap, then? The confined volume can be defined by FWHM of the field distribution at the nano gap. Figure 2.16(c) is a line profile of the enhanced field along the horizontal axis including the gap. The red line is the raw data, and the black dotted line is the Gaussian fitted line. From the dispersion of the Gaussian fitting, FWHM of the enhanced field is estimated to be ~ 15 nm, which corresponds to a half size of the spatial resolution of TERS without a metallic substrate (See Fig. 2.6(b)). In summary, TERS microscopy having a nano gap between a metallic tip and a metallic substrate can dramatically improve both the sensitivity and the spatial resolution.

TERS with a nano gap between a metallic tip and a metallic substrate is often called “gap-mode TERS”, and it has been utilized for improving the sensitivity.[67-72] In fact, the first observation of TERS images was achieved using gap-mode TERS system, where rhodamine 6G and crystal violet

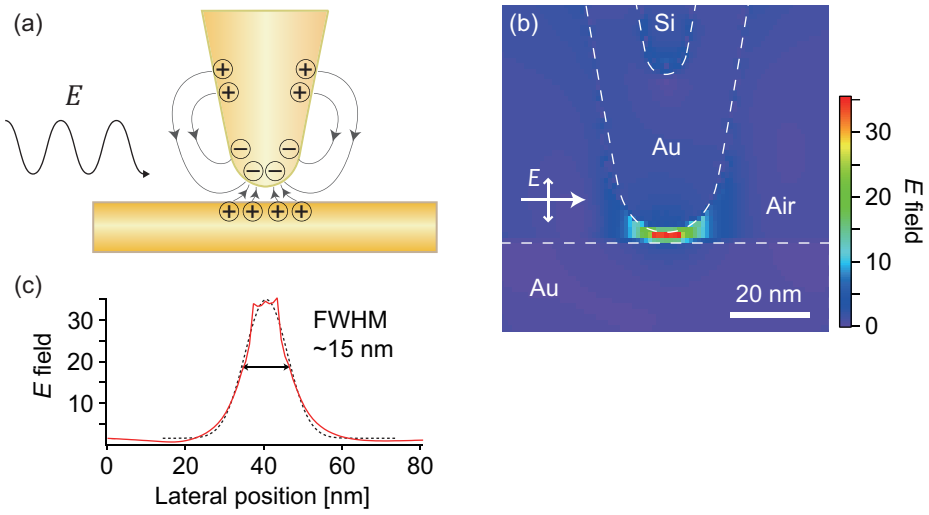


**Figure 2.16** (a) Schematic image of charge distribution condensed at a gap between a metallic tip and a metallic substrate, (b) FDTD result of field enhancement of an Au tip and an Au substrate system excited at 609 nm, diameter of the tip apex is 30 nm, corner angle of the tip apex is 30º, and the gap is adjusted to 2 nm. (c) Line profile of the enhanced field along to the horizontal axis between the tip and the substrate. The red line shows the raw data, and the black dotted line is the Gaussian fitted line. FWHM of the peak is estimated to ~ 15 nm.

molecules randomly deposited on a silver substrate were visualized by using a silver-coated cantilever tip.[68] After the first demonstration of gap-mode TERS microscopy, single molecule detection with the usage of gap-mode TERS has been carried out strenuously.[69-72] For example, Raschke group claimed that Raman enhancement factor at a nano gap between an Au tip and an Au substrate was up to ~ $5 \times 10^9$, where TERS signals of triarylmethane dye malachite green was detected at the single molecular level.[69] In addition, Zenobi group attained single molecule sensitivity of gap-mode TERS using an Ag tip and an Au substrate.[71] Thus gap-mode TERS spectroscopy is one of the promising approaches that enable us to image molecules at the nano scale resolution at the single molecular sensitivity.

## Summary

I have introduced fundamental principles of SERS, which utilizes strongly enhanced electromagnetic fields in the close vicinity of metal nanostructures. I first explained a dispersion relationship of light existing at an interface between a metal and a medium to describe physical properties of surface plasmons on a metal surface. I elucidated excitation condition and enhancement mechanism in surface plasmons using the derived dispersion relationship. I then moved to explain localized surface plasmons in a metal nanoparticle, and the unique plasmonic properties were discussed using FDTD calculation. I then gave a concept of TERS that was based on SERS locally induced at a metallic tip apex. Using FDTD calculation, I showed that a light field was confined at the metallic tip apex with the size comparable to the apex diameter. Optical setup of TERS spectroscopy/microcopy was also described. I also explained chemical effect in SERS, in which the chemical effect was understood by charge-transfer mechanism between a molecule and a metal atom. For distinguishing electromagnetic effect and chemical effect in SERS, I provided a couple of the practical methods. One method was to introduce a thin spacer layer of PVP between a metal substrate and a sample, which prevented any possible chemical bonding between the metal atoms and the sample molecules. Hence, the electromagnetic effect was selectively induced. Another way was to include halide ions in SERS samples, which selectively increased the intensity of those Raman modes that were enhanced through the chemical effect. In addition, I also demonstrated that, apart from the surface plasmon resonance, SERS went through another resonance that was based on the chemical effect, which enabled us to identify the resonance condition of the system due to the charge-transfer. Further, I showed the appearance of some extraordinary enhanced Raman modes when the sample molecules were sandwiched between an Au film and an Au-coated tip. Finally, I introduced gap-mode enhancement of Raman scattering in a nano gap between a metallic tip and a metallic substrate, which indicated much stronger field enhancement at the tip apex comparing to that without the metallic substrate.

## References

1. E. Kretschmann and H. Raether, *Z. Naturfors*, **23 A**, 2135 (1968).
2. T. F. Krauss, *Nature Photon*., **2**, 448-450 (2008).

3. J. J. Mock, M. Barbic, D. R. Smith, D. A. Schultz, and S. Schultz, *J. Chem. Phys*., **116**, 6755-6759 (2002).
4. C. L. Nehl and J. H. Hafner, *J. Mater. Chem.*, **18**, 2415-2419 (2008).
5. G. H. Chan, J. Zhao, G. C. Schatz, and R. P. Van Duyne, *J. Phys. Chem. C*, **112**, 13958-13963 (2008).
6. P. B. Johnson and R. W. Christy, *Phys. Rev. B*, **6**, 4370-4379 (1972).
7. G. Mie, *Ann. Physik IV*, **25**, 377-445 (1908).
8. H. Fröhlich, *Theory of Dielectrics, Oxford University Press*, London (1949).
9. K. S. Yee, *IEEE Trans, Antennas. Propagat*., **14**, 302 (1966).
10. E. M. Purcell and C. R. Pennypacker, *Astrophys, J*., **186**, 705 (1973).
11. B. T. Draine and J. Goodman, *Astrophys, J*., **405**, 685 (1993).
12. C. A. Brebbia and L. C. Wrobel, *Computer methods in fluids*., London, Pentech Press, 26-48 (1980).
13. A. Taflove and M. E. Brodwin, *IEEE Trans. Microwave Theory Tech.*, **MTT-23**, 623-630 (1975).
14. J. Nelayah, M. Kociak, O. Stéphan, F. J. G. de Abajo, M. Tencé, L. Henrard, D. Taverna, I. Pastoriza-Santos, L. M. Liz-Marzán, and C. Colliex, *Nature Phys*., **3**, 348-353 (2007).
15. M. Rang, A. C. Jones, F. Zhou, Z. Li, B. J. V. Wiley, Y. Xia, and M. B. Raschke, *Nano Lett*., **8**, 3357-3363 (2008).
16. K. Imura, T. Nagahara, and H. Okamoto, *J. Chem. Phys*., **122**, 154701 (2005).
17. S. Kawata and V. M. Shalaev, *Tip Enhancement*, Elsevier (2007).
18. L. Novotny, R. X. Bian, and X. S. Xie, *Phys. Rev. Lett.*, **79**, 645-648 (1997).
19. Y. Saito, M. Kobayashi, D. Hiraga, K. Fujita, S. Kawano, N. I. Smith, Y. Inouye, and S. Kawata, *J. Raman Spectrosc*., **39**, 1643-1648 (2008).
20. N. Hayazawa, Y. Saito, and S. Kawata, *Appl. Phys. Lett.,* **85**, 6239-6241 (2004).
21. N. Anderson, A. Bouhelier, and L. Novotny, *J. Opt. A: Pure Appl. Opt*., **8**, S227-S233 (2006).
22. N. Hayazawa, Y. Inouye, and S. Kawata, *J. Microsc*., **194**, 472-476 (1999).
23. N. Hayazawa, Y. Inouye, Z. Sekkat, and S. Kawata, *Chem. Phys. Lett*., **335**, 369-374 (2001).
24. T. Kalkbrenner, M. Ramstein, J. Mlynek, and V. Sandoghdar, *J. Microsc*., **202**, 72 (2001).
25. A. Hartschuh, E. J. Sánchez, X. S. Xie, and L. Novotny, *Phys. Rev. Lett*., **90**, 095503 (2003).
26. C. C. Neacsu, G. A. Steudle, and M. B. Raschke, *Appl. Phys. B*, **80**, 295-300 (2005).
27. D. Mehtani, N. Lee, R. D. Hartschuh, A. Kisliuk, M. D. Foster, A. P. Sokolov, F. Cajko, and I Tsukerman, *J. Opt. A*, **8**, S183-S190 (2006).

28. A. Taguchi, N. Hayazawa, Y. Saito, H. Ishitobi, A. Tarun, and S. Kawata, *Opt. Express*, **17**, 6509-6518 (2009).
29. B. Yeo, T. Schmid, W. Zhang, and R. Zenobi, *Anal. Bioanal. Chem.*, **387**, 2655-2662 (2007).
30. X. Cui, W. Zhang, B. Yeo, R. Zenobi, C. Hafner, and D. Erni, *Opt. Express*, **15**, 8309-8316 (2007).
31. I. Notinger and A. Elfick, *J. Phys. Chem. B*, **109**, 15699-15706 (2005).
32. J. T. Krug II, E. J. Sánchez, and X. S. Xie, *J. Chem. Phys*., **116**, 10895-10901 (2002).
33. F. Festy, A. Demming, and D. Richards, *Ultramicroscopy*, **100**, 437-441 (2004).
34. C. A. Barrios, A. V. Malkovskiy, A. M. Kisliuk, A. P. Sokolov, and M. D. Foster, *J. Phys. Chem. C*, **113**, 8158-8161 (2009).
35. Y. Saito, T. Murakami, Y. Inouye, and S. Kawata, *Chem. Lett.*, **34**, 920-921 (2005).
36. Y. Zou, P. Steinvurzel, T. Yang, and K. B. Crozier, *Appl. Phys. Lett*., **94**, 171107 (2009).
37. M. Fleischer, A. Weber-Bargioni, M. V. P. Altoe, A. M. Schwartzberg, P. J. Schuck, S. Cabrini, and D. P. Kern, *Nano Lett*., **5**, 2570-2579 (2011).
38. D. L. Jeanmaire and R. P. Van Duyne, *J. Electroanal. Chem*., **84**, 1-20 (1977).
39. M. G. Albrecht and J. A. Creighton, *J. Am. Chem. Soc.*, **99**, 5215 (1977).
40. A. Otto, I. Mrozek, H, Grabhorn, and W. Akemann, *J. Phys.: Condens. Matter*, **4**, 1143-1212 (1992).
41. M. Moskovits, *Rev. Mod. Phys*., **57**, 783 (1985).
42. X. Hu, T. Wang, L. Wang, and S. Dong, *J. Phys. Chem. C*, **111**, 6962-6969 (2007).
43. D. P. Fromm, A. Sundaramurthy, A. Kinkhabwala, and P. J. Schuck, *J. Chem. Phys*., **124**, 061101 (2006).
44. M. Osawa, N. Matsuda, K. Yoshii, and I. Uchida, *J. Phys. Chem*., **98**, 12702-12707 (1994).
45. K. Kim and H. S. Lee, *J. Phys. Chem. B,* **109**, 18929 (2005).
46. Y. Wang, H. Chen, S. Dong, and E. Wang, *J. Chem. Phys*., **124**, 074709 (2006).
47. E. B. Wilson, *Phys. Rev*., **45**, 706 (1934).
48. X. Li, Q. Huang, V. I. Petrov, Y. Xie, Q. Luo, X. Yu, and Y. Yan, *J. Raman Spectrosc.*, **36**, 555-573 (2005).
49. W. Hill and B. Wehling, *J. Phys. Chem.*, **97**, 9451-9455 (1993).
50. D. P. Fromm, A. Sundaramurthy, A. Kinkhabwala, P. J. Schuck, G. S. Kino, and W. E. Moerner, *J. Chem. Phys*., **124**, 061101 (2006).
51. Y. Wang, H. Chen, S. Dong, E. Wang, *J. Chem. Phys*., **125**, 044710 (2006).

52. Z. Sun, C. Wang, J. Yang, B. Zhao, and J. R. Lombardi, *J. Phys. Chem. C*, **112**, 6093-6093 (2008).

53. Q. Zhou, G. Zhao, Y. Chao, Y. Li, Y. Wu, and J. Zheng, *J. Phys. Chem. C*, **111**, 1951-1954 (2007).

54. G. K. Liu, J. Hu, P. C. Zheng. G. L. Shen, J. H. Jiang, R. Q. Yu, Y. Cui, and B. Ren, *J. Phys. Chem. C*, **112**, 6499-6508 (2008).

55. Y. Huang, H. Zhu, G. Liu, D. Wu, B. Ren, and Z. Q. Tian, *J. Am. Chem. Soc.,* **132**, 9244-9246 (2010).

56. P. Hildebrandt and M. Stockburger, *J. Phys. Chem.*, **88**, 5935-5944 (1984).

57. M. Futamata and Y. Maruyama, *Anal. Bioanal. Chem*., **388**, 89-102 (2007).

58. A. Palonpon, T. Ichimura, P. Verma, Y. Inouye, and S. Kawata, *J. Raman Spectrosc*., **40**, 119-120 (2009).

59. A. Palonpon, T. Ichimura, P. Verma, Y. Inouye, and S. Kawata, *Appl. Phys. Express*, **1**, 092401 (2008).

60. Q. Zhou, X. Li, Q. Fan, X. Zhang, and J. Zheng, *Angew. Chem. Int. Ed*., **45**, 3970-3973 (2006).

61. R. Smoluchowski, *Phys Rev*., **60**, 661 (1941).

62. D. R. Ward, N. J. Halas, J. W. Ciszek, J. M. Tour, Y. Wu, P. Nordlander, and D. Natelson, *Nano Lett.*, **8**, 919-924 (2008).

63. D. Wu, X. Liu, Y. Huang, B. Ren, X. Xu, and Z. Tian, *J. Phys. Chem. C*, **113**, 18212-18222 (2009).

64. J. F. Arenas, J. Soto, I. L. Tocón, D. J. Fernández, and J. C. Otero, *J. Chem. Phys*., **116**, 7207 (2002).

65. K. Kneipp, Y. Wang, H. Kneipp, L. T. Perelman, I. Itzkan, R. R. Dasari, and M. S. Feld, *Phys. Rev. Lett*., **78**, 1667-1670 (1997).

66. S. Nie and S. R. Emory, *Science*, **275**, 1102-1106 (1997).

67. N. Hayazawa, Y. Inouye, Z. Sekkat, and S. Kawata, *Opt. Commun*., **183**, 333-336 (2000).

68. N. Hayazawa, Y. Inouye, Z. Sekkat, and S. Kawata, *J. Chem. Phys*., **117**, 1296 (2002).

69. C. C. Neacsu, J. Dreyer, N. Behr, and M. B. Raschke, *Phys. Rev. B*, **73**, 193406 (2006).

70. K. F. Domke, D. Zhang, and B. Pettinger, *J. Am. Chem. Soc*., **128**, 14721-14727 (2006).

71. W. Zhang, B. S. Yeo, T. Schmid, and R. Zenobi, *J. Phys. Chem. C,* **111**, 1733-1738 (2007).

72. J. Steidtner and B. Pettinger, *Phys. Rev. Lett*., **100**, 236101 (2008).

# Chapter 3.
# Nanoscale Raman analysis of multilayer graphene

This chapter presents tip-enhanced Raman analysis of multilayer graphene. It is natural that Raman spectroscopy is useful to determine molecular structures, and especially it makes a significant contribution to characterize carbon-based materials. For example, Raman spectra of multilayer graphene can give information about the crystal disorder, the number of layer, edge structure, interlayer interaction, and other physical properties. There are some key vibrational modes in multilayer graphene for allowing a determination of the physical properties. The nature of the each vibrational mode of multilayer graphene is briefly introduced. I then show some of the Raman analysis of multilayer graphene samples using Raman microscopy and TERS microscopy, and present great capabilities of their microscopy.

## 3.1 Raman scattering of graphene

Graphene is composed of $sp^2$-bonded carbon atoms located at the vertices of a planar honeycomb crystal lattice. I briefly introduce the outstanding properties of graphene. For instance, the breaking strength of graphene is ~ 40 N/m (more than 200 greater than steel), the Young's modulus is ~ 1.0 TPa (Fe is ~ 0.2 TPa), and the room temperature thermal conductivity is ~ 5000 $Wm^{-1}K^{-1}$.[1] Furthermore, the unique band structure of graphene leads massless Dirac electrons in it, which allows the state-of-the-art mobility reaching $2 \times 10^5$ $cm^2/Vs$.[2] Because of the above reasons together with the Novel Prize for physics in 2010, the investigation of graphene has the enormous attention all over the world. For developing the application of graphene-based devices, evaluation of physical properties in graphene is indispensable. Those properties can be elucidated by Raman spectra of the graphene. Figure 3.1(a) shows Raman spectra from multilayer graphene. I explain some of the important vibrational modes as follows.

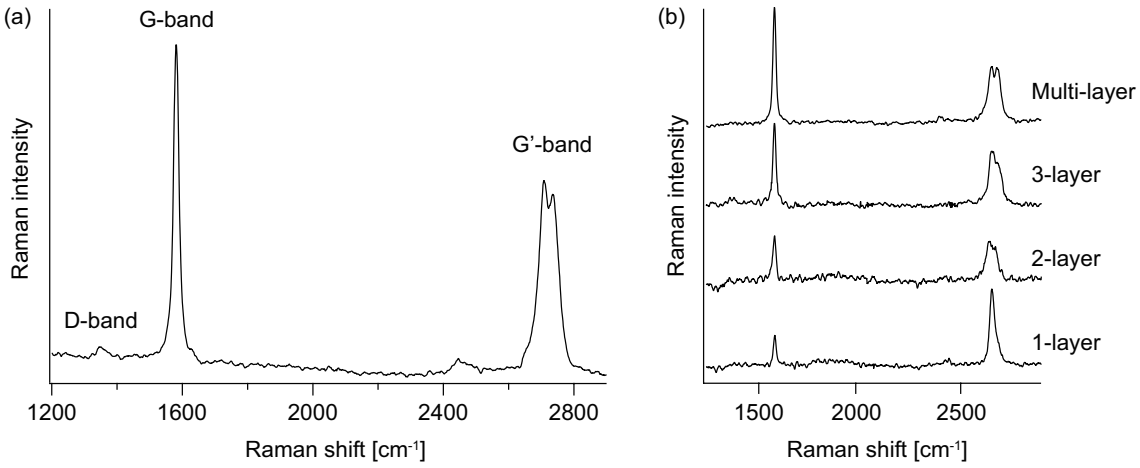


**Figure 3.1** (a) Raman spectrum of multilayer graphene, and (b) Raman spectra of multilayer graphene with the layer of single, double, triple and multiple.

### G-band

The G-band centered at ~ 1581 $cm^{-1}$ is associated with the in-plane vibrational modes of $sp^2$ hybridization of carbon bonding. It is related to the in-plane C-C bond stretching mode, which gives rise to both the TO phonon and the LO phonon branches. The two optical phonon modes are degenerate due to the two-dimensional full rotation symmetry in the graphene hexagonal lattice. The G-band is the fundamental mode for carbon-based materials (where the notation G comes from graphite), thus it is indicative for evaluating an amount of the graphene and confirming the existence.

### D-band

The D-band centered at ~ 1350 $cm^{-1}$ is involved with the vibrational modes of perturbed $sp^2$ hybridization of carbon bonding, and represents crystal disorder in multilayer graphene. The origin of the notation D is generally based on disorder, defect, or diamond. An introduction of the crystal disorder breaks the crystal symmetry of graphene, and activates D-band that would otherwise be inactive. Since disarray of the crystal symmetry is caused by borders of the crystallite areas, the Raman activity of the D-band can indicate the amount of the crystallite boundary in the sample. Therefore, Raman intensity of the D-band becomes strong at the edges of multilayer graphene.[3,4] I note that the D-band intensity also depends upon the crystallite of the boundary.[5,6]

**G'-band**

The G'-band (also called 2D-band) around 2500 – 2700 $cm^{-1}$ is also attributed to $sp^2$ hybridization of carbon bonding. It is associated with an intervalley double-resonance Raman process in which the phonon vector connects two energy bands at the *K* and *K*' symmetry points of the Brillouin zone in graphene.[7,8] Since the G'-band is related to resonance Raman effect, the frequency of the G'-band depends on the laser excitation energy. The G'-band is quite useful to decide the number of graphene layers.[9] Figure 3.1(b) shows Raman spectra of multilayer graphene with the single, double, triple, and multi layers. Single-layer graphene exhibits a single Lorentzian peak in the G'-band, and the intensity of the G'-band is about 2 times larger than that of the G-band. In contrast, double-layer graphene is generally composed of several Lorentzian peaks in the G'-band, and the intensity of the G'-band is reduced to be comparable with that of G-band. As the increase of the number of layer, ratio of the intensity of the G'-band to that of the G-band is gradually decreased. The intensity ratio for more than 6-layered graphene hardly changes with the increase of the layer. The G'-band is also utilized for charactering the graphene interlayer structures. As shown in Fig. 3.1(b), G'-band of the single-layer graphene is split from a one peak into two peaks with the increase of the number of layer. The origin of the two peaks of the G'-band is related to the stacking order occurring along the *c* axis of graphene. There are two types of stacking structures in multilayer graphene. One type has carbon atoms aligning in the direction perpendicular to the graphene layer, while the other type has the alignment in every other layer (so called Bernal stacking order). The change of the G'-band lineshape is resulted from the special electronic structure due to a stacking interaction between the layers of graphene.[10,11] Thus, the G'-band is utilized to assign the number of layer and the stacking structures of interlayers in the multilayer graphene. Note that the Raman shift and the intensity ratio between the G-band and G'-band depend on a substrate on which graphene samples are prepared.[12,13]

## 3.2
## Raman imaging of multilayer graphene

In this section, I show you some of the Raman analysis of graphene samples by means of Raman microscopy. I prepared multilayer graphene deposited on a cover slip from a highly oriented pyrolytic graphite (HOPG) crystal. The deposition of the graphene was done by mechanical cleavage

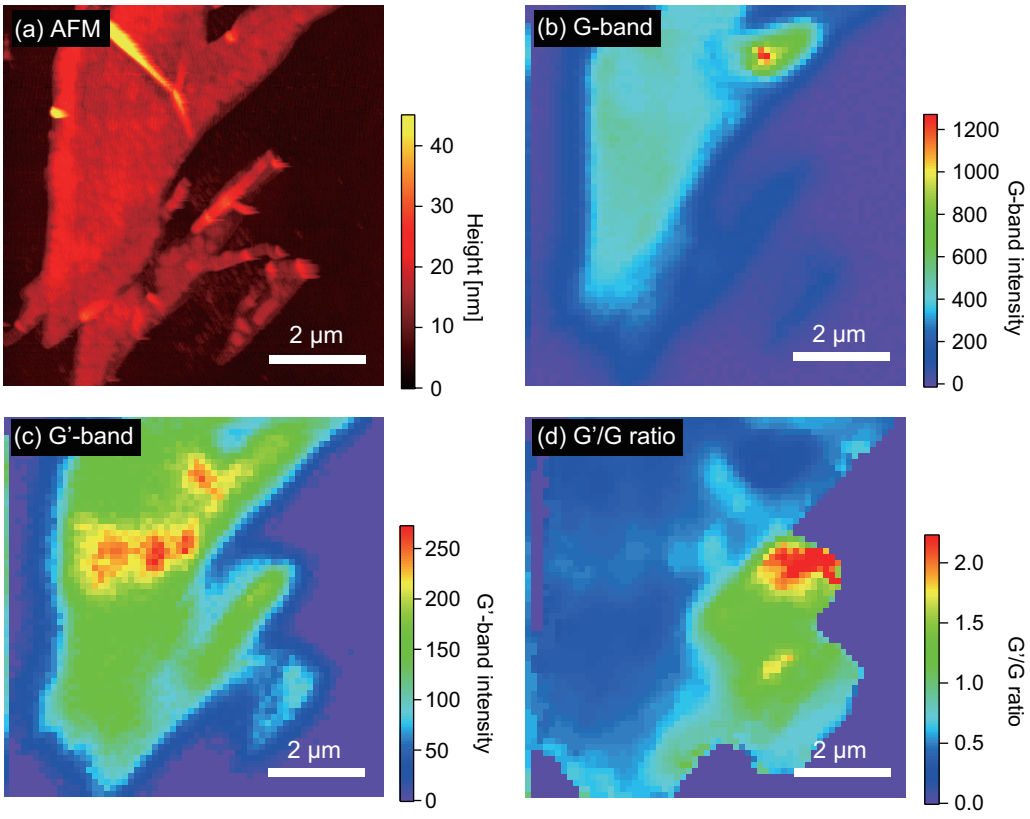


**Figure 3.2** AFM and Raman images of multi-layered graphene deposited on a cover slip. (a) AFM image, (b) Raman image at G-band, (c) Raman image at G'-band, and (d) Raman image constructed by the ratio of G'-band intensity to G-band intensity. Raman excitation wavelength is 532 nm.

method using a scotch tape.[14] Figure 3.2(a) shows an AFM image of multilayer graphene deposited on a coverslip. As you can see, the multilayer graphene was composed of a layered structure where the each layer had a certain area. Next, I measured Raman spectra of the multilayer graphene using Raman microscopy that was introduced in Chapter 1. I utilized 532 nm wavelength laser for the Raman excitation. Figure 3.2(b,c) indicate G-band and G'-band Raman images of the multilayer graphene in the same area as Fig. 3.2(a), respectively. The Raman images were constructed by an area integral of Raman intensities of the nine points around a center of the each Raman peak. Afterward, Raman images were constructed by the area integral of a Raman peak if not otherwise specified. As you can see, the spatial distribution of the multilayer graphene was different according to the Raman mode. For example, the center of the multilayer graphene imaged at the G'-band in Fig. 3.2(c) shows stronger intensity than the other area, while the G-band image doesn't show any localized distribution around the center. This result implies that amount of carbon atoms around the cen-

ter of the multilayer graphene is not changed much in terms of the stationary G-band intensity, but the stacking interaction between the graphene layers is different around the center. Since the surface of the multilayer graphene doesn't represent notable changes in structure judging from the AFM image, the variation of the stacking interaction observed in Fig. 3.2(c) may occur in interlayers of the multilayer graphene. For the further analysis, I show a Raman image constructed by the ratio of the G'-band to the G-band intensity as shown in Fig. 3.2(d). The important thing is that the distribution of the G'/G-band ratio reflects the number of layers in the multilayer graphene. Referring to Fig. 3.1(b), it can be expected that the ratio ~ 2 indicates single-layered graphene, ratio ~ 1.2 is for a double layer of graphene, and ratio ~ 0.7 is for a triple layer of graphene, and ratio ~ 0.5 is for more than four layers of graphene. As you can notice, single-layered graphene exists in the red area of Fig. 3.2(d), although it is not clearly observable in Fig. 3.2(a-c).

The crystalline orientations of multilayer graphene at the edges can be also investigated by the Raman microscopy.[5,6] I measured Raman spectra of multilayer graphene near the edges and analyzed the crystalline orientations. Figure 3.3(a) is an AFM image of multilayer graphene with a sharp corner of ~ 30º at the top. Figure 3.3(b,c) are the corresponding Raman images taken at the G-band and the D-band, respectively. The Raman images were taken with the linear-polarized laser parallel to the vertical axis of the Raman images. As you can see, the G-band image indicates a similar distribution to the AFM image, and the intensity of the G-band is uniform over the sample. On the other hand, the D-band image shows a quite different distribution, and in particular the right side of the edge indicates strong Raman intensities comparing with the left side. The uneven distribution of the D-band near the edges is understood from the aspect of the possible crystalline orientations of the multilayer graphene. To tell the conclusion first, a perfect zigzag edge cannot show D-band mode of graphene, and a perfect armchair edge can show the D-band mode. This is due to the forbidden transition of intervalley double-resonance Raman process associated with the defect for a zigzag edge.[15,16] From the point of view about the corner angle of 30º, the possible crystalline orientations at the top-vertex of the multilayer graphene are concluded as shown in Fig. 3.3(d). The multilayer graphene crystalline on the left side forms a zigzag orientation, and it on the right side has an armchair orientation. For the additional information, Raman scattering intensity of the D-band for an armchair orientation depends on polarization direction of the excitation laser, and the intensity takes the maximum value when the polarization direction is parallel to the armchair orientation.[15] It should be emphasized that Raman spectroscopy provides one easy method for distinguishing between armchair and zigzag edges, and the point of Raman microscopy is the comprehensive understanding of the atomic structure of graphene through the spectral imaging.

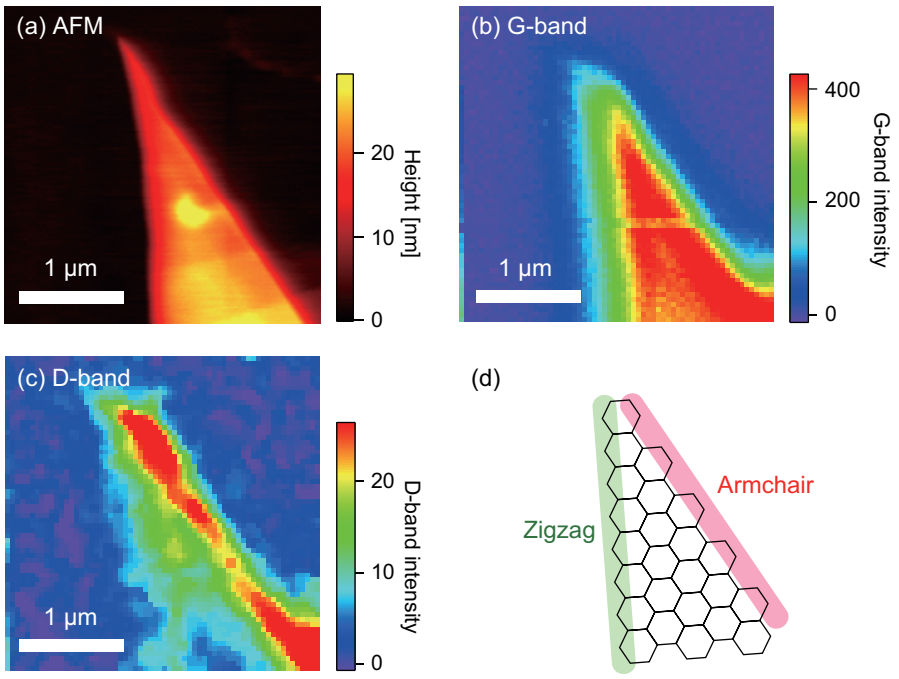


**Figure 3.3** AFM and Raman images of multilayer graphene. (a) AFM image. (b) Raman image at G-band, and (c) Raman image at D-band are taken with the linear-polarized laser parallel to the vertical axis. (d) Schematic illustration of atomic structure at the top-vertex of the multilayer graphene, where the left and right sides form the zigzag and armchair orientations, respectively.

## 3.3
## TERS imaging of multilayer graphene

I have demonstrated Raman imaging of multilayer graphene. It is very useful to characterize the atomic structures, however the accessible resolution is limited to submicron scale, which doesn't allow us to probe nano-scale distributions based on the layer numbers, defects, and other physical properties. I here show tip-enhanced Raman analysis of multilayer graphene using TERS microscopy, which enables the nano-scale analysis. I first prepared multilayer graphene on a glass substrate following to a procedure explained in Section 3.2. Then, I looked for pieces of graphene flakes on the glass substrate through optical microscopy, and took AFM and TERS images around some of the graphene flakes. After the TERS measurement, the far-field images were also measured. In the Raman measurement, the excitation wavelength was 532 nm, the laser intensity was set to 100 μW, the exposure time was 0.5 sec/spectrum, and the single pixel size was 20 × 20 $nm^2$. The laser power

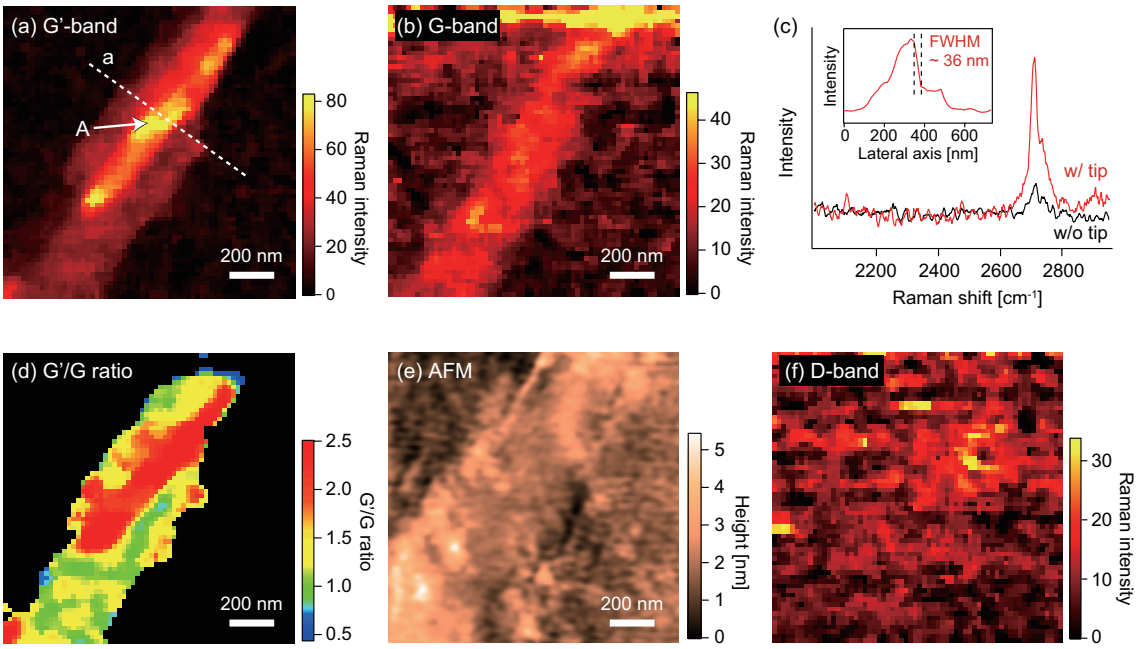


**Figure 3.4** (a,b) TERS images of multilayer graphene at the G'-band and G-band, respectively. (c) (red) TERS and (black) spontaneous spectra of the multilayer graphene, obtained from the point A in Fig. 3.4(a). The inset shows cross section of TERS image along the white dotted line a in Fig. 3.4(a). (d) TERS image constructed of the G'/G ratio, indicating distribution of the number of layers. The black area represents that multilayer graphene doesn't exist. (e) AFM image of the graphene layers. (f) TERS image of the multilayer graphene at the D-band. The pixel size of the each image is $20 \times 20$ nm$^2$.

was optimized for avoiding damages at a metallic tip apex by laser heating, and the exposure time was as reduced as possible with keeping the Raman signals enough to be separated from background noise.

Figure 3.4(a,b) represent TERS images of multilayer graphene deposited on a glass substrate, where the images are constructed of the G'-band signals and the G-band signals, respectively. The far-field signals are already subtracted from the TERS signals, which indicates the pure near-field signals are selectively extracted. As you can see, the graphene structures are clearly observed at the G'-band, while the G-band image is a little bit vague. This is simply because scattering intensity from the G'-band is stronger than that from the G-band. Interestingly, the G'-band image includes some localized areas indicating the strong Raman intensity at intervals while the G-band image shows a certain intensity over the sample. This result is understood by dependence of the Raman enhancement for the G-band and the G'-band on the number of layer. It was reported that the en-

hancement factors decreased with an increase in the number of graphene layers: single-layer > double-layer > triple-layer, and the change is approximately inversely-proportional to the number of layers in the case of the three kinds of layers.[22] Therefore, the G-band intensity balances by the decrease of the enhancement factor and the increase of graphene layers, while the G'-band intensity can be distinguished by its layer number. In addition to the difference of their distributions, only the G-band image shows strong signals at the top of the image (the yellow part). This stems from Raman signals from carbon contaminations attached on a metallic tip, which is often observed in TERS or SERS experiments.[17-19] Figure 3.4(c) shows TERS and spontaneous Raman spectra of the multilayer graphene in the G'-band region, obtained from the point A in Fig. 3.4(a). The red line indicates the TERS spectrum, and the black line indicates the spontaneous Raman spectrum. As you can see, the Raman intensity is dramatically enhanced with the approach of a metallic tip. I estimated the Raman enhancement factor to be ~ 313, regarding the Raman signals in a unit volume. The inset shows a line profile of the TERS image in Fig. 3.4(a) along the white dotted line a. The FWHM was estimated to ~ 36 nm by a Gaussian fitting performed on an edge indicated by the black dotted lines. Judging from the Raman enhancement and the spatial resolution, I confirm that the G'-band and G-band images certainly represent near-field Raman images of the multilayer graphene. Note that the spatial resolution of the TERS images could be improved when size of the each pixel in these TERS images is reduced.

Next, I analyzed a spatial distribution relevant to the number of layers in the multilayer graphene. As I already discussed in previous sections, the number of graphene layers can be estimated from an intensity ratio of the G'-band to the G-band (which is described as G'/G ratio). Figure 3.4(d) expresses a Raman image based on the G'/G ratio. In the case of TERS measurement, the G'/G ratio can be modified by the contact of metal on graphene because the metal contacts induce electron (or hole) doping in the graphene and characteristic electronic structure of the graphene is altered.[23] The doping decreases the G'/G ratio comparing to non-doping graphene.[24] Now, looking at the G'/G ratio with (Fig. 3.4(d)) and without an Ag tip (in Fig. 3.2(d)), the G'/G ratio is increased with the contact of an Ag tip. This result can be comprehended by the hole doping by atmospheric oxygen binding on graphene.[25] The used graphene samples were kept in atmosphere for more than 1 week, so that oxygen molecules could attach onto the graphene surface, and holes were doped to the samples. Indeed, the G-band in the TERS spectra is observed at 1588 $cm^{-1}$, which is blue-shifted by 4 $cm^{-1}$ to pristine graphene and the frequency shift corresponds to the perturbation produced by oxygen bondings.[25] On the other hand, the Ag tip contact works for the electron doping,[24] which compensates holes in the graphene. Thus, the concentration of free carriers in the graphene is reduced by

the Ag tip contact, resulting in the increase of the G'/G ratio. Since the precise determination of the G'/G ratio corresponding to the number of layer is difficult, I assumed the G'/G ratio was increased by a certain proportion with the contact of an Ag tip and roughly estimated the number of layers. The proportion was calculated by taking the maximum values of the G'/G ratio in Fig. 3.2(d) and Fig. 3.4(d), and was estimated to ~ 1.1. Considering the relationship between the G'/G ratio and the number of layers, the color balance was coordinated to roughly describe the number of graphene layers, where the red, yellow, green, and light blue colors indicated the single, double, triple, and more than four layers, respectively. Note that the G'/G ratio depends on impurities attached on surface of multilayer graphene and is altered by ~ 15 % due to modification of the charge-career density inside the graphene,[20] therefore the each color range in Fig. 3.4(d) includes a certain distribution. The black area means there are no graphene layers. As you can see, a wide variety of layers are distributed in the graphene sheet with a narrow width of ~ 400 nm, and the number of layers changes vertiginously at an interval of several tens of nanometer. Figure 3.4(e) is the AFM image simultaneously obtained with Fig. 3.4(a,b). The AFM image is too obscure to confirm the geometry of the multilayer graphene because of the bumpy surface having a roughness of ~ 0.36 nm in a thin region of 400 × 400 $nm^2$ in the center of Fig. 3.4(e). Since a pure graphene has a very flat surface at the atomic level, this roughness implies that some molecules are adsorbed on the multilayer graphene surface. One possible reason for the roughness could be water or oxygen molecules attached on the graphene from the ambient atmosphere in addition to a roughness of a glass substrate.[20,21] The adsorbed molecules on the multilayer graphene can be identified when sensitivity in the TERS measurement is improved.

The crystalline defects were also investigated by the TERS imaging at the D-band signals as shown in Fig. 3.4(f). Although particular points showed a certain level of the signals, a distribution of the defects was not observed owing to the essentially weak intensity of the D-band signals. It is difficult to conclude that either the multilayer graphene doesn't contain any defects or the signal intensity to noise is not enough to identify the defects existing in the graphene. Also, the D-band can be induced by the contact of metal on graphene,[26] therefore tip-enhanced Raman analysis of crystalline defects in graphene should be performed using TERS based on non-contact mode AFM. Although TERS analysis of multilayer graphene revealed the physical properties at the nano-scale resolution, these results pointed to the critical need for the sensitivity improvement in TERS spectroscopy.

## Summary

I have provided Raman analysis of multilayer graphene. I first explained characteristics of Raman modes of multilayer graphene such as G-band, D-band, and G'-band with the basis of the molecular vibrations. Then, I demonstrated Raman imaging of multilayer graphene, where the distribution of the multilayer graphene was visualized by G-band, G'-band, and the number of layer. I also showed distribution of the crystalline defects, and elucidated the crystal orientation on edges of the multilayer graphene. Nano-scale analysis of multilayer graphene was also presented with the usage of TERS microscopy, where the spatial resolution of ~ 36 nm was achieved. It was also confirmed that TERS microscopy was quite useful for analyzing multilayer graphene deposited on a rough surface like a grass substrate in an atmosphere condition because Raman microscopy could selectively visualize the graphene with the basis of the physical properties.

## References

1. C. Lee, X. Wek, J. W. Kysar, and J. Hone, *Science*, **321**, 385-388 (2008).
2. V. S. Morozov, K. S. Novoselov, M. I. Katsnelson, F. Schedin, D. C. Elias, J. A. Jaszczak, and A. K. Geim, *Phys. Rev. Lett*., **100**, 016602 (2008).
3. A. C. Ferrari, J. C. Meyer, V. Scardaci, C. Casiraghi, M. Lazzeri, F. Mauri, S. Piscanec, D. Jian, K. S. Novoselov, S. Roth, and A. K. Geim, *Phys. Rev. Lett*., **97**, 187401 (2006).
4. M. M. Lucchese, F. Stavale, E. H. Martins Ferreira, C. Vilani, M. V. O. Moutinho, R. B. Capaz, C. A. Achete, and A. Jorio, *Carbon,* **48**, 1592-1597 (2010).
5. Y. You, Z. Ni, T. Yu, and Z. Shen, *Appl. Phys. Lett.*, **93**, 163112 (2008).
6. C. Cong, T. Yu, and H. Wang, *Nano Lett.*, **4**, 3175-3180 (2010).
7. A. Jorio, M. Dresselhaus, R. Saito, and G. F. Dresselhaus, *Raman Spectroscopy in Graphene Related Systems*, Wiley-VCH (2011).
8. R. Saito, A. Jorio, A. G. Souza Filho, G. Dresselhaus, M. S. Dresselhaus, and M. A. Pimenta, *Phys. Rev. Lett*., **88**, 027401 (2002).
9. A. C. Ferrari, J. C. Meyer, V. Scardaci, C. Casiraghi, M. Lazzeri, F. Mauri, S. Piscanec, D. Jian, K. S. Novoselov, S. Roth, and A. K. Geim, *Phys. Rev. Lett*., **97**, 187401 (2006).
10. L. G. Cançado, A. Reina, J. Kong, and M. S. Dresselhaus, *Phys. Rev. B*, **77**, 245408 (2008).
11. Z. H. Ni, H. M. Wang, J. Kasim, H. M. Fan, T. Yu, Y. H. Wu, Y. P. Feng, and Z. X. Shen,

*Nano Lett.*, **7,** 2758-2763 (2007).

12. Y. Y. Wang, Z. H. Ni, T. Yu, Z. X. Shen, H. M. Wang, Y. H. Wu, W. Chen, and A. T. S. Wee, *J. Phys. Chem. C*, **112**, 10637-10640 (2008).
13. C. Casiraghi, S. Pisana, K. S. Novoselov, A. K. Geim, and A. C. Ferrari, *Appl. Phys. Lett.*, **91**, 233108 (2007).
14. K. S. Novoselov, A. K. Geim, S. V. Morozov, D. Jiang, Y. Zhang, S. V. Dubonos, I. V. Grigorieva, and A. A. Firsov, *Science*, **306**, 666-669 (2004).
15. L. G. Cançado, M. A. Pimenta, B. R. Dantas, and A. Jorio, *Phys. Rev. Lett*., **93**, 247401 (2004).
16. B. Krauss, P. Nemes-Incze, V. Skakalova, L. P. Biro, K. V. Klitzing, and J. H. Smet, *Nano Lett.*, **10**, 4544-4548 (2010).
17. K. F. Domke, D. Zhang, and B. Pettinger, *J. Phys. Chem. C*, **111**, 8611-8616 (2007).
18. M. Chaigneau, G. Picardi, and R. Ossikovski, *Surf. Sci.*, **604**, 701-705 (2010).
19. T. Schmid, B. Yeo, G. Leong, J. Stadler, and R. Zenobi, *J. Raman Spectrosc.*, **40**, 1392-1399 (2009).
20. B. Krauss, T. Lohmann, D. H. Chae, M. Haluska, K. von Klitzing, and J. H. Smet, *Phys. Rev. B*, **79**, 165428 (2009).
21. F. Yavari, C. Kritzinger, C. Gaire, L. Song, H. Gullapalli, T. Borca-Tasciuc, P. M. Ajayan, and N. Koratkar, *Small*, **6**, 2535-2538 (2010).
22. J. Lee, K. S. Novoselov, and H. S. Shin, *ACS Nano*, **5**, 608-612 (2010).
23. G. Giovannetti, P. A. Khomyakov, G. Brocks, V. M. Karpan, J. van den Brink, and P. J. Kelly, *Phys. Rev. Lett*., **101**, 026803 (2008).
24. A. Das, S. Pisana, B. Chakraborty, S. Piscanec, S. K. Saha, U. V. Waghmare, K. S. Novoselov, H. R. Krishnamurthy, A. K. Geim, A. C. Ferrari, and A. K. Sood, *Nature Nanotech*., **3**, 210-215 (2008).
25. S. Ryu, L. Liu, S. Berciaud, Y. Yu, H. Liu, P. Kim, G. W. Flynn, and L. E. Brus, *Nano Lett*., **10**, 4944-4951 (2010).

# Chapter 4.
# Nanoscale Raman analysis of single-walled carbon nanotubes

The interest in the fundamental properties of single-walled carbon nanotubes (SWNTs) and in their exploitation through a wide range of applications is due to their unique structural, optical, mechanical, electronic, and chemical properties. After two decades of intense researches in SWNTs, more and more attentions are now focusing on the practical applications. For the applications, Raman analysis of SWNTs is quite important for the investigation because the Raman spectrum reflects on the physical properties such as nanotube diameter, defect, electric conductivity, applied strains, chiral coordinate, and energy band gap. In this chapter, I explain fundamental physics of SWNTs about the geometry and the electric properties depending upon the nanotube diameter. I then discuss the important Raman modes and the resonance Raman scattering. Also, I shortly explain the polarization dependence of cross section of the Raman intensity. After discussion of the basic physics, I show Raman analysis of isolated SWNTs through the resonance Raman scattering. Furthermore, nanoscale Raman analysis of strained SWNTs is discussed using relationship between strain in SWNTs and the molecular vibrational modes.

## 4.1
## Resonance Raman scattering of single-walled carbon nanotubes

At the beginning of discussion of Raman scattering from SWNTs, I give some of the physical properties of SWNTs. A SWNT is constructed from a graphene layer by rolling it up into a seamless cylinder. The geometry of a SWNT is defined by the coordinate indicating the orientation direction and it is uniquely determined by the chiral vector $\boldsymbol{C}_h = n\boldsymbol{a}_1 + m\boldsymbol{a}_2$, where $n$ and $m$ are integers and where the vectors $\boldsymbol{a}_1$ and $\boldsymbol{a}_2$ are unit vectors of the graphene layer, as shown in Fig. 4.1(a). In the

shortened ($n$, $m$) form, the chiral vector is written as a pair of integers, and the same notation is generally used to characterize the geometry of ($n$, $m$) chirality. The diameter $d$ of the nanotube can also be characterized by the chirality, and it is expressed in terms of the indices $n$ and $m$ by the relation $d = |\boldsymbol{C}_h|/\pi = a\sqrt{n^2 + m^2 + nm}/\pi$, where $a = |\boldsymbol{a}_1| = |\boldsymbol{a}_2| = \sqrt{3}a_{\mathrm{c-c}} = 0.246$ nm is the lattice constant for the graphene layer and $a_{\mathrm{c-c}}$ is the nearest neighbor C-C distance.[1] As an example, the chiral vector $\boldsymbol{C}_h$ shown in Fig. 4.1(a) is given by $\boldsymbol{C}_h = 3\boldsymbol{a}_1 + \boldsymbol{a}_2$, and thus the corresponding nanotube can be identified by the integer pair (3, 1). Due to the six-fold symmetry of one graphene layer, all nonequivalent nanotubes can be characterized by the ($n$, $m$) chirality. The dispersion of the chirality relies on the production process such as chemical vapor deposition (CVD),[2] high-pressure CO conversion (HiPCO),[3] cobalt-molybdenum catalysts (CoMoCAT),[4] arc discharge methods,[5] and so on.

The distinguishing structure of a SWNT also indicates a unique electronic property. Since SWNTs are one-dimensional (1D) systems, the electronic density of states (DOS) is characterized by their van Hove singularities as shown in Fig. 4.1(b). The population of the electronic states is localized at their van Hove singularities, resulting in the DOS having an energy band gap between the valence and conduction bands. The structure of the DOS changes according to the geometry, hence the energy band gap also depends on the geometry. The DOS can be categorized as two different cases; $n - m = 3l$ and $n - m \neq 3l$, where $l$ is an integer. The former SWNTs show the metallic behavior, and the latter ones show the semiconducting behavior. As shown in Fig, 4.1(b), the DOS of (10, 10) SWNTs has a certain population of the electronic states between the van Hobe singularities across the energy zero, while the DOS of (22, 0) SWNTs cannot allow the electronic states around the energy zero. SWNTs have the several energy band gaps allowing the electron transition (*e.g.* $E_{11}^{\mathbf{M}}$, $E_{11}^{\mathbf{S}}$ and $E_{22}^{\mathbf{S}}$ in Fig. 4.1(b)). The energy band gaps can be depicted as a function of the nanotube diameter as shown in Fig. 4.1(c). This figure is well known as a Kataura plot,[6] and it is often utilized for estimating the energy band gaps of SWNTs. These specific electronic properties are caused by discretization of wavenumber vector in the wave function of electrons along the nanotube circumference. That's why the band gap energy depends on the nanotube diameter. The more detail description is found in textbook.[7]

I next introduce several important Raman modes of SWNTs. Raman spectra of SWNTs represent unique vibrational modes owing to the nanotube structure in addition to Raman modes of graphene. Remarkably, the Raman spectrum can give information of the geometry at the angstrom level. Figure 4.2(a) shows a Raman spectrum of a bundled SWNT in which the important peaks are pointed as G-band, D-band, and radial breathing mode (RBM).

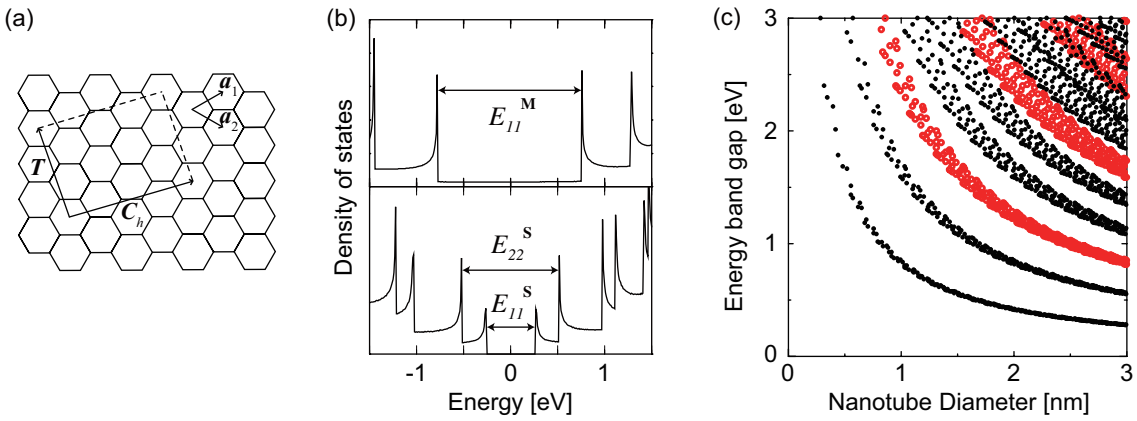


**Figure 4.1** (a) An unrolled nanotube projected on the graphene layer. When the nanotube is rolled up, the chiral vector $\boldsymbol{C}_h$ turns into the circumference of the cylinder, and the translation vector $\boldsymbol{T}$ is aligned along the cylinder axis. (b) Density of electronic states for the upper (10, 10) SWNT, and the lower (22, 0) SWNT calculated with tight-biding model. (c) Energy band gap as a function of diameter for SWNTs (Kataura plot). The red points are for metallic SWNTs, and the black points are for semiconducting SWNTs. [ref. 6, Fig. 7]

### G-band

The root of the G-band around 1500 – 1600 $cm^{-1}$ is same as that of graphene, and it is associated with the tangential vibrational modes of SWNTs. The G-band of SWNTs contains six fundamental modes ($A_{1g}^{+}$, $A_{1g}^{-}$, $E_{1g}^{+}$, $E_{1g}^{-}$, $E_{2g}^{+}$, $E_{2g}^{-}$) that are based on atomic vibrations along the nanotube axis or along the nanotube circumference. The two atomic vibrations are categorized as $G^{+}$ mode ($A_{1g}^{+}$, $E_{1g}^{+}$, $E_{2g}^{+}$, base on the LO phonon) and $G^{-}$ mode ($A_{1g}^{-}$, $E_{1g}^{-}$, $E_{2g}^{-}$, based on the TO phonon), respectively, although the totally symmetric $A_{1g}$ mode usually dominate the spectra. The $G^{+}$ mode frequency is expected to be independent of diameter, since the atomic vibrations are along the tube axis. In contrast, the $G^{-}$ mode has atomic vibrations along the tube circumference, and increasing the curvature increases the our-of-plane components, thus decreasing the spring constant with a $1/d^2$ dependence.[32] The $G^{+}$ mode has higher Raman frequency than the $G^{-}$ mode as shown in the inset in Fig. 4.2(a). The $G^{-}$ band provides information on electronic properties of the SWNTs. The lineshape of the $G^{-}$ mode is broader and asymmetry for a metallic SWNT, and this feature follows a Breit-Wigner-Fano line shapes.[8] This is due to electron-phonon interaction in which the lattice vibration couples to electrons. Therefore, semiconducting SWNTs and metallic SWNTs can be roughly identified by the lineshape of the $G^{-}$ mode. Note that in dealing with metallic SWNTs, the fitting functions for the Raman spectrum should be carefully treated.[8]

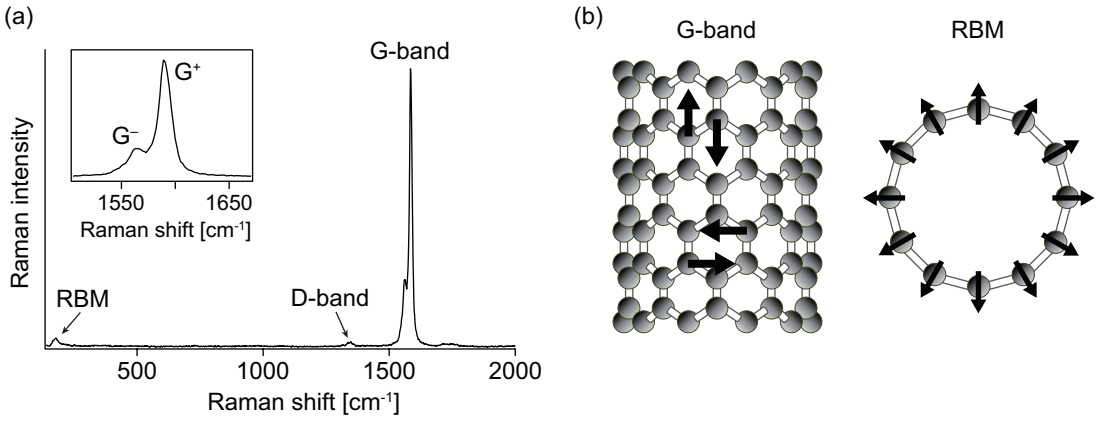


**Figure 4.2** (a) Raman spectrum of a SWNT bundle. The inset figure is a zoomed view of the G-band. (b) Schematic pictures of (left) the G-band atomic vibrations along the nanotube circumference and along the nanotube axis, and (right) the radial breathing mode (RBM) vibrations.

### D-band

The D-band describes the disorder structure in SWNTs, as is the case with graphene. Comparing the G-band intensity to the D-band intensity, the degree of purity of the SWNTs can be quantified as the G/D ratio. The frequency of the D-band is slightly dependent upon the nanotube diameter.[7]

### Radial breathing mode (RBM)

The radial breathing mode (RBM) between 100 – 300 $cm^{-1}$ is associated with the carbon atom vibration oscillating in the radial direction with the same phase as if the nanotube is breathing (see Fig. 4.2(b)). The atomic motion does not break the tube symmetry, that is, the RBM is a totally symmetric $A_1$ mode. RBM is very useful for characterizing the nanotube diameter through a relation $\omega_{\mathrm{RBM}} = A/d + B$, where $d$ is the diameter and $A$ and $B$ are coefficients depending on the aggregation state of SWNTs. For instance, in dealing with SWNT bundles in micelles suspended in water, $A$ = 223.5 $cm^{-1}$ and $B$ = 12.5 $cm^{-1}$ are suitable,[9] and for an isolated SWNT on an oxidized Si substrate, $A$ = 248 $cm^{-1}$ and $B$ = 0 have been found.[10] The difference is owing to van der Waals attractions between SWNTs in the bundle. Note that the values for $A$ and $B$ vary from one research group to another due to environmental effect from the surrounding medium such as molecules adsorbed from the air.[11-16] From the estimated diameter, the possible chirality of the nanotube can be determined.

In discussion of Raman scattering from SWNTs, the energy band gaps have to be also considered. When Raman excitation energy of light is getting equal to an allowed electron transition energy $E$ of a molecule, efficiency of the Raman scattering from the molecule is significantly intensified. Hence, the Raman spectrum shows dominant information of the molecules resonant with the excitation energy. The effect is called resonance Raman effect, and it gives around $10^{4\text{-}6}$ times larger Raman scattering efficiency than the spontaneous Raman scattering under the resonance condition.[17] Therefore, Raman spectra of bundled SWNTs are dominated by particular SWNTs resonant with the excitation laser unless the every SWNT is resonant with the excitation laser.

Here, I briefly explain the mechanism of resonance Raman scattering. I can refer to equation Eq. (1.8) for the discussion. Supposing that the excitation energy corresponds to an electronic energy band gap between a ground state and a excited state in a molecule, that is $(\omega_e - \omega_m - \omega_i = 0, \text{or } \omega_e - \omega_n + \omega_i = 0)$, the polarizability tensor of the Raman scattering is resonantly enhanced. Note that Placzek approximation is not applicable for describing resonance Raman effect in a precise sense. Figure 4.3 shows an excitation process diagram of the resonance Raman scattering, where an initial and a final vibrational states are assumed to exist in an electronic ground state $|g]$, and a virtual state is assumed to exist in a certain electronic state $|e]$ in a molecule. Under the resonance Raman scattering condition, the multiple virtual states $\sum|v)$ of the molecule can be instantaneously compatible with practically existing molecular vibrational states in the original electronic state. Since the transition probability of Raman scattering allowed through the virtual states is increased, as a result, scattering cross section of the Raman scattering is enhanced. As is discussed above, resonance Raman scattering is associated with energy band gaps of molecules. In this sense, resonance Raman spectroscopy is a powerful tool for high sensitive and selective observation of particular molecules.

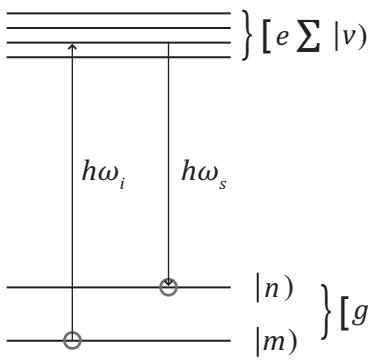


**Figure 4.3** Excitation process diagram of resonance Raman scattering.

## 4.2
## Raman imaging of isolated SWNTs through resonance Raman effect

In this section, I demonstrate Raman imaging of isolated SWNTs through the resonance Raman effect, and discuss what can be elucidated from the Raman images. Before the discussion of Raman analysis of SWNTs, I explain a sample preparation method of SWNTs for separating individually isolated SWNTs from bundled SWNTs for the Raman analysis. Since SWNTs are usually aggregated due to the van der Waals attractions, they have to be dispersed in a solution containing a surfactant for making them isolated. Among the various kinds of surfactants for the dispersion,[18] I utilized 2,2,3,3-tetrafluoro-1-propernol (TFP), because TFP is volatile and doesn't stay adherent around SWNTs in air. SWNTs of 0.4 mg were first put in TFP of 20 ml in a test tube with the capacity of 50 ml, and the mixed solution was sonicated with an ultrasonic homogenizer with the power of 40 W for 30 minute. After leaving it for 30 minutes after the sonication, the supernatant solution was gently pulled out, and dropped by 30 μl on a clean cover slip set on a spin coater. After 1 minute, the cover slip was rotated by 500 rpm for 5 second, and 2000 rpm for 60 second in a row. I finally checked spatial distribution of the SWNTs deposited on the cover slip by the AFM measurements, and I confirmed that the SWNTs were well isolated.

I show you some of the Raman analysis of SWNTs by means of Raman microscopy that I introduced in Chapter 1. Figure 4.4 shows Raman images and an AFM image of SWNTs deposited on a cover slip. Here, CVD-based SWNTs were used as the sample. Figure 4.4(a,b) are the G-band images measured by 532 nm and 442 nm excitation laser, respectively. The excitation lasers were polarized parallel to the vertical axis. As you can see, they represent basically similar distributions of the SWNTs, but some of them are observed only in either of the two images. Considering resonance Raman effect in SWNTs, this result indicates that the CVD-based SWNTs contain both SWNTs resonant with 532 nm and those resonant with 442 nm at least. And, some of the deposited SWNTs are isolated or composed of a few SWNTs that are resonant with either 532 nm or 442 nm. Figure 4.4(c) shows Raman spectra of the bundled CVD-based SWNTs. Considering the lineshape of the $G^-$ mode in Fig. 4.4(c), I can conclude that 532 nm excitation laser is resonant with semiconducting SWNTs, while 442 nm excitation laser is relatively resonant with metallic SWNTs. That is, Raman images in Fig. 4.4(a,b) distinguish the deposited SWNTs in respect to the electric properties. The *in situ* discrimination of the electric properties is the advantage of the Raman microscopy because the AFM image shown in Fig. 4.4(e) is not useful for the purpose.

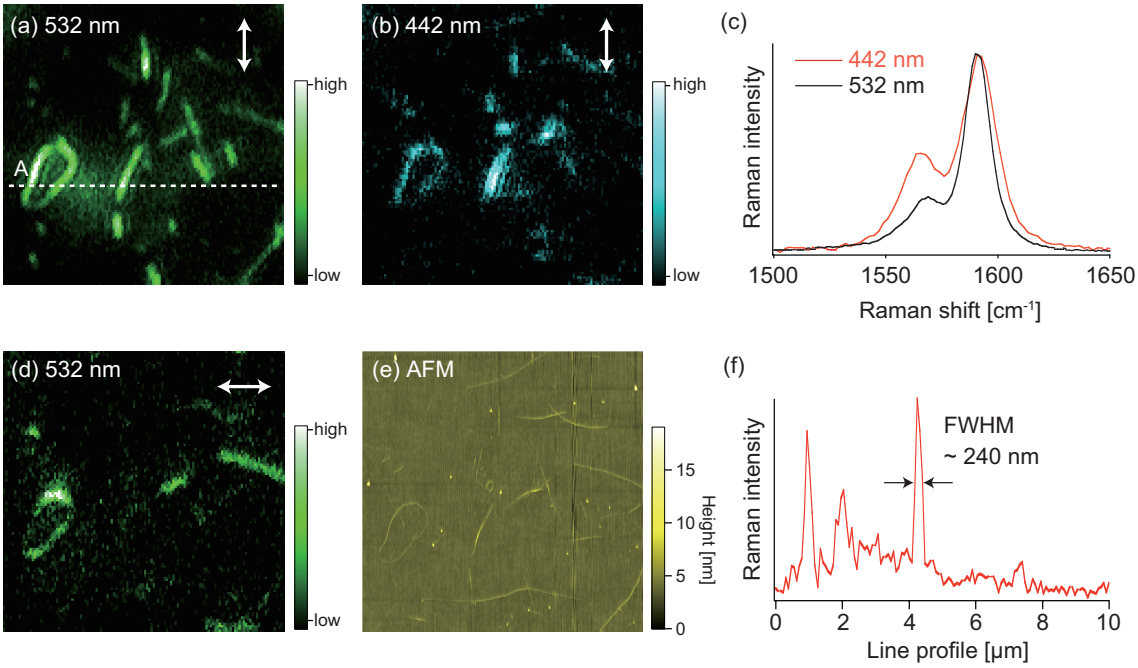


**Figure 4.4** Raman images and the corresponding AFM image of SWNTs deposited on a cover slip. (a) G-band image measured by 532 nm excitation laser, and (b) G-band image measured by 442 nm excitation. Raman image (a) and (b) are taken with the polarization direction parallel to the vertical axis. The white arrows indicate polarization direction of the excitation laser. (c) Raman spectra of the SWNTs measured by 532 nm and 442 nm excitation wavelength. (d) Raman image taken by 532 nm laser with the polarization direction parallel to the horizontal axis. (e) AFM image of the deposited SWNTs, and (f) line profile along the white dashed line A in Raman image (a). The size of these images is 10 × 10 μm$^2$.

I also discuss polarization dependence of Raman scattering cross section of SWNTs. Owing to the 1-dimensional tube structure of a SWNT, SWNTs have an optical anisotropic nature. According to the selection rule of the optical absorption, which directly affects resonance Raman effect, the Raman scattering cross section $I$ can be described as $I \propto \cos^2\theta$, where $\theta$ is an angle difference between the nanotube orientation and polarization of the incident light.[19] Figure 4.4(d) is the Raman image measured by 532 nm excitation laser with the polarization direction parallel to the horizontal axis. Comparing Fig. 4.4(a) with Fig. 4.4(d), SWNTs oriented approximately parallel to the incident polarization are selectively observed. This Raman investigation of the nanotube orientations can be quite useful for an evaluation of the alignment of SWNTs embedded in a polymer film and of vertically aligned carbon nanotubes arrays on a substrate.[20,21]

Finally, I mention spatial resolution of the Raman microscopy. Figure 4.4(f) is a line profile plotted along the white dashed line A in Fig. 4.4(a). The spatial resolution can be given by the FWHM, and it was estimated to be ~ 240 nm. The theoretical resolution of the optical microscopy is calculated as $0.61\times\frac{\text{wavelength}}{\text{NA}}$, and it is estimated to be ~ 230 nm, which indicates that my Raman microscopy shows the best performance.

## 4.3
## Relationship between strain in SWNTs and the vibrational modes

As the other application of Raman spectroscopy for analyzing SWNTs, I demonstrate to investigate strain induced in SWNTs using the Raman spectroscopy. When SWNTs are deformed by some sort of forces, bond lengths and angles between carbon atoms in the lattice of the SWNTs are perturbed.[22,23] The deformation of the bonding conformation changes the bonding forces between the carbon atoms. When the atomic distance is enlarged, the bonding force becomes weak, and vise versa according to the tight-binding model.[24] Given a molecular vibration is represented by a harmonic oscillation model, the natural oscillation of the vibrational modes in SWNTs is shifted to lower frequency as the atomic distance is increased. Since the amount of the frequency shift under a certain strain is proportional to natural oscillation of the each Raman mode, the G-band is much shifted than the RBM.[7] Also, the perturbation of the atomic distance varies slightly on position of carbon atoms in the lattice, thus Raman spectrum of deformed SWNTs is broadened. Since the frequency shift of the Raman mode depends on the change of the atomic distance, the induced strain can be analyzed from the Raman spectrum.

The strain can be categorized as tensile (also called uniaxial) strain and torsional strain as shown in Fig. 4.5(a). The tensile strain always makes the length of C-C bonds longer, while the torsional strain shortens and elongates the bond length depending on the position of the C-C bonds in the SWNT.[25] The perturbation of the bond length causes the frequency shift in the Raman modes. Here, I focus on the G-band shift because the RBM is not sensitive to the perturbation because of its primitively low frequency. The frequency shift under the tensile and torsional strain can be estimated with the usage of density function theory (DFT) or tight biding model.[26] Figure 4.5(b) expresses the calculated shifts in the $G^+$ mode and $G^-$ mode of a SWNT possessing (10, 0) chirality under tensile and torsional strain. The horizontal axis for the tensile is described by the relative increase in length $\partial L / L$, where $L$ is the initial length and $\partial L$ is the stretched length, and the horizontal axis for torsional

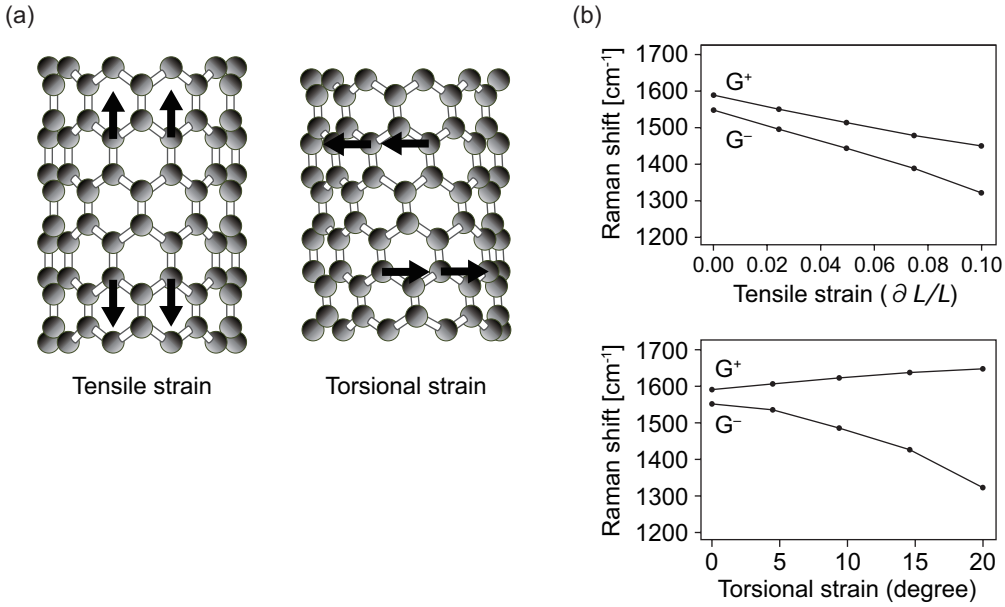


**Figure 4.5** (a) Schematic illustrations of a SWNT deformed by tensile strain and torsional strain. (b) Calculated shifts in the $G^+$ mode and $G^-$ mode of a SWNT possessing (10, 0) chirality under (upper) tensile and (lower) torsional strain. The each horizontal axis for the tensile and torsional strain is described by the relative increase in length $\partial L / L$ and the angle of twist caused by rolling of a SWNT, respectively.

strain is depicted by the angle of twist caused by rolling of a SWNT. The $G^+$ mode shifts in the lower frequency direction for the tensile strain, while it shifts in the higher frequency direction for the torsional strain. And, the $G^-$ mode shifts in the lower frequency direction under either strain. In conclusion, the two types of strain induced in SWNTs can be identified from the frequency shift of the $G^+$ mode and $G^-$ mode. Note that the amount of the frequency shift depends on chirality of the SWNTs although the tendency of the frequency shift is same in any types of SWNTs.[25]

## 4.4
## Raman analysis of strained SWNTs

With the relationship between strain in SWNTs and the vibrational modes in place discussed in previous section, we are now ready to start analyzing Raman spectra of strained SWNTs. I first prepared strain-induced SWNTs. Since SWNTs deposited on a glass coverslip following the procedure introduced in Section 4.2 seldom included strain spontaneously, I utilized an AFM manipulation

method for applying strain on SWNTs.[22,27,28] In the AFM manipulation method, a part of SWNTs on a substrate was dragged by a cantilever apex with maintaining the tip-applied vertical force constant at 20 nN. Since SWNTs were physically adhered on the substrate due to the van der Waals force, surroundings of the manipulated point was partially distorted in the direction of the tip scanning. The distortion resulted in local rolling, stretching, and shifting of the SWNTs. Meijo Nano SWNTs (which was prepared by the arc discharge method) were used as the sample. The diameter distribution of Meijo Nano SWNTs was ~ 1.4 nm and the resonance condition could be estimated to ~ 2.5 eV from the Kataura plot, so that 488 nm excitation wavelength was utilized for the Raman measurement.

Figure 4.6(a) is an AFM image of partially manipulated SWNTs, where there are two bundled SWNTs. The center of the both SWNTs was dragged by an AFM probe along a predefined path perpendicular to orientation direction of the each bundle. By the manipulation, there would be a simultaneous rolling and sliding movement of the SWNTs, giving rise to strain in the SWNTs. Figure 4.6(b) shows the Raman spectra measured at the point A, B, and C in Fig. 4.6(a). The point B corresponds to the manipulated point. As you can see, the Raman spectrum from the point B in the G-band region shows a broader Raman spectrum comparing with those from the other two points. As it is already explained that peak position and intensity of the G-band are sensitive to the strain induced in the SWNTs,[29-31] this result indicates that some sort of strain can be applied only around the point B. On the other hand, the three Raman spectra in the RBM region represent the different peak positions each other as shown in the inset. Since the frequency of the RBM is not sensitive to the strain,[29,30] the slight change of the each RBM peak at the point A, B, and C can be due to different types of SWNTs in the bundle. To verify physical properties and distribution of the strain, I performed Raman shift imaging of the bundled SWNTs with peak positions of the $G^+$ mode and the $G^-$ mode as shown in Fig. 4.6(c) and (d), respectively. The area where SWNTs didn't exist enough to provide the detectable Raman scattering was filled in the black color. Note that the peak positions of them were obtained by executing double Lorentzian curve fitting on the Raman spectra. As shown in Fig. 4.6(c), you can see two localized blue spots corresponding to the manipulated points in the SWNTs while the other area basically shows white color, indicating the blueshift of the $G^+$ mode at the manipulated points by ~ 5 $cm^{-1}$ compared with the entire area. On the contrary, the $G^-$ mode shows the redshift by ~ 4 $cm^{-1}$ at the manipulated points as shown in Fig. 4.6(d). Since the spectral accuracy of used spectroscope is less than 1.7 $cm^{-1}$, the shifts surely represent the change of the Raman modes. Here, I discuss what types of strain is induced in the manipulated points. At the manipulated point B in Fig. 4.6(a), the peak position of the $G^+$ mode shows blue-shifted while that of the

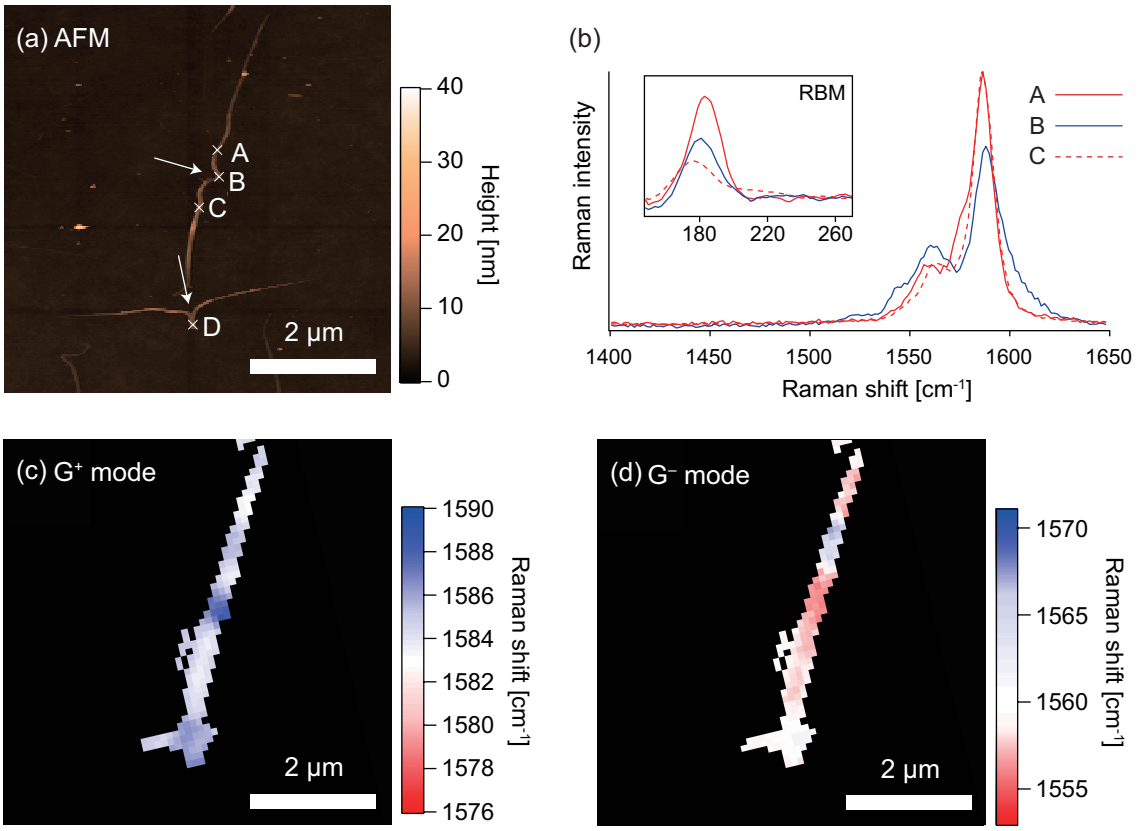


**Figure 4.6** (a) AFM image of partially manipulated SWNTs. The white arrows indicate the manipulated points and directions. (b) Raman spectra measured at the point A, B, and C in Fig 4.6(a). The red, blue solid lines are from the point A and B, respectively and the red dotted line is from the point C. The inset figure shows RBM region of the Raman spectra. (c,d) Raman shift image of the SWNTs constructed with the Raman intensity at the $G^+$ mode and the $G^-$ mode, respectively.

$G^-$ mode represents red-shifted. Thus, I can conclude that the strain induced at the point B in Fig. 4.6(a) is mainly associated with the torsional strain, referring to Fig. 4.5. As for the point D in Fig. 4.6(a), the strain is also owing to the torsional strain because of the blueshift of the $G^+$ mode, although the $G^-$ mode didn't indicate apparent Raman shift. This is probably due to the difference of the pressure applied by the strain at the point B and D. Note that both the tensile and torsional strains could be simultaneously applied to the SWNTs by the AFM manipulation, and there would be an interference effect between two kinds of strains on the frequency shift and intensity change, which are not equal to a simple sum over those induced separately by tensile and torsional strains.[25] Here I would also like to mention that I found no noticeable change in the D-band mode, which indicated that the SWNTs didn't develop any recognizable defects during the AFM manipulation.

## 4.5
## TERS imaging of strain distribution within a SWNT

I have demonstrated Raman mapping of strain induced in SWNTs. Although the Raman analysis revealed physical properties of the strain, the analysis was still limited to sub-micro level due to diffraction limit of light. Since SWNTs have nanometric dimensions, the physical properties of the strain might be more complicated when we could see the nanometric scale. Toward the nanometric investigation, I use TERS microscopy for analyzing a strain distribution in structured SWNTs at the nano-scale resolution.

I first prepared structured SWNTs on a cover slip, in which SWNTs were dragged from the several positions by an AFM manipulation technique step-by-step. In the TERS measurement, the excitation wavelength was 488 nm, the laser intensity was set to 75 μW at the focus spot, and the exposure time was 0.85 sec/spectrum. The images were taken in a region of 800 × 800 $nm^2$, and 64 × 64 pixels. A silicon dioxide tip on which Ag was coated with the thickness of 65 nm was utilized for TERS measurements.

Figure 4.7(a) shows an AFM image of structured SWNTs. As you can see, SWNTs were finely structured as "CNT", where the structure was formed from a long SWNT bundle by an AFM manipulation technique and therefore complicated strains could be induced inside the SWNT bundle. Figure 4.7(b) is a TERS image of the structured SWNTs constructed with the G-band signals at 1587 $cm^{-1}$, in which the far-field signals are subtracted from the TERS signals. Although the TERS image quality was not the best, similar distribution of the SWNTs to the AFM image was clearly observed. The spatial resolution of the TERS image was clarified by a cross section profile along the white dashed line a in Fig. 4.7(b), and it was estimated to ~ 47 ± 5 nm that was calculated by a Gaussian fitting performed on the peak as shown in Fig. 4.7(c). Since the spatial resolution was much smaller than the diffraction limit, I confirmed that the TERS image was sure to represent the near-field Raman image.

I investigated Raman mode shifts caused by strain induced in the SWNTs. As I have already discussed in Section 4.3, the strain mainly perturbs the G-band phonon eigenvectors of SWNTs. I selected three points A, B, and C from Fig. 4.7(b) and examined the TERS spectra in the G-band region. Figure 4.7(d) represents the TERS spectra measured from the point A, B, and C, respectively. The each black dotted line indicates the fitted curve that is composed of double Lorentzian function. The two blue lines show the each Lorentzian curve associated with the $G^+$ mode and $G^-$ mode. The black solid line described vertically at 1587 $cm^{-1}$ is a reference line to see a difference of the Raman

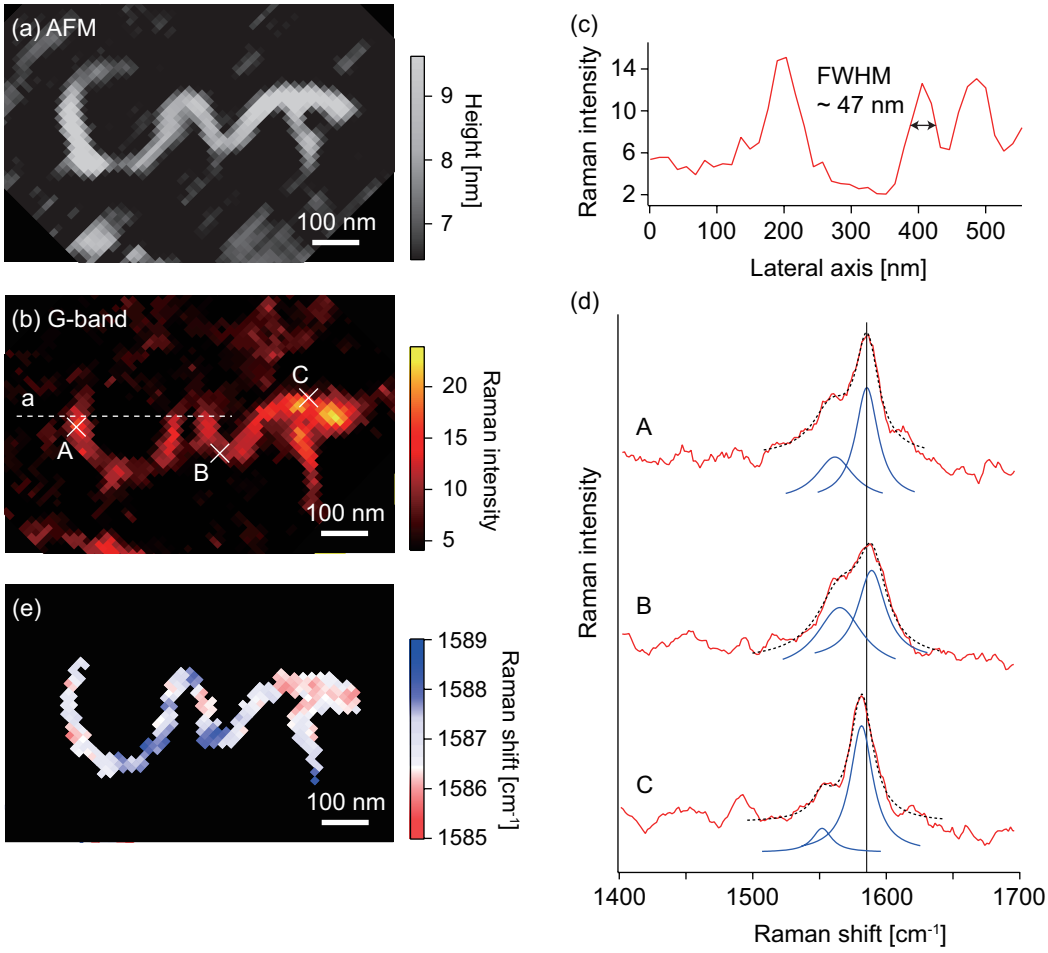


**Figure 4.7** (a) AFM image and (b) TERS image of structured SWNTs. The TERS image is constructed with the G-band signals at 1587 $cm^{-1}$. (c) Cross section profile of the TERS image along the white dashed line a in Fig. 4.7(b). The FWHM is estimated to ~ 47 nm. (d) TERS spectra of the SWNTs measured from the point A, B, and C in Fig. 4.7(b), respectively. The each black dotted line represents the fitted curve that is composed of a double Lorentzian function. The two blue lines show the each Lorentzian curve associated with the $G^+$ mode and $G^-$ mode. The black solid line described vertically at 1587 $cm^{-1}$ is a reference line to see a difference of the Raman shift among the three spectra. In terms of the $G^+$ mode, the spectrum B is blue shifted and the spectrum C is red shifted comparing with the spectrum A. (e) Raman shift image of the $G^+$ mode in Fig. 4.7(b). The color balance of the white area is set to 1586.7 ± 0.5 $cm^{-1}$, which is an average Raman shift of unmanipulated Meijo Nano SWNTs obtained from Fig. 4.6. The blue region is for the blue-shifted $G^+$ mode, and the red region is the red-shifted one. These images are taken in a region of 800 × 800 $nm^2$, and 64 × 64 pixels. The excitation wavelength was 488 nm, the exposure time was 0.85 sec/spectrum, and the laser power was kept to 75 μW at the focus spot.

shift among the three spectra. In terms of the $G^+$ mode, the peak position in the spectrum B is blue shifted by 5 $cm^{-1}$, whereas that in the spectrum C is red shifted by 2 $cm^{-1}$ comparing with that in the spectrum A. Since a blueshift of the $G^+$ mode indicates torsional strain in SWNTs, I conclude that the SWNT bundle at the point B can be twisted, and torsional strain is applied by an AFM manipulation. On the other hand, a redshift of the $G^+$ mode at the point C represents the tensile strain.

For the detail analysis of strain distribution in the SWNT bundle, I constructed Raman shift image of the $G^+$ mode as shown in Fig. 4.7(e), where a peak position of the fitted $G^+$ mode was plotted. The color balance of the white area was set to ~ 1586.7 ± 0.5 $cm^{-1}$, which was an average Raman shift of unmanipulated Meijo Nano SWNTs obtained from Fig. 4.6. Note that the kind of the strain could be estimated from the $G^+$ mode shift as shown in Fig. 4.5(b), therefore I focused on only the $G^+$ mode. The blue region describes the blue-shifted $G^+$ mode, and the red region shows the red-shifted $G^+$ mode. The blue and red regions namely indicate torsional strain and tensile strain, respectively. As you can see in Fig. 4.7(e), the blue and red color distributions are intricately localized in a particular area at the nano scale level.

I would like to consider the strain distribution one by one referring to AFM images of a series of the manipulation performed in the SWNTs as shown in Fig. 4.8. The yellow arrows indicate the each process of an AFM manipulation for the SWNTs. In the procedure (a) to (c), “N” character was structured. When the top-left corner of the “N” was structured from bottom up by the AFM manipulation, the left (A) and write (B) edges around a pushing point 2 in Fig. 4.8(b) could be drastically deformed. The edges would be gradually twisted during the manipulation owing to a friction force caused by van der Waals forces between SWNTs and a glass substrate, resulting in the torsional strain of the SWNTs. At the same time, the SWNTs between the corners of “N” should have been elongated, resulting in the tensile strain. After the top-left corner of the “N” was created, the SWNTs tried to release the induced strain at the corner. However, due to the van der Waals forces, the strain remained. Then, torsional strain could be induced at the top-left corner of the “N”. Eventually, the bottom-left edge and the two corners of “N” depict torsional strain, and the line between the two corners indicates the tensile strain as shown in Fig. 4.7(e). In the procedure (d) to (g), “T” character was structured. When the top line of the “T” was created in Fig. 4.8(d), the line was strongly elongated, and the tensile strain should have been generated. The next process from Fig. 4.8(e) to (g) has a possibility to give both tensile and torsional strain in the SWNTs. On the other hand, the “T” character is basically composed of red color as shown in Fig. 4.7(e), which indicates the tensile strain was dominantly induced. This result can be understood by the change of the friction forces between a glass surface and SWNTs. The “T” character was manipulated by four times in which a part of

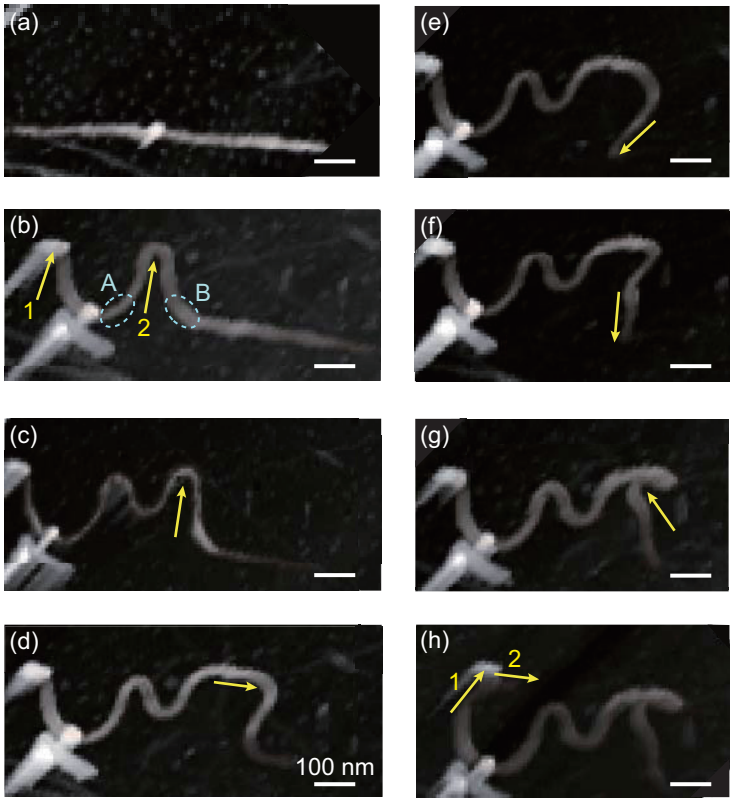


**Figure 4.8** AFM images showing a series of manipulation performed in SWNTs measured in Fig. 4.7(a). These manipulations were performed along the yellow arrows in the each process.

SWNTs may have been slightly removed from the glass surface. When the suspended SWNTs were manipulated, it caused only tensile strain because there were no friction forces between the glass surface and the SWNTs. Thus the "T" character dominantly indicates the tensile strain. The torsional strain in the bottom of the "T" could be induced by the rolling in the step (e) and (f). In the procedure of (b) first and (h), "C" character was structured. The "C" was created by three manipulation processes, which may have also made a part of the SWNTs suspended. As a result, the torsional strain could loosen while the tensile strain was induced. Considering stronger tensile strain could be applied on the exterior SWNTs than the inner ones, it is understood that the tensile strain was selectively induced on the exterior area as shown in Fig. 4.7(e).

Figure 4.9 shows the TERS image of the structured SWNTs in Fig. 4.7(e) integrated with the AFM image in Fig. 4.7(a). The topographic and strain distribution of the SWNTs are clearly visualized simultaneously. The high-resolution characterization technique provides an insight of extremely localized variations of structural properties in nanomaterials in a convenient form of color images.

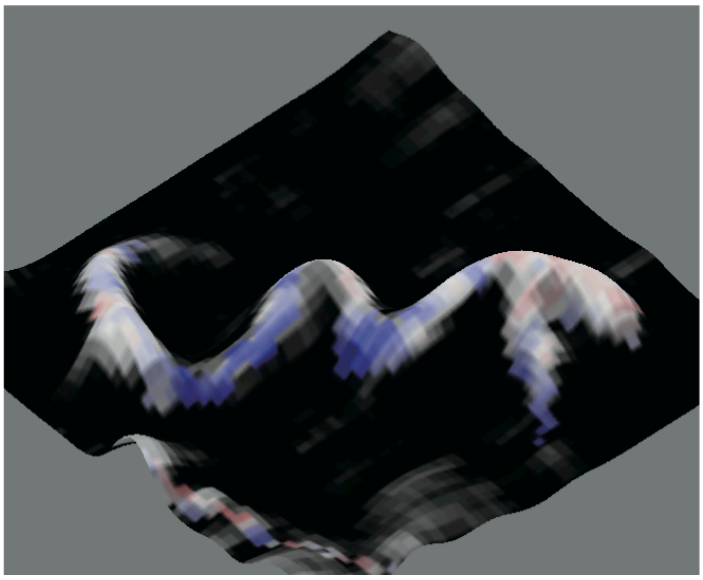

**Figure 4.9** TERS image of structured SWNTs integrated with the AFM image.

Although Raman signals of the RBM and D-band were not observed in this experiment because of the weak Raman intensities, further physical information such as the diameter and crystalline defect could be visualized at the nano-scale resolution when the sensitivity of TERS microscopy is improved.

## Summary

I have provided Raman analysis of SWNTs for investigating the physical properties. I first explained geometry of SWNTs, where the geometry was defined by chirality ($n$, $m$). I then introduced an outstanding electronic structure of SWNTs based on the van Hove singularity caused from the one-dimensional system. And, I showed important Raman modes defined as G-band, D-band, and RBM for characterizing the fundamental geometries of SWNTs. In the discussion of Raman scattering from SWNTs, resonance Raman effect was also described. After reviewing the basic physics in SWNTs, I demonstrated Raman imaging of SWNTs deposited on a cover slip, where I elucidated selective imaging of SWNTs with the basis of the resonance condition and the orientation directions. Furthermore, I showed an application of Raman microscopy for investigating strain distribution in SWNTs. The relationship between strain and vibrational modes in SWNTS was discussed, and it was confirmed that the G-band phonon eigenvectors depended on the tensile and torsional strain.

According to the relationship, distribution of the strain induced in SWNTs was visualized by Raman microscopy. Toward the nanometric analysis of the strain in SWNTs, I performed tip-enhanced Raman analysis of structured SWNTs. As the result of investigation of the $G^+$ mode shift, localized variations of strain properties in the SWNTs were provided at the nano-scale resolution. I was not able to investigate Raman signals of the RBM and D-band in structured SWNTs because of the weak Raman intensities, but further physical information such as the diameter and crystalline defect could be visualized at the nano-scale resolution when the sensitivity of TERS microscopy is improved.

## References


1. R. Saito, G. Dresselhaus, and M. S. Dresselhaus, *Physical Properties of Carbon Nanotubes*, Imperial College Press, London (1998).
2. M. José-Yacamán, M. Miki-Yoshida, L. Rendón, and J. G. Santiesteban, *Appl. Phys. Lett*., **62**, 657 (1993).
3. P. Nikolaev, M. J. Bronikowski, R. K. Bradley, F. Rohmund, D. T. Colbert, K. A. Smith, and R. E. Smalley, *Chem. Phys. Lett*., **313**, 91-97 (1999).
4. B. Kitiyanan, W. E. Alvarez, J. H. Harwell, and D. E. Resasco, *Chem. Phys. Lett.*, **317**, 497-503 (2000).
5. S. Iijima, *Nature,* **354**, 56-58 (1991).
6. R. Saito, G. Dresselhaus, and M. S. Dresselhaus, *Phys. Rev. B*, **61**, 2981-2990 (2000).
7. A. Jorio, M. Dresselhaus, R. Saito, G. F. Dresselhaus, *Raman Spectroscopy in Graphene Related Systems*, Wiley-VCH (2011).
8. M. A. Pimenta, A. Jorio, S. D. M. Brown, A. G. Souza Filho, G. Dresselhaus, J. H. Hafner, C. M. Lieber, R. Saito, and M. S. Dresselhaus, *Phys. Rev. B*, **64**, 041401 (2001).
9. S. M. Bachilo, M. S. Strano, C. Kittrell, R. H. Hauge, R. E. Smalley, and R. B. Weisman, *Science*, **298**, 2361 (2002).
10. A. Jorio, R. Saito, J. H. Hafner, C. M. Lieber, M. Hunter, T. McClure, G. Dresselhaus, and M. S. Dresselhaus, *Phys. Rev. Lett.*, **86**, 1118 (2001).
11. M. Milnera, J. Kürti, M. Hulman, and H. Kuzmany, *Phys. Rev. Lett*., **84**, 1324 (2000).
12. C. Fantini, A. Jorio, M. Souza, M. S. Strano, M. S. Dresselhaus, and M. A. Pimenta, *Phys. Rev. Lett*., **93**, 147406 (2004).

13. H. Telg, J. Maultzsch, S. Reich, R. Hennrich, C. Thomsen, *Phys. Rev. Lett*., **93**, 177401 (2004).
14. A. Hartschuh, H. N. Pedrosa, L. Novotny, and T. D. Krauss, *Science*, **301**, 1354-1356 (2003).
15. M. S. Strano, *J. Am. Chem. Soc.*, **125**, 16148-16153 (2003).
16. S. M. Bachilo, L. Balzano, J. E. Herrera, F. Pompeo, D. E. Resasco, and R. B. Weisman, *J. Am. Chem. Soc*., **125**, 11186-11187 (2003).
17. 濱口宏夫, 平川暁子, ラマン分光法, 学会出版センター (1988).
18. L. Vaisman, H. D. Wagner, and G. Marom, *Adv. Colloid. Interf. Sci*., **128-130**, 37-46 (2006).
19. G. S. Duesberg, I. Loa, M. Burghard, K. Syassen, and S. Roth, *Phys. Rev. Lett*., **85**, 5436-5439 (2000).
20. S. Shoji, H. Suzuki, R. P. Zaccaria, Z. Sekkat, and S. Kawata, *Phys. Rev. B*, **77**, 153407 (2008).
21. L. Qu and L. Dai, *Adv. Mater*., **19**, 3844-3849 (2007).
22. H. W. C. Postma, A. Sellmeijer, and C. Dekker, *Adv. Mater*., **12**, 1299-1302 (2000).
23. T. Hertel, R. Martel, and P. Avouris, *J. Phys. Chem. B*, **102**, 910-915 (1998).
24. G. Wu, J. Zhou, and J. Dong, *Phys. Rev. B*, **72**, 115411 (2005).
25. X. Li, Y. Jia, J. Dong, and Y. Kawazoe, *Phys. Rev. B*, **81**, 195439 (2010).
26. Z. Liu, J. Zhang, and B. Gao, *Chem. Commum.*, **45**, 6902-6918 (2009).
27. T. Hertel, R. Martel, and P. Avouris, *J. Phys. Chem. B*, **102**, 910-915 (1998).
28. M. R. Falvo, R. M. Taylor II, A. Helser, V. Chi, F. P. Brooks Jr., S. Washburn, and R. Superfine, *Nature*, **397**, 236-238 (1999).
29. X. Li, Y. Jia, J. Dong, and Y. Kawazoe, *Phys. Rev. B*, **81**, 195439 (2010).
30. S. B. Cronin, A. K. Swan, M. S. Ünlü, B. B. Goldberg, M. S. Dresselhaus, and M. Tinkham, *Phys., Rev., Lett*., **93**, 167401 (2004).
31. X. Duan, H. Son, B. Gao, J. Zhang, T. Wu, G. G. Samsonidze, M. S. Dresselhaus, Z. Liu, and J. Kong, *Nano Lett.*, **7**, 2116-2121 (2007).
32. A. Jorio, A. G. Souza Filho, G. Dresselhaus, M. S. Dresselhaus, A. K. Swan, M. S. Ünlü, B. B. Goldberg, M. A. Pimenta, J. H. Hafner, C. M. Lieber, and R. Saito, *Phys. Rev. B*, **65**, 155412 (2002).

# Chapter 5.
# Hybridization of plasmons in gap-mode of tip-film system

I have demonstrated TERS spectroscopy for analyzing nanomaterials at the nano scale resolution. Although the tip-enhanced Raman analysis has enabled us to visualize distribution of nanomaterials with the basis of their physical properties, the sensitivity of TERS spectroscopy has not been enough to detect weak Raman vibrational modes that have the low scattering efficiency such as D-band in multilayer graphene and SWNTs. Toward the improvement of the efficiency in TERS, a resonant excitation of plasmon at a metallic tip is crucial. In this chapter, I discuss tunable plasmon resonances in a nano gap between a metallic tip and a metallic nanofilm in TERS spectroscopy, where a nanofilm is defined as a film having a nanometric thickness. When a metallic tip is close to a metallic nanofilm, the plasmon hybridization takes place between localized surface plasmons at the tip and delocalized surface plasmons on two individual surfaces of the nanofilm. The hybridization invokes two plasmon resonance modes that express interesting tunable dependence of the plasmon resonance on the thickness of the nanofilm. The hybridized plasmon modes are varied in the visible to near-infrared spectral regions, which allows obtaining the highest enhancement in TERS through resonant excitation of the localized surface plasmons at the tip apex for any desired excitation suitable for a given sample. In this chapter, I present a theoretical and experimental investigation to understand how the thickness of the nanofilm influences the resonance energy of the hybridized tip-film plasmon modes. I first explain a concept of the plasmon hybridization in tip-film system, and show numerical analysis for understanding physical properties of the plasmon modes depending on the thickness of the nanofilm. Next, I show a fabrication method for obtaining subnano-scale flat metallic nanofilms, and uniformly-coated metallic tips. I then present an optical setup to experimentally elucidate plasmon resonance of the plasmon modes, and discuss the experiment results.

## 5.1
## Plasmon modes and their hybridization in tip-film system

The optical properties of a metallic nanostructure are determined by its plasmon resonances, which are strongly dependent on the geometry. The tunability of plasmon resonances *via* the structure has been one of the reasons for the interest in a rapidly expanding array of metal nanostructure geometries, such as nanorods,[1,2] nanorings,[3] nanocubes,[4,5] and nanoshells.[6] The resonant excitation of plasmons can lead to large local enhancements of the incident electromagnetic field at the nanostructure surface, resulting in dramatically large enhancement of the cross section for optical spectroscopies such as surface-enhanced Raman scattering, as discussed in Chapter 2. The plasmon resonance can be modified across the visible to the near-infrared spectral regions by tailoring plasmonic hybridization of metallic nanostructures.

A metallic tip-film system, composed of a metallic tip apex adjacent to a metallic nanofilm with a nanometric gap, supports plasmon resonances whose energies are determined sensitively by the tip and film geometry. In the tip-film geometry, localized SPPs at a metallic tip apex interact with delocalized SPPs on a metallic substrate at a nano gap, which generates specific hybridized plasmon modes. Since plasmonic properties of metal nanostructures strongly depend on their size and geometries, the plasmon hybridization in a tip-film system can be modified by geometries of the film [7,8] and gap distance.[9-11] For example, it was reported that localized surface plasmon modes upon an Au tip apex above an Au substrate could be tuned from 650 to 680 nm with changing the gap distance.[9] Although the plasmon resonance has been investigated with various kinds of structures, the tunable range of the plasmon resonance is limited to such a narrow resonance window. In this section, I present an idea for greatly expanding the tunable range of the plasmon resonance energies from visible to near-infrared spectral region. I first give a concept of plasmon hybridization for a nano gap in a metallic tip-film system.

To facilitate the discussion, I assume that a metallic tip apex works as a metallic nanosphere and consider plasmon hybridization in a metallic nanosphere-film system to simplify a metallic tip-film system. A plasmon hybridization at the gap of a metallic nanosphere-film system is a consequence of a plasmon interaction between localized surface plasmons of the nanosphere and delocalized surface plasmons propagating on surface of the film. The interaction depends on the relative size of the nanosphere and the thickness of the film. For a metallic film with large thickness, the interaction is image-like, resulting in a redshift of the plasmon resonances with decreasing the nanosphere-film separation.[12,13] However, for a metallic nanofilm, the image of the nanosphere does not

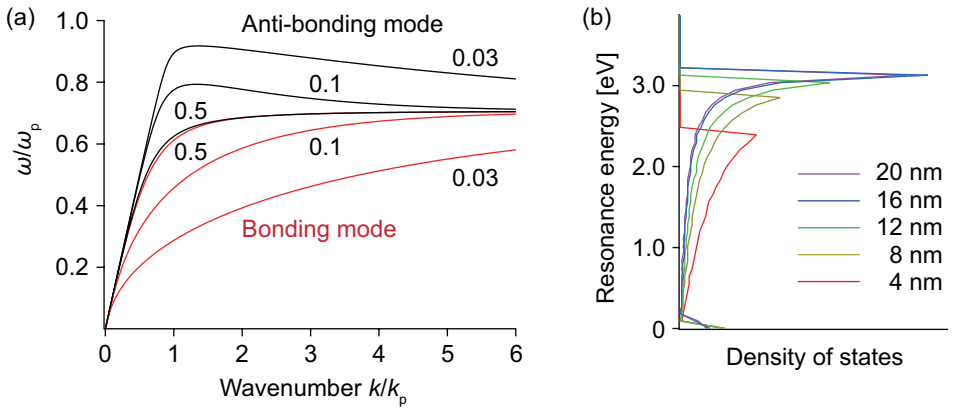


**Figure 5.1** (a) Dispersion relations of surface plasmons on a metallic nanofilm in vacuum. The parameters in the figure indicate a thickness of the nanofilm, which is normalized by wavelength $\lambda_p$ of resonance plasma oscillation in a bulk of the metal. The vertical and horizontal axes are also normalized by frequency $\omega_p$ and wavenumber $k_p$ of the plasma oscillation, where $k_p = \omega_p/c = 2\pi/\lambda_p$ is satisfied. (b) Plasmon density of states in Au nanofilms with the thickness of 4, 8, 12, 16, and 20 nm.

fit inside the nanofilm, and therefore the plasmonic response is fundamentally different. Surface plasmon modes of a metallic nanofilm, in particular, are notably changed as the thickness of a metallic nanofilm decreases. This is because surface charges on the upper surface of a metallic nanofilm start to interact with surface charges on the opposite surface, and the two surface plasmons propagating on the surfaces are no more independent and form two types of coupled plasmon modes; one is bonding film plasmons with symmetric charge alignment on the two surfaces of the nanofilm, and the other is anti-bonding film plasmons with anti-symmetric charge alignment on them.[14] The proper equations of dispersion relations for the bonding and anti-bonding modes are written by

$$\varepsilon_1 k_{z2} + \varepsilon_2 k_{z1} \coth(k_{z2} t/2i) = 0 \tag{5.1}$$

$$\varepsilon_1 k_{z2} + \varepsilon_2 k_{z1} \tanh(k_{z2} t/2i) = 0 \tag{5.2}$$

where, definitions of $\varepsilon_1, \varepsilon_2, k_{z1}, k_{z2}$ are same as those used in Section 2.1, and $t$ is the thickness of a nanofilm. The upper and lower equations are for the bonding and anti-bonding modes, respectively, and the dispersion relations can be described as shown in Fig. 5.1. The red lines are for the bonding mode, and the black lines are for the anti-bonding mode. The parameters in the figure indicate a thickness of the nanofilm, which is normalized by wavelength $\lambda_p$ of resonance plasma oscillation in a bulk of the metal. For instance, the $\lambda_p$ of an Au nanofilm can be estimated to ~ 270 nm.[7] As you can see, the dispersion relations of the bonding and anti-bonding modes are considerably

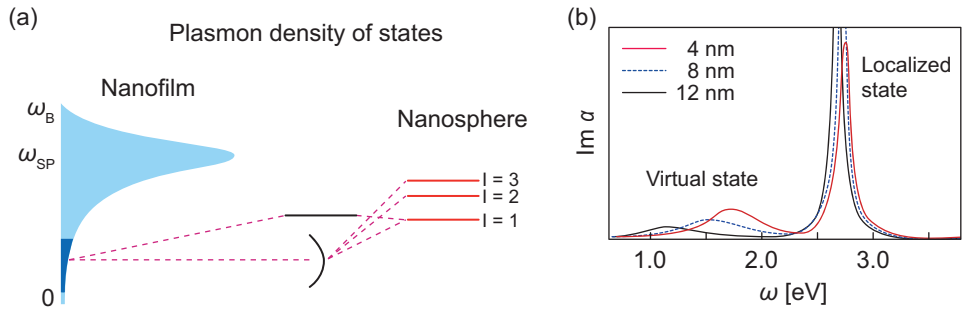


**Figure 5.2** (a) Calculated energetics of the interaction regime for a plasmonic Au nanosphere and the surface plasmons of an Au nanofilm. The plasmonic density of states and the effective continuum of the nanofilm are illustrated in light blue and dark blue, respectively. The red bars indicate discrete localized plasmon states of the nanosphere, and the resulting hybridized plasmons are shown in black. (b) The corresponding spectra for nanofilms of the thickness of 12 (red-solid), 8 (blue-dashed), and 4 nm (black-solid). In this calculation, diameter of the Au particle was 50 nm, and the polarization direction of the excitation light was perpendicular to the Au nanofilm. [ref. 7, Fig. 2]

separated with the decrease of the nanofilm thickness. Especially, the bonding film plasmons strongly interact with localized plasmons in a metallic nanosphere and contribute most of the interaction because the energies of the bonding film plasmon modes are closer to the energy of the localized nanosphere plasmon modes (*e.g.* $\omega/\omega_p = \sim 0.5$ for localized plasmons of an Au nanosphere). To facilitate this discussion in a metallic nanosphere-film system, I focus on the contribution from the bonding film plasmons, although the higher energy anti-bonding film plasmons also play a role. The physical states of surface plasmons in a nanofilm can be intuitively understood by the density of states. Figure 5.1(b) is calculated plasmon density of states in Au nanofilms with the thickness of 4, 8, 12, 16, and 20 nm, respectively. The energy of the plasmons increases as the nanofilm becomes thick, and the density of states takes a stationary state when the thickness is close to 20 nm. This is because the interaction of surface plasmons between upper film surface and lower film surface gets low with increasing the film thickness. Thus, the plasmons in a metallic nanosphere-film system strongly depend on the nanofilm thickness. The hybridized plasmons in a metallic nanosphere-film system were well discussed by Nordlander's group,[7,15] and I would like to explain the plasmonic properties referring to his theory.[7]

Nordlander described the plasmon hybridization in a metallic nanosphere-film system using the spinless Anderson impurity model, in which plasmons are described as incompressible fluid of the conduction electron gas of the particle.[15,16] Figure 5.2(a) shows calculated energetic regimes between

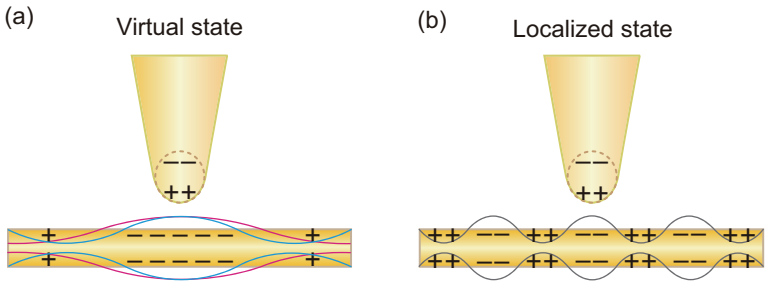


**Figure 5.3** Schematic models of charge distributions for (a) virtual state and (b) localized state in a metallic nanosphere-film system. In the virtual state, localized surface plasmons at the nanosphere efficiently couple to longer wavelength nanofilm plasmons, while in the localized state the localized surface plasmons interact only with short wavelength nanofilm plasmons. Note that the size of the nanofilm is infinite to the in-plane direction.

the discrete plasmon level of an Au nanosphere and the continuum of bonding film plasmon states of an Au nanofilm. The plasmonic density of states for a nanofilm is illustrated in the light blue. As shown in Fig. 5.1, the plasmonic density of state for an infinite film is localized at $\omega_{SP} = \omega_p/\sqrt{2}$ of a single metal-vacuum interface, however it is broadened with decreasing the film thickness and has a continuum state that continuously varies with the wavenumber of the surface plasmons. The nanofilm plasmons at the continuum state can be effectively hybridized with the localized surface plasmons of the nanosphere. The effectively-coupled continuum state is defined as an effective continuum of the nanofilm, which is illustrated in the dark blue in Fig. 5.2(a). The resulting hybridized plasmons are shown in the black in the figure and form two resonance modes; one is a "virtual state" and the other is a "localized state". Figure 5.2(b) shows plasmon resonance energies of their states with the nanofilm thickness of 4, 8, and 12 nm. As you can see, the plasmon resonance energies are clearly varied by the nanofilm thickness, and in particular, it is expected that the plasmon resonance at the virtual state can be widely tuned from visible to near-infrared region.

The physical roots of the virtual and localized states can be described using schematic models of their hybridized plasmons as shown in Fig. 5.3. In the virtual state, the resonance state exists at energies lower than resonance energy of the localized surface plasmons of the nanosphere, where the instantaneous charge polarization of the nanosphere follows the incident field adiabatically. This state is not an eigenstate of the system and can be best described as a superposition of the nanofilm plasmons of wavelengths larger than twice diameter of the nanosphere, as illustrated in Fig. 5.3(a). In general, such nanofilm modes would not be excited for a plane wave excitation, but are here ex-

cited because the near-field from the polarized SPPs at the nanosphere couples directly to the surface charges of sufficiently long wavelength film plasmons through their Coulomb interaction. The largest coupling occurs for nanofilm plasmons with energies equal to the energy of the incident light, where the nanosphere plays a role of antenna for the nanofilm plasmons. Since the energies of the bonding surface plasmons $\omega_-$ of the nanofilm depend strongly on the nanofilm thickness $T$ according to $\omega_- = \omega_{sp}\sqrt{1-e^{-kT}}$ as shown in Fig. 5.1, the energy of the virtual state is highly tuned and decreases with reduced nanofilm thickness. In contrast, the localized state exists above the continuum state of the nanofilm and is essentially premised on screened localized surface plasmons at the nanosphere, where the film plasmons align their surface charges with respect to the surface charges of the nanosphere as shown in Fig. 5.3(b). In this state, due to the energy mismatch between the localized surface plasmons at the nanosphere and the nanofilm plasmons of wavelengths longer than the twice of the nanosphere diameter, the interaction is relatively weak and the screening is predominantly mediated by higher energy short wavelength film plasmons, as shown in Fig. 5.3(b). Since such film plasmons are only weakly dependent on the nanofilm thickness, the localized state does not depend strongly on the nanofilm thickness.

## 5.2
## Numerical analysis of film-thickness-dependence on plasmon resonance

In order to understand physical properties on the hybridized plasmon modes in tip-film system, I first analyzed optical properties of the hybridized plasmons numerically with the usage of FDTD method. As base materials for the metallic nanofilms and tips, I selected Au because it has been reported that plasmon resonance of Au nanostructures could be widely tuned from the visible to near-infrared region.[15,17-24] In the FDTD calculation for the tip-film system, the geometric structure of the tip apex was approximated as an Au nanoshpere,[25] because a metal-coated tip fabricated by vacuum vapor deposition method forms a nanosphere structure at the tip apex. The Au nanoparticle was set on an infinitely large Au nanofilm deposited on a glass substrate. The diameter of the Au nanoparticle was set at 30 nm, and thickness of the nanofilm was varied from 4 to 20 nm. I note that decay length of electric fields attributed to SPPs on an Au nanofilm into the Au nanofilm can be estimated to ~ 30 nm order in visible to near-infrared region, so that the two SPPs on the both surfaces can efficiently couple to each other under the above condition. The gap distance between the nanosphere and the nanofilm was maintained at 2 nm. The gap was then irradiated with a plane light

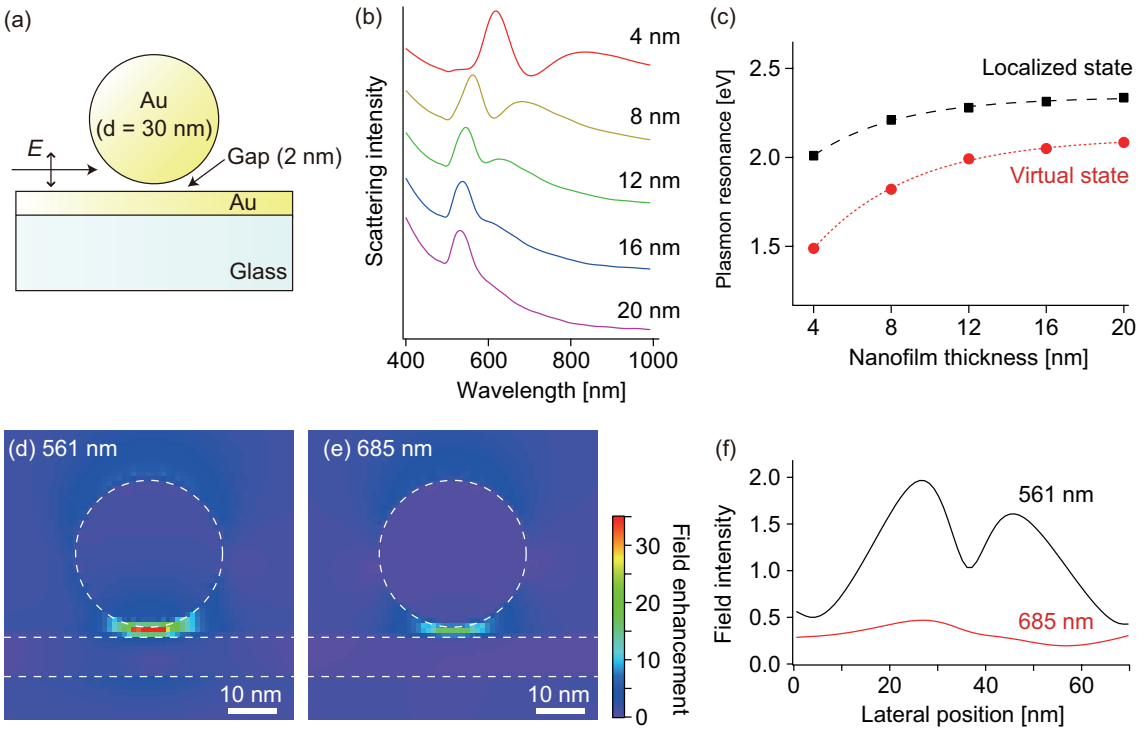


**Figure 5.4** (a) Schematic illustration of nanosphere and nanofilm system for the FDTD calculation. (b) Calculated scattering spectra at a nano gap between an Au nanosphere and an Au nanofilm. The diameter of the Au nanosphere was fixed at 30 nm, and the spectra were calculated for the nanofilm thickness of 4, 8, 12, 16, and 20 nm. (c) Plasmon resonance energy of the nanosphere-nanofilm system as a function of the nanofilm thickness obtained from Fig. 5.4(b). The black squares and red circles represent the plasmon modes in the localized state and the virtual state, respectively. The dashed and dotted lines are the best fits obtained by square exponential curves. (d,e) Electric field distributions of the scattered light for the plasmon resonance at the excitation of 561 nm and 685 nm, respectively, simulated for a combination of 30 nm nanosphere and 8 nm film. The white dotted lines represent boundaries between different materials. (f) Line profiles for Fig. 5.4(d) and (e) along a horizontal axis including the center of the nanofilm. The black and the red curves correspond to the plasmon modes at the excitation of 561 nm and 685 nm, respectively.

wave, which was linearly polarized perpendicular to the surface of the nanofilm (p-polarization) and most efficiently generated localized surface plasmons at the tip apex. Figure 5.4(a) describes a schematic illustration of the calculation model. In the above condition, electric and magnetic field vectors were calculated across a defined region in the nano gap by utilizing the discretized Maxwell equations in 3D space. Regions of the interest near the gap were divided into unit cells of 1 × 1 × 1 $nm^3$, which was small enough to avoid an artificial field enhancement at corners of the structures.

The dielectric constant of Au was taken from Johnson and Christy parameters.[26]

Figure 5.4(b) shows calculated scattering spectra from a nano gap of the tip-film system for nanofilm thickness ranging from 4 to 20 nm, with a nanosphere of diameter 30 nm. As expected, one can see two resonance peaks that stem from the interaction of continuum SPPs on the nanofilm and localized SPPs of the nanosphere. Both peak positions, which represent the plasmon resonance wavelengths, are clearly dependent on the nanofilm thickness and they blueshift with increasing values of the nanofilm thickness. From the theoretical prediction in Section 5.1, the high-energy mode is associated with hybridized plasmons at the localized state, and the low-energy mode is based on hybridized plasmons at the virtual state. The low-energy mode also represents a broad line shape, thus it is expected that the low-energy mode be attributed to the bonding surface plasmon modes in the virtual state. I summarized the plasmon resonance energy as a function of the nanofilm thickness as shown in Fig. 5.4(c). The black squares and red circles represent the plasmon modes in the localized state and the virtual state, respectively. The dashed and dotted lines are the best fits obtained by square exponential curves. It is clear that the high-energy plasmon mode shifts from 2.0 to 2.3 eV and the low-energy plasmon mode shifts from 1.5 to 2.0 eV, respectively, as the nanofilm thickness increases. This wide range tunable resonance of the plasmon modes, controllable through the nanofilm thickness, suggests a potential of precise control of the plasmon resonance energy in the tip-film system. Figure 5.4(d,e) show cross-section of the electric field distributions around the gap for the plasmon resonance at the excitation of 561 nm (localized state) and 685 nm (virtual state), respectively, simulated for a combination of 30 nm nanosphere and 8 nm nanofilm. The white dotted lines represent boundaries of different materials. The field enhancement is dominantly caused at the gap in the both cases, which implies that the scattering spectrum essentially represents the plasmonic property at the gap. Figure 5.4(f) represents line profiles for Fig. 5.4(d) and (e) along a horizontal axis inside the nanofilm, where the black and red curves correspond to the plasmon modes at the excitation of 561 and 685 nm, respectively. The line profiles reflect charge distributions in the metallic nanofilm. When a standing wave of charges is generated in the nanofilm, the electrons are concentrated at nodes of the standing wave, and the electric fields take a maximum value at the center between the nodes and have a minimum value at the nodes. In the case of the excitation of 561 nm, three nodes are found with a symmetric distribution at the center of the line profile and the full width at zero maximum of peaks correspond approximately to the diameter of the nanosphere. Thus, the charge distribution in the nanofilm will be like the schematic illustration shown in Fig. 5.3(b). On the other hand, in the case of the excitation of 685 nm, the electric fields are very broad and don't have particular nodes and peaks. This means that the charge distribution in the nanofilm will be

composed of superposition of the standing waves, as shown in Fig. 5.3(a). These results support my theoretical expectation explained in the previous section.

Here, I should point out the fact that two hybridized plasmon modes are definitely excited in the nanosphere-film system even though the nanofilm is placed between air and a glass substrate. It is known that when refractive indices of the surroundings on the upper and lower surfaces of the nanofilm are different, the bonding surface plasmon modes on the nanofilm are not excited due to wave-vector mismatching between the surface plasmons on the upper and the lower surfaces of the nanofilm. The FDTD results in Fig. 5.4 imply that bonding plasmon modes in tip-film system can be locally excited in the close vicinity of the nano gap and generate the virtual state and localized state. The plasmon hybridization at a nano gap between an Au nanosphere and an Au nanofilm has been well investigated by Peter Nordlander in 2005,[7,15] and my calculated results denote the similar tendency to his works.

## 5.3
## Fabrication of metallic nanofilms and metallic tips

For practical experiments to investigate physical properties of the hybridized plasmon modes in a gap of the tip-film system, I fabricated Au nanofilms and Au tips. Of the wide array of techniques available for the production of metallic nanofilms, I utilized vacuum vapor deposition that was quite well suited for producing metallic nanofilms with the precisely controlled thickness at Å level. Au nanofilms were fabricated by vacuum vapor deposition of 99.9999 % pure Au shots from a resistively heated tungsten boat in a turbomolecular-pumped chamber in which high vacuum was provided down to ~ $10^{-7}$ Torr. Cover slips were used for the evaporation substrates. Prior to the evaporation, the cover slips were cleaned by sequential sonication process to remove impurities on them. Evaporation speed and thickness of evaporated metals were monitored, and the evaporation speed was fixed to 0.2 Å/sec. The evaporation was performed under room temperature.

Au nanofilms for the experiments have to be formed with the surface roughness comparable to subnano scale, because the rough surface of Au nanofilms may generate enhanced fields on the surface asperity.[27] I also would like to avoid radiative decay of non-radiative surface plasmon modes coupling with propagation light due to diffraction grating effects caused by the surface roughness.[28] In order to examine an optimized condition for obtaining a smooth surface of Au nanofilms, I focused on the degree of vacuum during the metal evaporation. Figure 5.5(a,b) show AFM images of

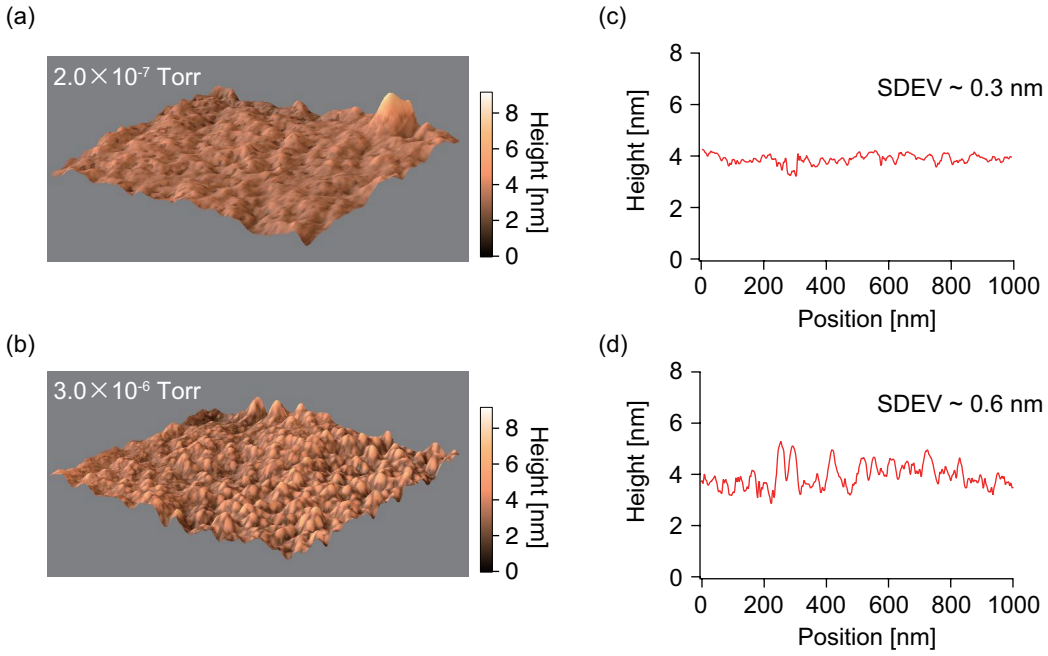


**Figure 5.5** (a,b) AFM images of Au nanofilm with the thickness of 4 nm evaporated under $2.0 \times 10^{-7}$ and $3.0 \times 10^{-6}$ Torr, respectively. The evaporation speed was fixed to 0.2 Å/sec, and the evaporation was performed under room temperature. The measured area is $1 \times 1$ μm$^2$. (c,d) Line profiles of AFM images in Fig. 5.3(a) and (b), respectively. The SDEV represents standard deviation of their surface topography.

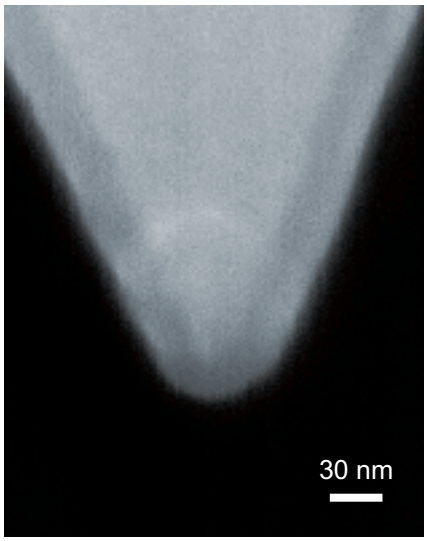


**Figure 5.6** SEM image of an Au-coated silicon tip with the Au thickness of 30 nm.

Au nanofilms with the thickness of 4 nm produced under $2.0 \times 10^{-7}$ and $3.0 \times 10^{-6}$ Torr, respectively. Comparing the two AFM images, Au nanofilms produced under higher vacuum condition give the much smoother surface. For the quantitative verification of their roughness, I plotted line profiles of the surface for their AFM images as shown in Fig. 5.5(c,d). I also introduced standard deviation (SDEV) of the height distribution as the characteristic roughness parameter. As you can see, roughness of Au nanofilms under $2.0 \times 10^{-7}$ Torr is twice as small as that under $3.0 \times 10^{-6}$ Torr. In the high vacuum condition, the number of impurity atoms in vacuum chamber is reduced, and the possibility of collision of the impurity atoms onto an evaporated metal surface is decreased during the evaporation. Therefore, it is concluded that higher vacuum condition is suitable for obtaining the smoother nanofilms. I adopted the $2.0 \times 10^{-7}$ Torr condition for fabrication of Au nanofilms with the any thickness.

For fabrication of Au tips, I coated Au on a silicon cantilever tip by vacuum vapor deposition method. The vacuum degree was kept around $2.0 \times 10^{-7}$ as well as the case of Au nanofilms. Figure 5.6 represents a SEM image of the Au-coated silicon tip with the Au thickness of 30 nm. In this SEM measurement, I applied an accelerating potential of 15 kV to electrons in order to see interfaces between the coated Au and the silicon tip, where a part of the electrons could pass through the Au layers. As you can see, Au layers coated on a cantilever tip are clearly observed, and thickness of the Au layer is uniform around the tip apex. It is also confirmed that the diameter of the Au nanostructure at the tip apex is ~ 30 nm that corresponds to the thickness of the evaporated Au layers. Hence, it is concluded that the thickness of the Au layer on a cantilever tip is precisely controlled by the vacuum vapor deposition method.

## 5.4
## Construction of optical setup for scattering measurement

In this section, I explain an experimental setup for analyzing plasmon resonance energy in a nano gap of the tip-film system. Plasmon resonance energies in a nano gap between a metallic tip and a metallic nanofilm can be investigated by scattering spectra from the gap. For the scattering measurement, I constructed an optical setup that was based on dark-field optical microscopy as shown in Fig. 5.7.

First of all, Xenon lamp passing through a pinhole of 50 μm, which was utilized as a white light source, was collimated with an achromatic lens. It was introduced into an inverted objective lens

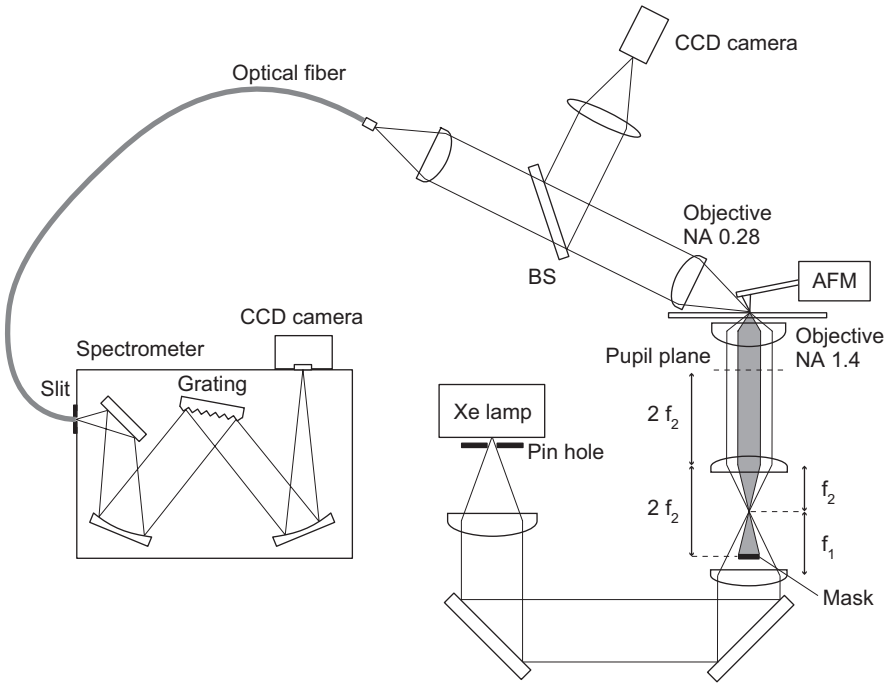


**Figure 5.7** Optical system for scattering measurement from a gap between a metallic tip and a metallic nanofilm. BS is a beam splitter.

through two achromatic lenses ($f_1$, $f_2$) and a mask that rejected the low NA components (NA < 1). The mask was located at the conjugated plane of the pupil of the objective lens, as illustrated in Fig. 5.7. The white light was illuminated on a surface of the metallic nanofilm with the objective lens having the high NA equal to 1.4 (Nikon, Plan Apo), where the white light generated an evanescent field. Then, a metallic tip was approached and moved at the focused position, where a distance between the tip and the substrate was precisely controlled by a feedback system using a quadrant detector. When a metallic nanofilm was set as the substrate, the gap-mode configuration was completed. After the tip adjustment, scattering light from the gap between the tip and the nanofilm was collected by a long working distance objective lens having the NA of 0.28 (Mitsutoyo, Plan Apo), and lead to a spectrometer through an optical fiber. A part of the scattering light was also guided to a CCD camera for adjusting position of the long working distance objective lens. The scattering light was dispersed by a grating, and focused on a liquid nitrogen cooled CCD camera (Roper, 1340 × 400 channel, -100 Cº). The grating had blaze wavelength of 600 and 1200 lines/mm that was chosen according to the necessary spectral resolution.

## 5.5
## Experimental results

I here show scattering spectra in a nano gap of the Au tip-film system, and discuss the plasmon resonance modes. Figure 5.8(a) represents scattering spectra from a nano gap in the Au tip-film system measured with the nanofilm thickness of 4, 8, 12, 16, 20 nm, and without a nanofilm, respectively. The diameter of the Au tip was 30 nm for the all spectra. In the scattering measurements, the Au tip apex was contacted on the Au nanofilm, in which a gap distance between the tip and the nanofilm was estimated to less than 1 nm. This is because the Au nanofilms have a roughness of ~ 0.3 nm and the tip apex of 30 nm cannot contact to bottom of surfaces of the nanofilms. These spectra were corrected for background signals by the subtracting spectra obtained without the tip from corresponding spectra obtained with the tip. The each background-subtracted spectrum was divided by a spectrum of the incident light for the normalization. Finally, the spectra were offset on intensity scale for their facile visualization. The procedure for the normalization can be easily understood by using equations. The intensity of the scattering and incident light must be described as a function of wavelength, and I put them as $Scat(\lambda)$ and $Inci(\lambda)$, respectively. The filed enhancement in a nano gap should also depend on the wavelength, and it can be depicted as $E(\lambda)$. The background scattering light can be written as $Back(\lambda)$. Using these assumptions, the scattering light is described by

$$Scat(\lambda) = E(\lambda) \times Inci(\lambda) + Back(\lambda) \tag{5.3}$$

This equation can be solved for the field enhancement, and it is finally written as

$$E(\lambda) = \big(Scat(\lambda) - Back(\lambda)\big)/Inci(\lambda) \tag{5.4}$$

Therefore, the procedure for the normalization of the scattering spectra exactly follows Eq. (5.4). I here note that the background scattering light should not be observed without a metallic tip because the incident light excites non-radiative surface plasmons or is totally reflected on the glass substrate. Actually, however, the background scattering light was always detected in my experiments, which was probably owing to radiative decay of surface plasmons on metallic nanofilms by the sub-nano-scale surface roughness.[29]

As shown in Fig. 5.8(a), two plasmon resonance modes are observed in the all spectra, which are associated with the bonding surface plasmon modes at the localized state and the virtual state. For the 12 nm nanofilm, two Lorentzian curves were performed to estimate the peak positions. The both modes appear in the visible to the near infrared region, and their peak positions change signify-

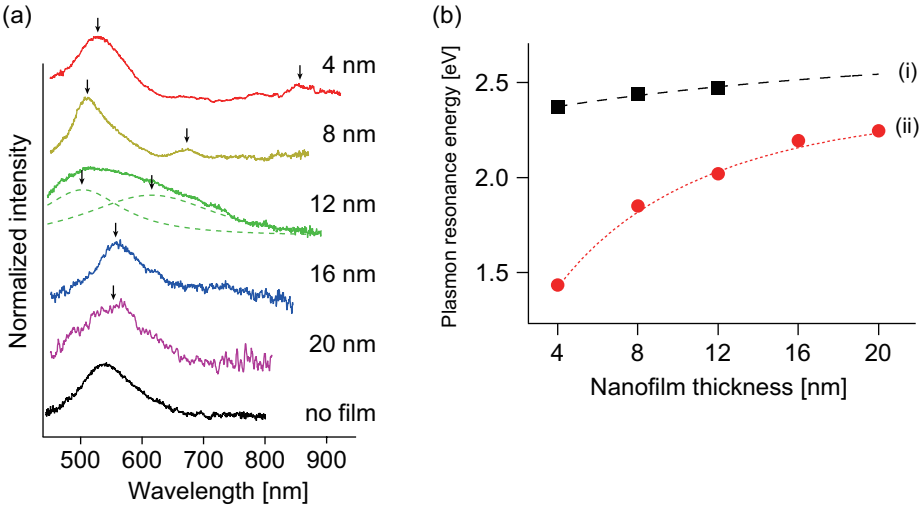


**Figure 5.8** (a) Scattering spectra of Au tip-film system measured with film thickness of 4, 8, 12, 16, 20 nm, and without a nanofilm, respectively. The diameter of the Au-coated tip was 30 nm for all spectra. The two dotted lines for 12 nm nanofilm represent Lorentzian fittings. The arrows indicate the plasmon resonance peaks that shift with the nanofilm thickness. (b) Plasmon resonance energy of the tip-film system as a function of the nanofilm thickness obtained from Fig. 5.8(a). The squares and the circles in (i) and (ii) represent the higher and the lower energy modes, respectively. The dashed and dotted lines are the best fits obtained by using square exponential curves to guide the eyes.

cantly with the nanofilm thickness. This behavior of experimentally observed spectra is akin to my FDTD calculation in Fig. 5.4. Note that polarization of the incident white light in this experiment includes not only the p-polarization components but also the s-polarization components, however the plasmon interaction between the tip and the nanofilm should dominantly occur by the p-polarization.

The plasmon resonance energy as a function of the nanofilm thickness was plotted in Fig. 5.8(b) for a better visualization of the plasmon modes observed in Fig. 5.8(a). Since the plasmon resonance energy is expected to change continuously with the nanofilm thickness, the experimental results were fitted by two least square exponential curves, which guides the eyes. They are predicted to be associated with the lower and the higher energy modes, respectively, although the higher energy mode is observed only for the nanofilms with thickness 4, 8, and 12 nm. The lower plasmon energy is noticeably blueshift from the near-infrared to visible region with increasing the nanofilm thickness. One the other hand, the higher energy mode shows much weaker dependence on the thickness. These results are well corresponding to my prediction in Section 5.1. Interestingly, the

resonance energy of the lower plasmon modes also goes close to the plasmon energy of the Au tip without a nanofilm by an increase of the nanofilm thickness. Although the plasmon energy of the Au tip is slightly red-shifted with the nanofilm, it is clear that the modification of the plasmon energy is small. In terms of the intensities, the relative intensity of the lower mode versus the higher modes becomes stronger with increasing the nanofilm thickness as shown in Fig. 5.8(a). Both the shift and relative intensities of the two resonances follow a similar pattern to what was observed in the earlier study of plasmon resonances of a solid Au nanosphere on Au nanofilms.[7] Furthermore, the lower plasmon resonance energy gradually approaches the higher plasmon resonance energy for thicker nanofilms. This is because the lower and higher plasmon modes are expected to finally end up to the same energy for significantly thick nanofilms, owing to the weak coupling of the surface plasmons between the two surfaces of the thick films. Indeed, Notingher et al. reported that plasmon resonance energy in a nano gap between an Au tip with the apex diameter of 20 nm and a thick Au substrate was estimated to ~ 530 nm,[11] which nearly corresponds to the plasmon resonance energy of ~ 550 nm observed in my tip-film system for the 20 nm nanofilm. These results emphasize that the lower plasmon resonance energy in the tip-film system can be precisely manipulated by selecting the nanofilm thickness.

To further expand tunable range of the plasmon resonance energy in the tip-film system, I changed size of the tip apex diameter. It has been reported that plasmon resonance energies in nanosphere-nanofilm system depend on an intrinsic plasmon energy of the nanosphere, and the plasmon resonance energy in nanosphere-nanofilm system is dramatically altered by a diameter of the nanosphere.[7,22,23] The plasmonic interaction between a metallic nanosphere and a metallic nanofilm becomes weak with decreasing a diameter of the nanosphere when the gap distance is kept constant, and therefore the plasmon resonance energy is blueshift. Hence, the plasmon resonance energy in the tip-film system is also expected to depend on the size of the tip apex diameter.

I prepared an Au-coated tip with the apex diameter of 15 nm, and measured scattering spectra in a nano gap of the tip-film system using the 15 nm Au tip under the same optical configuration as before. Figure 5.9(a) represents scattering spectra from the tip-film gap measured with the nanofilm thickness of 4, 8, 12, 16, and 20 nm, respectively. The black arrows indicate plasmon resonance peaks of the scattering spectra. These spectra were treated according to Eq. (5.4) for the normalization. Although two plasmon resonance modes are observed only for the nanofilm with the thickness of 4 nm, the plasmon mode at the virtual state clearly shows the blueshift from 700 to 520 nm with increasing the nanofilm thickness. As shown in Fig. 5.9(b), I plotted the tunable range of the plasmon resonance energy at the virtual state in the tip-film system with Au tips having the diameter of

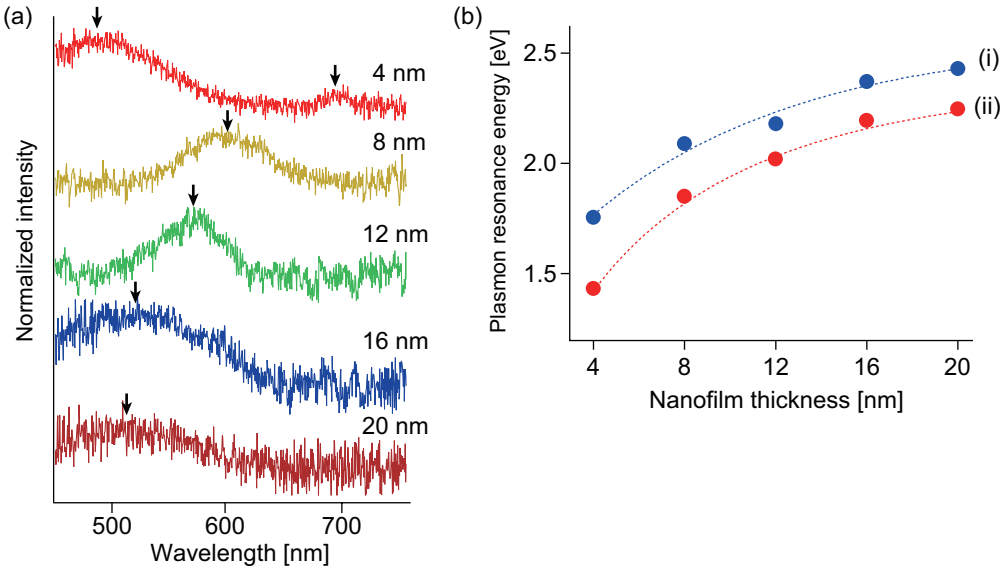


**Figure 5.9** (a) Scattering spectra of Au tip-film system measured with film thickness of 4, 8, 12, 16, and 20 nm, respectively. The diameter of the Au-coated tip was 15 nm for all spectra. The arrows indicate the plasmon resonance peaks. (b) Plasmon resonance energy of the bonding modes in the tip-film system with Au tips having the apex diameter of (i) 15 and (ii) 30 nm, as a function of the nanofilm thickness obtained from Fig. 5.8(a) and Fig. 5.9(a), respectively. The blue circles in (i) and (ii) represent the higher energy plasmon modes in the tip-film system. The dotted lines are the best fits obtained by using square exponential curves to guide the eyes.

(i) 15 nm and (ii) 30 nm. The dotted lines are the best fits obtained by using square exponential curves to guide the eyes. As one can notice from Fig. 5.9(b), the plasmon resonance energies obtained with the tip diameter of 15 nm are entirely blue-shifted with respect to those obtained with the tip of 30 nm for every value of the nanofilm thickness. The blueshift of the plasmon resonance energy is associated with the change of the localized surface plasmon energy at the tip apex for the two tips. It is well known that the plasmon resonance energy of a metallic nanoparticle is blue-shifted with the decrease of the diameter due to quantum size effect of the surface plasmons, therefore the plasmon resonance at the tip apex is expected to be blue-shifted by using the 15 nm diameter tip comparing with the 30 nm diameter tip. Since the plasmon resonance energy in the tip-film system results from the plasmon hybridization between the localized surface plasmons in the tip and the delocalized surface plasmons on the nanofilms, the hybridized plasmon mode is blue-shifted according to the blueshift of the localized surface plasmons at the tip. The quantitative understanding of the energy shift is yet to be fully examined, but it could be addressed with the FDTD calculations. This result indicates that tunable range of the plasmon resonance energy in the tip-film system can be further

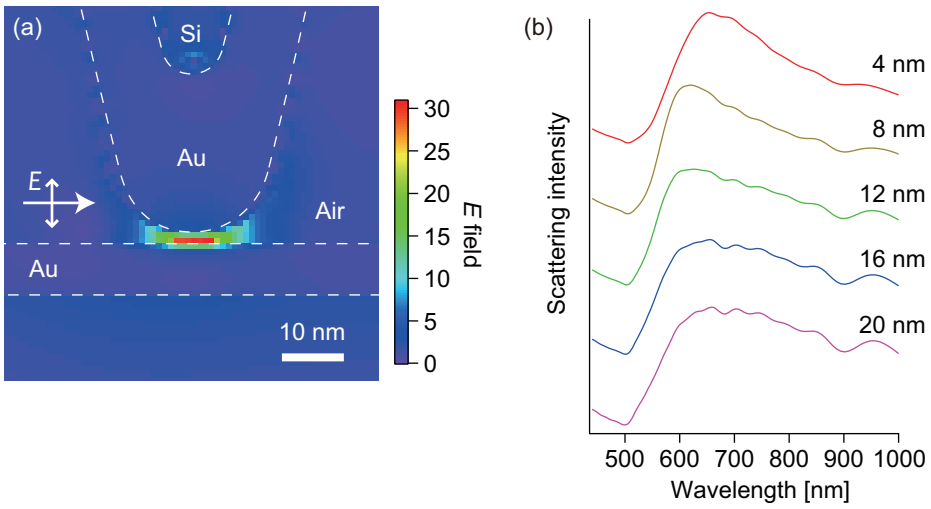


**Figure 5.10** (a) FDTD calculation of field distribution near a nano gap between an Au-coated silicon tip and an Au nanofilm. The apex diameter of the tip is 30 nm, the thickness of the nanofilm is 8 nm, and the gap distance is kept to 2 nm. Since a length of the tip should have a few hundreds of micrometer, the opposite side of the tip apex is located in a perfect matching layer. The field distribution is described at the excitation of 595 nm. (b) Calculated scattering spectra at a nano gap in Fig. 5.8(a). The spectra were calculated for the film thickness of 4, 8, 12, 16, and 20 nm.

extended by the apex size of the metallic tip. I also note that the signal to noise (S/N) ratio of the scattering spectra from the gap is decreased when the size of the tip apex is reduced from 30 to 15 nm, comparing Fig. 5.8(a) with Fig. 5.9(a). This is because scattering efficiency ($I$) from a metallic nanosphere depends on the diameter ($d$) following to $I \propto d^6$ by Rayleigh scattering theory,[30] and therefore scattering intensities from the gap between the Au tip and the Au nanofilms are also decreased using the small diameter tips. Furthermore, the S/N ratio is decreasing as the increase of the nanofilm thickness. This is because the amount of white excitation light transmitted to the tip apex through the nanofilms is decreased as the nanofilm thickness becomes thicker.

These experimental results imply an important fact that a metallic tip apex works as if it is a metallic nanosphere. I show FDTD calculation for an Au tip-film system as shown in Fig. 5.10. In the calculation, I calculated field distribution near a nano gap between an Au-coated silicon tip and an Au nanofilm. The apex diameter of the tip was 30 nm, the thickness of the nanofilm was 8 nm, and the gap distance was kept to 2 nm. Since a length of the Au-coated silicon tip should have a few hundreds of micrometer, the opposite side of the tip apex was located in a perfectly matched layer that strongly absorbed outgoing plasmon waves along the tip surfaces without reflecting them back

into the interior. The vertically polarized white light was input from the left side for the plasmon excitation. As you can see, strong field enhancement is observed at the nano gap as well as the case of nanosphere-film system in Fig. 5.4(d) and (e). However, the calculated scattering spectra from the gap in the tip-film system are quite different from the calculated spectra for nanosphere-film system, as shown in Fig. 5.10(b). The plasmon resonance energy doesn't show any particular resonance energy for the 12, 16, and 20 nm thicknesses, and the line shape is widely broadened from the visible to the near infrared region. This is due to the tip length having the micro-scale size in this calculation. The surface plasmons excited at the tip apex can propagate along surfaces of the tip and cannot be localized, so that the surface plasmons don't indicate the particular plasmon resonance energy. Thus the scattering spectra in the gap of the tip-film system represent the broad lineshape shown in Fig. 5.10(b). In my experiment obtained in Fig. 5.8 and Fig. 5.9, scattering spectra from a nano gap between an Au tip and an Au nanofilm evidently showed the plasmon resonance peaks, indicating an excitation of localized SPPs at the tip apex. Thus, it is concluded that an apex of the fabricated metallic tips works as a metallic nanoparticle. This discussion gives an important idea that geometry of a metallic tip apex for the FDTD analysis of the field enhancement has to be carefully considered, because the real geometry of the fabricated tips is usually composed of nanometric metal grains on the surfaces as shown in Fig. 2.8.

## Summary

I have explained hybridization of plasmons in gap-mode of tip-film system. I described a concept of the plasmon hybridization between localized surface plasmons at the tip apex and delocalized surface plasmons on surfaces of the nanofilm, where the two resonance modes at the virtual state and the localized state existed. In particular, the plasmon resonance energies at the virtual state were dramatically varied by a thickness of the nanofilm, due to film-thickness-dependence of a coupling of the surface plasmons on the both surfaces of the nanofilm. To prove the hybridized plasmon modes, I calculated scattering spectra from a nano gap in an Au tip-film system using FDTD method. The calculated scattering spectra represented two plasmon modes that shifted in the visible to the near-infrared region according to thickness of the nanofilm. For the experimental investigation, I fabricated Au nanofilms and Au tips by vacuum vapor deposition method, where it was confirmed that the Au nanofilms had a subnano-scale roughness and the tips were uniformly coated by Au layers. I then presented an optical setup, which was based on dark-field optical microscopy, to experi-

mentally elucidate the plasmon resonance modes in the Au tip-film system. I measured scattering spectra from the nano gap with Au nanofilms of 4, 8, 12, 16, and 20 nm thicknesses, and with an Au tip having the apex diameter of 30 nm. As a result, two plasmon resonance modes were observed in the spectra, in which the both resonance peaks appeared from 870 to 520 nm and their peak positions changed significantly with the nanofilm thickness. This behavior of the experimentally observed spectra was akin to the FDTD calculation. I also utilized an Au tip having the diameter of 15 nm, and confirmed that the plasmon resonance energies were entirely blue-shifted with respect to those obtained using the Au tip having the diameter of 30 nm for every value of the nanofilm thickness. The blueshift of the plasmon resonance energy was associated with the energy shift of the localized surface plasmons at the tip apex for the two tips. Finally, I discussed geometry of an Au tip apex and gave an important idea that the Au tip apex could work as if it was an Au nanosphere in the tip-film system.

## References


1. M. Micic, N. Klymyshyn, Y. D. Suh, and H. P. Lu, *J. Phys. Chem. B*, **107**, 1574-1584 (2003).
2. W. Zhang, X. Cui, B. Yeo, T. Schmid, C. Hafner, R. Zenobi, *Nano Lett.*, **7**, 1401-1405 (2007).
3. B. Pettinger, K. F. Domke, D. Zhang, G. Picardi, and R. Schuster, *Surf. Sci.*, **603**, 1335-1341 (2009).
4. N. Behr and M. B. Raschke, *J. Phys. Chem. C*, **112**, 3766-3773 (2008).
5. I. Notingher and A. Elfick, *J. Phys. Chem. B*, **109**, 15699-15706 (2005).
6. E. N. Economou, *Phys. Rev*., **182**, 539-554 (1969).
7. F. Le, N. Z. Lwin, J. M. Steele, M. Käll, N. J. Halas, and P. Nordlander, *Nano Lett*., **5**, 2009-2013 (2005).
8. K. H. Su, Q. H. Wei, X. Zhang, J. J. Mock, D. R. Smith, and S. Schultz, *Nano Lett*., **3**, 1087-1090 (2003).
9. P. Nordlander, C. Oubre, E. Prodan, K. Li, and M. I. Stockman, *Nano Lett.*, **4**, 899-903 (2004).
10. E. Prodan, C. Radloff, N. J. Halas, and P. Nordlander, *Science*, **302**, 419-422 (2003).
11. H. Wang, Y. Wu, B. Lassiter, C. L. Nehl, J. H. Hafner, P. Nordlander, and N. J. Halas, *Proc. Natl. Acad. Sci. USA*, **103**, 10856-10860 (2006).

12. G. Leveque and O. J. F. Martin, *Opt. Express*, **14**, 9971-9981 (2006).
13. J. J. Mock, R. T. Hill, A. Degiron, S. Zauscher, A. Chilkoti, and D. R. Smith, *Nano Lett*., **8**, 2245-2252 (2008).
14. 岡本隆之, 梶川浩太朗, プラズモニクス, 講談社 (2010).
15. F. Hao and P. Nordlander, *Appl. Phys. Lett*., **89**, 103101 (2006).
16. E. Prodan and P. Nordlander, *J. Chem. Phys.*, **120**, 5444-5454 (2004).
17. Y. Fang, N. Seong, and D. D. Dlott, *Science*, **321**, 388 (2008).
18. S. J. Oldenburg, R. D. Averitt, S. L. Westcott, and N. J. Halas, *Chem. Phys. Lett*., **288**, 243-247 (1998).
19. Y. G. Sun and Y. N. Xia, *Science*, **298**, 2176-2179 (2002).
20. S. Link and M. A. El-Sayed, *J. Phys. Chem. B*, **103**, 8410-8426 (1999).
21. C. J. Murphy, T. K. Sau, A. Gole, and C. J. Orendorff, *MRS Bull*., **30**, 349-355 (2005).
22. T. Okamoto and I. Yamaguchi, *J. Phys. Chem. B*, **107**, 10321 (2003).
23. K. Tsuboi, S. Abe, S. Fukuba, M. Shimojo, M. Tanaka, K. Furuya, K. Fujita, and K. Kajikawa, *J. Chem. Phys.*, **125**, 174703 (2006).
24. Y. Uchiho and K. Kajikawa, *Chem. Phys. Lett*., **478**, 211 (2009).
25. A. Cvitkovic, N. Ocelic, J. Aizpurua, R. Guckenberger, and R. Hillenbrand, *Phys. Rev. Lett*., **97**, 060801 (2006).
26. P. B. Johnson and R. W. Christy, *Phys. Rev. B*, **6**, 4370-4379 (1972).
27. L. J. Sherry, S. H. Chang, G. C. Schatz, R. P. Van Duyne, B. J. Wiley, and Y. N. Xia, *Nano Lett*., **5**, 2034-2038 (2005).
28. R. H. Ritchie, *Surf. Sci*., **34**, 1-19 (1973).
29. S. Hayashi, T. Yamada, and H. Kanamori, *Opt. Commun*., **36**, 195-199 (1981).
30. C. F. Bohren and D. R. Huffman, *Absorption and Scattering of Light by Small Particles*, WILEY-VCH, p.132 (2004).

# Chapter 6.
# TERS measurement of gap-mode of tip-film system

I have presented plasmon hybridization in gap-mode of a metallic tip-film system, in which the resonance plasmon energy was varied by the thickness of the nanofilm. The tunable plasmon resonance in the tip-film system can be expedient for obtaining the highest value of field enhancement in TERS when it is required to use a particular excitation wavelength suitable for a given sample. In this last chapter, I intend to evaluate the enhancement in Raman signals at a nano gap in the metallic tip-film system. To elucidate the enhancement, I measure TERS of a sample at the nano gap by varying the thickness of the nanofilms. Then, I estimate enhancement factor of the Raman signals in the tip-film system, and discuss superiority of the gap-mode TERS using a metallic nanofilm.

## 6.1
## TERS spectra in gap-mode of tip-film system

For Raman measurements in gap-mode TERS spectroscopy, I utilized a self-assembled monolayer of 4-ATP molecules adsorbed on Au nanofilms. This is because the molecular height of 4-ATP is ~ 0.7 nm and the geometry of the SAM is uniform over surface of the Au nanofilms. I prepared a SAM of 4-ATP molecules on Au nanofilms of different thicknesses ranging from 4 to 16 nm by following to the preparation method introduced in Section 2.3.2. For the Raman measurements, I used an optical system of TERS microscopy introduced in Section 2.2. For the excitation, single-mode diode laser ($\lambda$ = 642 nm) was used, where resonance Raman effect can be negligible due to weak absorption of 642 nm light by 4-ATP molecules. An Au-coated tip with an apex diameter of 30 nm was utilized, and the tip was brought in contact with the sample. In this configuration, the tip and the nanofilm were kept with a nano gap corresponding to length of the 4-ATP molecules.

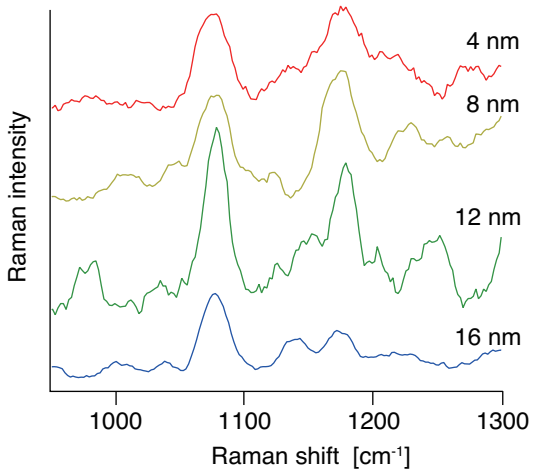


**Figure 6.1** TERS spectra from a monolayer of 4-ATP molecules sandwiched between an Au-coated tip with the apex diameter of 30 nm and Au nanofilms with the individual thicknesses.

Figure 6.1 shows examples of TERS spectra taken from the monolayer of 4-ATP molecules sandwiched between the tip and the nanofilms with the thickness of 4, 8, 12, and 16 nm, respectively. These spectra represent the normalized pure near-field Raman signals (that is, the far-field Raman signals are subtracted). The intensities of the TERS spectra slightly depended on the position of the sample surface because the Au nanofilms didn't have the atomic-scale flatness. Therefore, I measured the TERS spectra from different 25 points, and calculated the average intensities. TERS spectra shown in Fig. 6.1 were chosen from a spectrum nearest to the average. In addition, since TERS from the samples was detected by transmitting through Au nanofilms, I considered absorption of the TERS by the Au nanofilms in order to normalize intensities of the TERS spectra. As shown in Fig. 6.1, several Raman modes were observed at 1078, 1141, and 1179 $cm^{-1}$, which could be assigned to various vibrational modes of 4-ATP molecules. Since these spectra are purely enhanced spectra, all these modes represents enhancement in the Raman signals at the gap between the tip and the nanofilm. Interestingly, the each Raman spectrum shows slightly different shapes. For example, the Raman spectrum for the 12 nm nanofilm shows the maximum intensity at 1078 $cm^{-1}$, while the Raman spectrum for the 8 nm nanofilm indicates the maximum intensity at 1179 $cm^{-1}$. This phenomenon is due to the chemically enhanced modes of 4-ATP molecules at a nano gap in tip-film system. As I explained in Section 2.3.5, chemically enhanced modes of 4-ATP molecules can be dramatically excited in such metallic junctions, and the vibrational energy can be perturbed depending on the adsorption angle or adsorption site. Judging from assignment of the 4-ATP vibrational modes in Table

2.1, the both modes at 1078 and 1179 $cm^{-1}$ are based on the $a_1$ modes (due to electromagnetic effect). It appears not to be related to the chemical effect in SERS, however the Raman mode at 1179 $cm^{-1}$ can be disturbed by the Raman mode at 1141 $cm^{-1}$ that is associated with the $b_2$ modes (due to the chemical effect). Indeed, the Raman peak at 1179 $cm^{-1}$ for the 8 nm nanofilm in Fig. 6.1 is overlapped with a peak at the left shoulder. Therefore, the Raman intensities at 1179 $cm^{-1}$ may undergo some changes. For this reason, I adopted the Raman mode at 1078 $cm^{-1}$ to evaluate the field enhancement in gap-mode of this tip-film system.

## 6.2
## Film-thickness-dependence of Raman enhancement

As shown in Fig. 6.1, the Raman spectrum measured for the 12 nm nanofilm showed distinctly larger enhancement at the 1078 $cm^{-1}$ in comparison with the spectra measured with both thinner and thicker nanofilms. Thus I can conclude that the Raman enhancement indicates a clear dependence on the nanofilm thickness, and that the enhancement selectively increases for a particular value of the nanofilm thickness. In order to quantitatively evaluate the enhancement, I calculate enhancement factors at the gap as a function of the nanofilm thickness.

The enhancement factor for Raman scattering is defined as an intensity ratio of the enhanced Raman spectra to the spontaneous Raman spectra from molecules in a unit volume under same experimental condition.[1,2] The enhancement factor (EF) can be described by

$$EF = \frac{I_{gap}/N_{gap}}{I_{bulk}/N_{bulk}} \tag{6.1}$$

where $I_{gap}$ represents an enhanced intensity of a Raman mode in the TERS spectrum observed in the nano gap, and $I_{bulk}$ is an intensity of the same Raman mode in the spontaneous Raman spectrum. $N_{gap}$ expresses the number of 4-ATP molecules within a volume of the enhanced field at the nano gap, and $N_{bulk}$ is the number of 4-ATP molecules in a solid sample within the focal volume. For the estimation of the enhancement factor, I utilized Raman intensity at 1078 $cm^{-1}$, which is mainly attributed to electromagnetically enhancement in the TERS as discussed in previous section. $N_{gap}$ is estimated by an area of the enhanced field at the nano gap and a packing density of the 4-ATP molecules on Au nanofilms. The lateral size of the enhanced field can be roughly estimated by the FDTD results in Fig. 6.2(a), and it is estimated to 17 nm from a line profile of the field

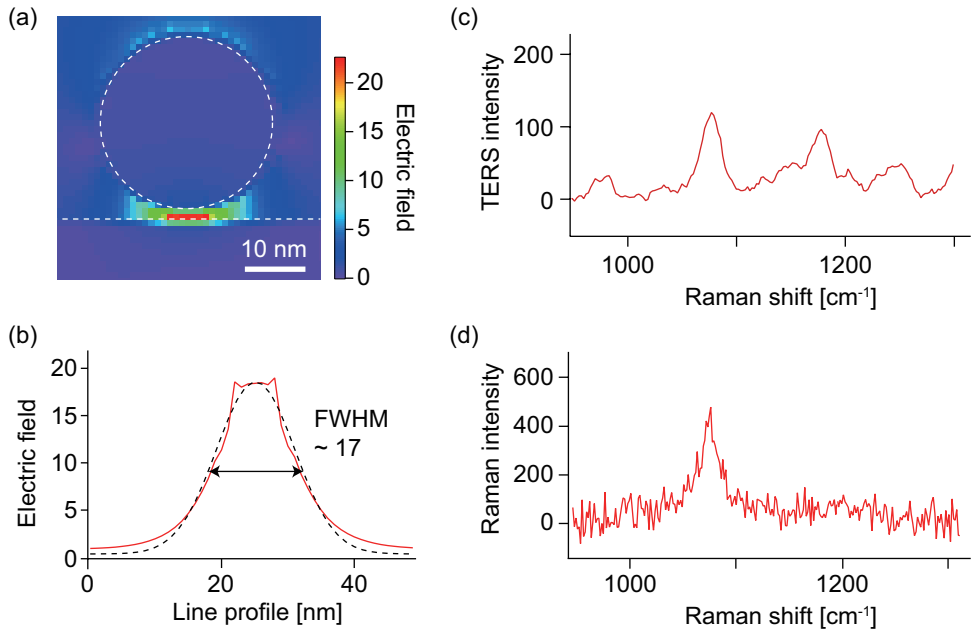


**Figure 6.2** (a) Calculated field distribution around the tip-film gap for 12 nm nanofilm, excited at 624 nm wavelength (the lower resonance mode). The tip diameter was set to 30 nm. (b) Line profile of field distribution along the horizontal axis including the highest value in Fig. 6.2(a). (c,d) TERS and spontaneous Raman spectra of 4-ATP molecules excited at 642 nm wavelength, respectively.

distribution along the horizontal axis including the gap as shown in Fig. 6.2(b). The each 4-ATP molecule occupies ~ 0.20 nm$^2$ on full coverage of an Au nanofilm.[2] As a result, $N_{gap}$ is eventually estimated to 1.1 × 10$^3$. $N_{bulk}$ can be estimated by a volume of the laser focus in the far-field Raman measurement and the density of solid 4-ATP (1.18 g/cm$^3$). The volume of the laser focus is considered as an ellipsoidal body with the long axis of the focal depth and the short axis of lateral size of the focus. Following the consideration of the density, the focal volume, and Avogadro constant, $N_{bulk}$ is estimated to 5.5 × 10$^{10}$. For obtaining Raman intensities of $I_{gap}$ and $I_{bulk}$, I measured the TERS and spontaneous spectra of 4-ATP molecules as shown in Fig. 6.2(c) and (d), respectively. The both spectra were taken under the same exposure time and same laser intensity. Finally, I assigned these estimated values to Eq. (6.1), I calculated the Raman enhancement factor in this Au tip-film system.

Figure 6.3(a) shows the calculated enhancement factor as a function of the nanofilm thickness, which is varied from 4 to 16 nm. In order to obtain high reliability in the results, the enhancement factor was averaged from 25 measurements. The maximum extents of their experimental errors are represented by the error bars, which probably come from a possible variation in the sample packing

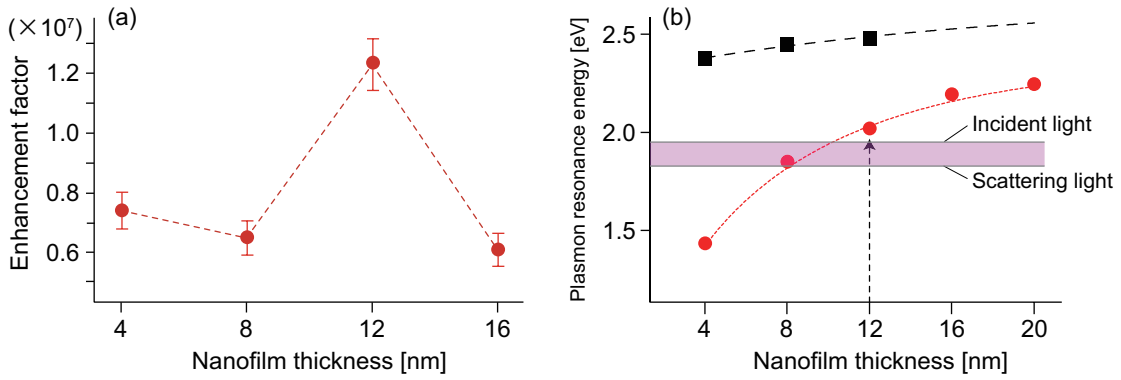


**Figure 6.3** (a) Enhancement factor in TERS measurement as a function of the nanofilm thickness. The error bars represent the maximum extent of the experimental error in 25 identical measurements. (b) Plasmon resonance energy in this tip-film system from Fig. 5.6(b) to compare the resonance condition in this tip-film system with the energies of the incident light at λ = 642 nm and the scattering light at λ = 689 nm that corresponds to Raman scattering from 4-ATP molecules at 1078 $cm^{-1}$.

density on the nanofilm and from temporal fluctuation of apparatus in the optical system. As shown in Fig. 6.3(a), the enhancement factor indicates a clear increase only for the nanofilm thickness of 12 nm, which was also seen from the spectra shown in Fig. 6.1. This result can be explained by the fact that the hybridized plasmon resonance is tuned well for the excitation wavelength. I referred the plasmon resonance energy in a gap of this tip-film system, which was discussed earlier for the Au tip with the apex of 30 nm in Fig. 5.6(b), and also described the energies of the incident light at λ = 642 nm and the scattering light at λ = 689 nm that corresponds to Raman scattering from 4-ATP molecules at 1078 $cm^{-1}$ as shown in Fig. 6.3(b). As you can see, the incident and scattering light should be strongly resonant with the hybridized plasmons at the nanofilm thickness of 8 nm, rather than 12 nm. This confliction is understood by the effect of the 4-ATP molecules adsorbed on Au nanofilms. The refraction index of 4-ATP molecules is ~ 1.5,[8] so that the plasmon resonance energies in the tip-film system can be modified by the presence of the 4-ATP molecules. Since the scattering measurement for investigating the plasmon resonance energies was performed in air without 4-ATP molecules, its energies can be slightly red-shifted. Namely, the resonance curves in Fig. 6.3(b) can be entirely down-shifted by the existence of the 4-ATP molecules. Thus, the thickness of 12 nm could give the maximum Raman enhancement in the TERS measurement. To confirm the energy shift of the plasmon resonance by the adsorption of 4-ATP molecules on a nanofilm, I measured extinction spectra of 4-nm Au nanofilms with and without 4-ATP molecules as shown in Fig. 6.4. As you can see,

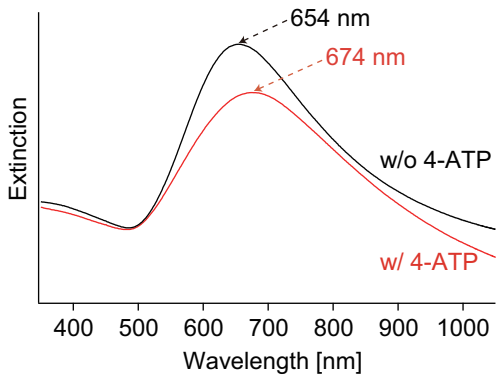


**Figure 6.4** Extinction spectra of 4-nm Au nanofilms (red) with and (black) without 4-ATP molecules. The peak position of the resonances is red-shifted from 654 to 674 nm with 4-ATP molecules.

the peak position of the resonances is red-shifted from 654 to 674 nm with 4-ATP molecules. If a comparable energy shift of the resonance is adopted to the Au tip-film system, the resonance condition of the Au tip-film system at the 12-nm nanofilm goes into resonance window between the incident and excitation energies, while that at the 8-nm nanofilm deviates from the resonance window. The precise amount of the energy shift can be estimated by the FDTD calculation. One also notices that the field enhancement for the 4 nm nanofilm is not the minimum among the four different nanofilm thicknesses examined here, though the plasmon resonance is expected to be the farthest from energy of the excitation laser for this nanofilm thickness. I believe that this is due to the general observation that thin films provide larger electric field enhancements than thick films due to the symmetrically aligned surface charges, as illustrated in Fig. 5.1(a).[3] For a nanofilm, the surface charges on the bottom surface of the nanofilm contributes significantly to the field enhancement in the junction because of their proximity. These results indicate that nanofilm thickness has a crucial role for the field enhancement at a nano gap between a metallic tip and a metallic nanofilm, and a proper selection of the nanofilm thickness can result in huge enhancement through plasmon hybridization between the tip and the nanofilm.

I also discuss the enhancement factor in gap-mode of this tip-film system. The enhancement factor was estimated to $0.5 - 1.2 \times 10^7$ order with the any nanofilms as shown in Fig. 6.3. Given that Raman enhancement factor at a metallic tip apex without metallic nanofilms was estimated to be ~ 313 as discussed in Section 3.3, the enhancement factor was greatly improved with the use of the nanofilms. Comparing with other researcher's results, the enhancement factor in my gap-mode TERS was comparable with that reported by Raschke (Au tip and Au substrate, $\sim 5 \times 10^9$),[4] Zenobi

(Ag tip and Au substrate, ~ $9 \times 10^6$),[5] and Pettinger groups (Au tip and Au substrate, $1.6 \times 10^6$).[6] The optical configuration and samples used in these articles are different each other including my experimental condition, therefore the enhancement factor indicates a certain level of dispersion.

The enhancement factor of my gap-mode system could be further improved with the usage of an atomically flat Au surface. Au nanofilms that I used have subnano-scale roughness on the surface as shown in Fig. 5.3, which gives background SERS of sample molecules at junctions of the asperities on the nanofilms. As a result, Raman signals from a gap between a metallic tip and a nanofilm are buried in the background noise. Hence the enhancement factor is estimated to as a small value as it should be. The roughness on Au nanofilms can be reduced using an adhesion layer such as chromium, but vacuum vapor deposition method is not essentially suitable for the fabrication of the atomically flat surface due to the surface tension of Au atoms. Although citrate reduction of $HAuCl_4$ was suggested for the synthesis of ultraflat Au nanoplates, subnano-scale roughness (~ 0.2 nm) was formed on the nanoplates.[7] The decrease of roughness on metallic nanofilms remains to be solved.

## Summary

I have studied field enhancement at a nano gap between an Au tip and an Au nanofilm by measuring TERS spectra of 4-ATP molecules at the gap. It was found that the TERS intensity at the gap depended on the nanofilm thickness. I calculated Raman enhancement factor at the gap by intensities of an electromagnetically enhanced Raman mode of the 4-ATP molecule, and confirmed that the Au tip-film system gave the largest enhancement factor of ~ $1.2 \times 10^7$ under the plasmon resonance condition with the excitation laser, where the effect of 4-ATP samples was considered. This approach of tuning the plasmon resonance energy by changing the nanofilm thickness could provide significant improvement of the filed enhancement. The enhancement factor could be further improved with the usage of atomically flat nanofilms, because junctions of asperities on the nanofilms would give background SERS of the sample molecules. The decrease of roughness on metallic nanofilms remains to be solved for further improvement of the sensitivity of gap-mode TERS using metallic nanofilms.

## References


1. Y. Wang, H. Chen, S. Dong, and E. Wang, *J. Chem. Phys*., **124**, 074709 (2006).
2. X. Hu, T. Wang, L. Wang, and S. Dong, *J. Phys. Chem. C*, **111**, 6962-6969 (2007).
3. F. Le, N. Z. Lwin, N. J. Halas, and P. Nordlander, *Phys. Rev. B*, **76**, 165410 (2007).
4. C. C. Neacsu, J. Dreyer, N. Behr, and M. B. Raschke, *Phys. Rev. B*, **73**, 193406 (2006).
5. W. Zhang, B. S. Yeo, T. Schmid, and R. Zenobi, *J. Phys. Chem. C,* **111**, 1733-1738 (2007).
6. K. F. Domke, D. Zhang, and B. Pettinger, *J. Am. Chem. Soc*., **128**, 14721-14727 (2006).
7. T. Deckert-Gaudig and V. Deckert, *Small*, **5**, 432-436 (2009).
8. E. Valério, L. M. Abrantes, and A. S. Viana, *Electroanalysis*, **20**, 2467-2474 (2008).

# Conclusion

In this dissertation, I have addressed plasmon hybridization in the gap between a metallic tip and a metallic nanofilm for tip-enhanced Raman analysis of nanomaterials. I pointed out the necessity of improving sensitivity of TERS microscopy through the demonstration of TERS imaging of carbon-based nanomaterials. I then suggested a tunable plasmon hybridization system in which the plasmon resonance energies at the tip-film gap could be adjusted for the resonant excitation of plasmons by a thickness of the nanofilm, and I confirmed that the tunable plasmon resonance was useful to enhance the sensitivity in tip-enhanced Raman analysis.

The substance of this dissertation is to improve the sensitivity of TERS microscopy, and the metallic nanofilm is certainly the key geometry for it. On the other hand, such a metallic nanofilm has a subnano-scale roughness on the surface, which dramatically increases the background noise in the gap-mode TERS system as discussed in Chapter 5 and 6. Therefore, fabrication of atomically flat nanofilms is one of the most important issues. Single-crystalline Au nanoplates with a uniform face orientation or a template-stripping Au substrate [1,2] might be a good candidate as the nanofilms.

The required measurement time for taking one TERS image is directly dependent on the sensitivity of TERS microscopy, and that is, on the enhancement in Raman signals at a metallic tip apex. The enhancement factor at a metallic tip apex is extremely improved with the usage of a metallic nanofilm. In fact, a metallic tip approached on a metallic nanofilm gave more than $3.8 \times 10^4$ times higher enhancement in the TERS than the metallic tip without the metallic nanofilm, as discussed in Chapter 6. Therefore, the measurement time for TERS imaging in the gap-mode system should be reduced down to less than one second ideally, although the measurement time is limited by tracking speed of a metallic tip apex on a sample surface. If the gap-mode TERS system can be operated with high-speed AFM system[3], video-rate TERS imaging of molecular dynamics might be realized. The investigation of the measurement time in gap-mode TERS is the important issue remaining in this research.

Evaluation of spatial resolution of the gap-mode TERS microscopy using metallic nanofilms is

also a challenging topic in the future. As I introduced in Section 2.4, the spatial resolution in gap-mode TERS microscopy is generally much better than that in TERS microscopy without metallic nanofilms. In addition, the hybridized plasmons in the gap invoke two resonance modes, and the two resonance modes have a different field distribution around the gap. Therefore, the spatial resolution in the gap-mode TERS microscopy would depend on the plasmon modes. It is also possible that the spatial resolution depends on a thickness of the nanofilm.

New physics would be identified when we could observe the nano-scale world with light. The importance of tip-enhanced Raman microscopy would be rising along with the development of nano science in the future. I hope this dissertation will be conducive to such the nano-scale investigation.

## References

1. M. Hegner, P. Wagner, and G. Semenza, *Surf. Sci.*, **291**, 39-46 (1993).
2. P. Nagpal, N. C. Lindquist, S. Oh, and D. J. Norris, *Science*, **325**, 594-597 (2009).
3. N. Kodera, D. Yamamoto, R. Ishikawa, and T. Ando, *Nature*, **468**, 72-77 (2010).

# List of publications

**Original papers**

1. **Kazumasa Uetsuki**, Prabhat Verma, Taka-aki Yano, Yuika Saito, Taro Ichimura, and Satoshi Kawata, "Experimental identification of chemical effects in surface enhanced Raman scattering of 4-aminothiophenol," The journal of physical chemistry C, vol. 114, pp. 7515-7520 (2010)
2. **Kazumasa Uetsuki**, Prabhat Verma, Peter J. Nordlander, and Satoshi Kawata, "Tunable plasmon resonances in a metallic nanotip-film system" (Nanoscale, in press)
3. **Kazumasa Uetsuki,** Prabhat Verma, Taka-aki Yano, and Satoshi Kawata, "Imaging of isolated single-walled carbon nanotubes through resonant Raman scattering" (Applied Physics Letters, to be submitted)
4. **Kazumasa Uetsuki**, Prabhat Verma, and Satoshi Kawata, "Nanoscale Raman imaging of graphene layers" (in preparation)
5. Taka-aki Yano, Taro Ichimura, Shota Kuwahara, Fekhra H'Dhili, **Kazumasa Uetsuki**, Yoshito Okuno, Prabhat Verma, and Satoshi Kawata, "Nanoscale visualization of strain distribution in carbon nanotubes" (Science, submitted)

**International conferences**

1. Yoshito Okuno, Shota Kuwahara, **Kazumasa Uetsuki**, Taka-aki Yano, Prabhat Verma, and Satoshi Kawata, "Tip-enhanced Raman imaging and analysis of crossed nanotube junctions," The 8$^{th}$ Asia-Pacific Conference on Near-Field Optics, Paper-Number: 23 (Adelaide, Australia, 2011)
2. **Kazumasa Uetsuki** and Peter Nordlander, "Plasmonic Interaction at the Gap in a Metallic Nano Tip and a Thin Film System," The 25$^{th}$ Rice Quantum Institute Summer Research Colloquim 2011, Paper Number: EP-41 (Rice University, Houston, 2011)

3. **Kazumasa Uetsuki**, Prabhat Verma, Taka-aki Yano, Yuika Saito, Taro Ichimura, and Satoshi Kawata, "Experimental identification of chemical effects in surface enhanced Raman scattering of 4-aminothiophenol," XXII International conference on Raman spectroscopy, Paper Number: 095 (Boston Park Plaza Hotel, Boston Massachusetts, 2010)
4. **Kazumasa Uetsuki**, Prabhat Verma, Taro Ichimura, and Satoshi Kawata, "Plasmonic hybridization at the gap between a metallic nano-tip and a nano-film system," The 7th Asia-Pacific Conference on Near-Field Optics, Paper Number: II(1)-AW3, (International convention center, Jeju Island, Korea, 2009)
5. **Kazumasa Uetsuki**, Prabhat Verma, Taro Ichimura, Yasushi Inouye, and Satoshi Kawata, "Near-field Raman scattering at the gap between a metallic nano-tip and a nano-film system," SPIE Optics + Photonics 2009, Paper Number: 7395-8 (San Diego convention center, San Diego, 2009)

**Domestic conferences**

1. **植月一雅**、バルマプラブハット、矢野隆章、市村垂生、齋藤結花、河田聡、「表面増強ラマン散乱におけるモード選択的な化学増強効果の検証」、2010 年春季第 57 回応用物理学関連連合講演会、（東海大学、神奈川、2010）
2. **植月一雅**、バルマプラブバット、市村垂生、井上康志、河田聡、「金属チップ-金属薄膜システムを用いたギャップモード TERS 顕微鏡;膜厚による電場強度の制御」、 2009 年春季第 56 回応用物理学関連連合講演会、1a-H-9（筑波大学、茨木、2009）
3. **植月一雅**、森田寛之、矢野隆章、市村垂生、齋藤結花、バルマプラブバット、井上康志、河田 聡、「共鳴ラマン効果を用いたカーボンナノチューブの多波長ラマン分光計測とイメージング」、2007 年秋季第 68 回応用物理学会学術講演会、8a-T-10（北海道工業大学、北海道、2007）

# Acknowledgements

This dissertation is the result of the valuable support and input of teachers, collaborators, and friends.

**Professor Satoshi Kawata** (Department of Applied Physics, Osaka University) for his comments and incredible ideas. My view was always stimulated by his point of view and the way of thinking, which made me go on to doctoral course. I could learn the essential things, for instance presentation skills and the way to consider research themes, for surviving research life as a doctor. I could also have an opportunity to study abroad in my doctoral course for about seven months by his effort, which was extremely treasured experience to me for cultivating my international sense. I would like to again express my gratitude to him.

**Professor Prabhat Verma** (Department of Applied Physics, Osaka University) for his discerning advises on this dissertation. During science discussion with him, I could develop my expertise in nanophotonics and also maybe my English skills. He really supported to me for developing a theory, writing papers and making presentations even on holidays. I was also helped by his encouragement during this dissertation many times.

**Professor Shinji Hayashi** (Department of Electrical and Electronic Engineering, Kobe University), **Professor Yasuhiro Sugawara** (Department of Applied Physics, Osaka University), and **Professor Junichi Takahara** (Department of Applied Physics, Osaka University) for giving comments and suggestions on this dissertation for the improvement. They were really important for giving another thought to this dissertation.

**Professor Peter Nordlander** (Department of Physics and Astronomy, Department of Electrical and Computer Engineering, Rice University) for giving a chance to study in his laboratory for about three months. The experience was really valuable for reconsidering fundamental ideas in this dissertation and directly feeling the American's research life.

**Associated Professor Yuika Saito** (Department of Applied Physics, Osaka University), **Dr. Taro Ichimura** (Laboratory for Comprehensive Bioimaging, Riken Qbic), **Assistant Professor Taka-aki Yano** (Department of Electronic Chemistry, Tokyo Institute of Technology), **Assistant Professor Shota Kuwahara** (Department of Applied Chemistry, Chuo University), **Dr. Fekhra H'dhili**, and **Yoshito Okuno** (Department of Applied Physics, Osaka University) for deeply discussing together about TERS measurement of single-walled carbon nanotubes. I never forget running full out to accomplish the researches together in those days.

**Professor Zouheir Sekkat** (Nanophotonics Laboratory, The Institute of Nanomaterials and Nanotechnology) for accepting me to research in his nanophotonics laboratory for about five months. It was the first time for me to live (and survive) abroad and experience Ramadan, and I could gain international points of view to researches by the discussion with him and his laboratory's researchers.

**Dr. Yasuaki Kumamoto** (RIKEN)**, Dr. Kyoko Masui** (Photonics Center, Osaka University), **and Dr. Masahito Yamanaka** (Department of Applied Physics, Osaka University) for giving advice with respect to experiments and researches since I joined Kawata Laboratory.

**Mitsuhiro Honda**, **Masaya Okada**, and **Hiroyuki Morimura** (Department of Applied Physics, Osaka University) for often discussing with me about fundamental physics of photonics, material science, and bioscience.

**Toshihiro Mino**, **Yu Jun**, **Maouli Imad**, **Yoshiro Ohashi**, and **Takayuki Umakoshi** (Department of Applied Physics, Osaka University), and other NSOM group members for exchanging knowledge and experiences in all aspects of optics.

I appreciate other members in LaSIE and my friends all over the world. Thanks to them, I could enjoy my research life in my doctoral course.

I finally show my deep gratitude to my family and girlfriend for their understanding, encouragement, and love throughout my life even during hard time of this dissertation.